DRIVING INNOVATION IN FRACTURE CONDUCTIVITY AND PROPPANT TRANSPORT STIMULATION WORKFLOWS WITH 3D PRINTING TECHNOLOGY

A Thesis

by

CARRIE LYNN SISTRUNK

Submitted to the Graduate and Professional School of
Texas A&M University
In partial fulfillment of the requirements for the degree of

MASTER OF SCIENCE

Chair of Committee	Ding Zhu
Co-Chair of Committee	Dan Hill
Committee Member	Victor Ugaz
Head of Department	Akhil Datta-Gupta

August 2023

Major Subject: Petroleum Engineering

Copyright 2023 Carrie Sistrunk

ABSTRACT

The primary focus of this thesis is to summarize a workflow that leverages 3D printing to generate repeatable rock conductivity samples, reducing uncertainty associated with experimental results. Study results illustrate how proppant concentration impacts fracture conductivity while also demonstrating that conductivity results obtained from these 3D-printed samples are repeatable and reasonable relative to previous experimental studies.

Many previous studies have illustrated that rock surface topography and proppant characteristics are the primary informants of fracture conductivity. Given that conductivity is instrumental in determining how prolific a fractured well in a given resource is, great effort has been made to employ conductivity experiments to better understand how completion design and subsurface characteristics interact to inform conductivity. Still, isolating and evaluating rock sample characteristics systematically to form consistent conclusions given the intrinsically heterogeneous nature of subsurface rocks remains challenging.

Historically, samples for conductivity experiments are generated by fracturing downhole or outcrop rocks with tension to create realistic fracture surfaces that capture a wide range of possible surface morphologies. The surfaces created are inherently distinctive, even when using samples taken from the same block. This lack of sample repeatability complicates identification of the impact of rock characteristics on conductivity.

To overcome this challenge, 3D printing was employed as a means to produce consistent samples with well-defined surfaces to be used in conductivity experimental programs. In doing so, a set of geostatistically informed coordinates was first generated to numerically depict a rough fracture surface. The coordinates in this system were then connected to form one continuous

surface before sizing and scaling the resulting model to appropriately resemble the 7-inch long, 2-inch wide conductivity sample required for experimentation. The resulting 3D model was then printed with a Digital Light Processing (DLP) 3D printer. The 3D-printed output served as a prototype to create a mold of the conductivity sample, which was, in turn, used to produce "rock" samples made of high-strength cement.

With this methodology, conductivity samples with identical surface roughness and features were created and replicated. Reproducing identical samples allows for isolation and testing of parameters such as proppant size and concentration, in addition to reducing uncertainty associated with experimental results by conducting the same experiment more than once. Fracture conductivity tests were conducted using a modified-API conductivity cell and artificial "rock" samples with varied surface topography.

This thesis aims, secondarily, to summarize progress made in making proppant transport experimental workflows more comprehensive with the help of 3D printing. Like fracture conductivity, how effectively proppant is transported through a fracture network and subsequently distributed throughout that network is a key determining factor in how prolific a fractured well in a given resource turns out to be.

The foundation of these proppant transport and distribution experiments remains largely unchanged to date. That being said, this study aims to incorporate another layer of subsurface complexity by creating a fracture network for proppant transport experimentation characterized by 3D-printed, rough-walled fracture surfaces.

The rough-wall fracture network that was printed for this study is characterized with greater correlation of features in the direction of flow. Results associated with this updated fracture network were compared to the previous surface characterization generated, printed, and analyzed

by Tatman et al. (2022). Although the results garnered from the most recent fracture system are preliminary, they do offer insights into the impact that surface topography has on proppant transportation and distribution.

When employed appropriately, 3D printing can be leveraged to make a variety of stimulation experimental workflows more robust in nature.

DEDICATION

This work is dedicated to my grandfathers, Donald L. Whitley '48 and William T. Sistrunk '52; to my parents, Thomas W. Sistrunk '87 and Melissa L. Sistrunk '90; and to my brother, Connor W. Sistrunk '21—all of whom have always offered me their unwavering support and all of whom have played a role in making me the person I am today.

ACKNOWLEDGEMENTS

I would like to thank Dr. Ding Zhu and Dr. Daniel Hill for their continued support of my academic pursuits. Without their technical insights, extensive experience, and robust knowledge base, this project would not have been possible.

I would also like to thank Dr. Jennifer Miskimins and Dr. Ashtiwi Bahri from the Colorado School of Mines for their contributions to this research program.

Additionally, I would like to thank Dr. Valerie Jochen, Dr. John Lee, and Professor Cathy Sliva for their mentorship throughout my pursuit of both my Bachelor of Science and Master of Science degrees.

Lastly, I would like to acknowledge John Maldonado and all of the peers in my research group who have always been willing to lend a helping hand in the lab. They have supported me throughout my time in the department and made my time at Texas A&M something I will look back on fondly.

CONTRIBUTORS AND FUNDING SOURCES

Contributors

This work was part of a joint research project between Texas A&M University, the Colorado School of Mines, and sponsors of the 3D Printing Research for Well Stimulation Program. The thesis committee consists of Dr. Ding Zhu and Dr. Daniel Hill of the Harold Vance Department of Petroleum Engineering and Dr. Victor Ugaz of the Artie McFerrin Department of Chemical Engineering at Texas A&M University.

The code utilized for this research from Stanford University's Geostatistical Software Library (GSLIB) and from Dr. Michael Pyrcz's (University of Texas at Austin) Geostats Py Python Library was modified with help from Tohoko Tajima and Gabriel Tatman.

The conductivity experimental apparatus was assembled by Travis Brashear from Texas A&M University. The proppant transport experimental apparatus was assembled by Dr. Ashtiwi Bahri at the Colorado School of Mines.

Funding Sources

This graduate study was supported by the College of Engineering Merit Fellowship supplied by both the Texas A&M University College of Engineering and the Harold Vance Department of Petroleum Engineering. This work was also made possible through funding provided by companies sponsoring the Joint Investigative Project for 3D Printing Well Stimulation Research: ExxonMobil, ConocoPhillips, Schlumberger, and Mitsubishi Chemical.

TABLE OF CONTENTS

Page

LIST OF FIGURES

Page

1. INTRODUCTION

1.1 Background

Fracture conductivity and proppant transport experiments, geared towards understanding the relationships between well stimulation parameters and subsurface characteristics, are inherently difficult to design and execute given the challenges associated with reproducing realistic subsurface scenarios in laboratory settings. Fracture surface topography is critical in informing subsequent experimental results. Given that fracture surfaces are inherently inconsistent, unpredictable, and almost impossible to replicate, a unique challenge is presented across many stimulation experimental workflows.

1.2 Literature Review

The literature review summarized in this chapter offers insights into 3D printing processes and procedures, highlighting areas in which this technology has been employed for application in oil and gas research. This section also reviews recent advancements in fracture conductivity experimental studies and in proppant transport experimental studies, respectively.

1.2.1 3D Printing Processes

3D printing represents a type of additive manufacturing technology that employs materials including thermoplastics, resins, and metals to create a physical object based on a digital 3D model (Tatman et al. 2022). Although there is a plethora of different 3D printing options, there are three main approaches to printing that can be high graded for

appropriate use in laboratory scale research applications: Fused Deposition Modeling (FDM), Stereolithography (SLA), and Digital Light Processing (DLP).

Fused Deposition Modeling (FDM) beings with a digital 3D model that is "translated" into instructions for the 3D printer to follow. More specifically, FDM requires material—which can range from plastics to metal to biogels—to be extruded through a printer nozzle at a softening temperature as the extrusion head follows the appropriate path in the XY plane. After the first layer of material is expelled and cured, the extrusion head is raised a pre-specified height in the Z direction. The procedure is then repeated, this time with the material expelled adhering onto the layer of material below it. This process continues until the entire 3D model has been generated. **Figure 1** illustrates a schematic of this process, in addition to displaying an example of this printer type.

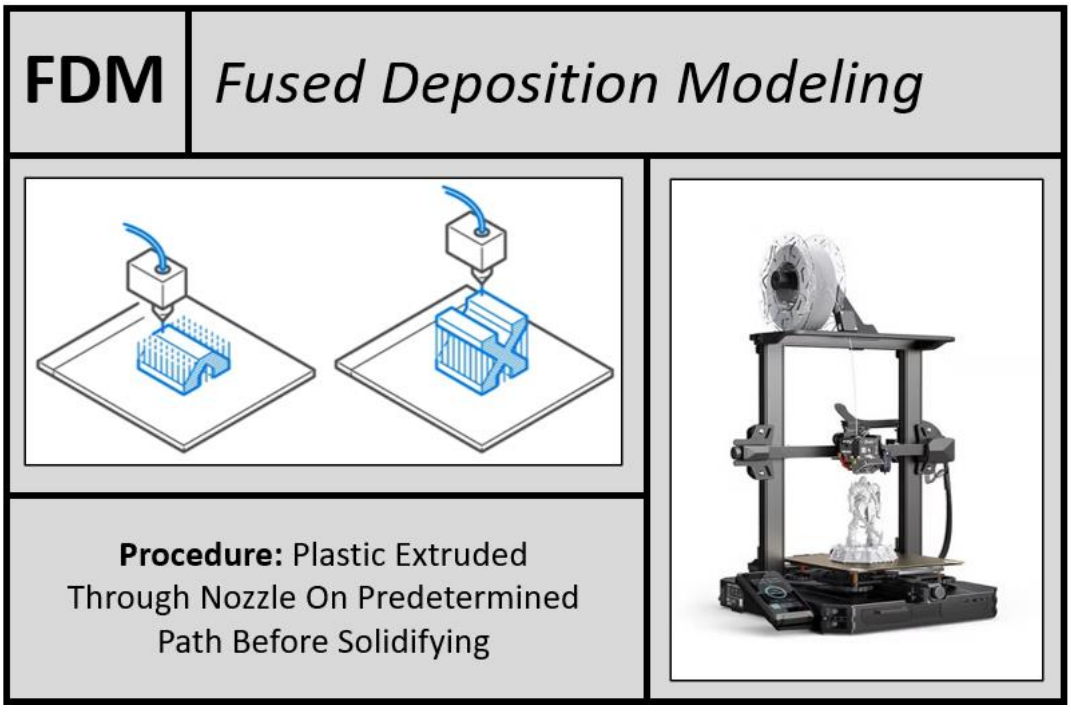

Figure 1: Fused Deposition Modeling (FDM) 3D Printing Process (All3DP, 2023)

FDM as a 3D printing technique offers a lower cost to alternatives and provides an opportunity to use a wide range of materials far more versatile than the thermoplastics typically used in 3D printing procedures. This flexibility comes at the cost of the high dimensional accuracy required for oil and gas research application (Tatman et al. 2022).

Stereolithography (SLA) is a vat polymerization form of 3D printing. SLA 3D printers employ mirrors positioned on the X-axis and Y-axis to aim laser beams across a tub of liquid resin, selectively solidifying a cross-section of the model being printed. The mirrors are adjusted to allow the laser beam to trace over the appropriate path in the XY plane. After the first layer of resin is cured, the build plate is raised in the Z direction. The procedure is then repeated, this time with the resin adhering onto the layer of material above it. This process continues until the entire 3D model has been generated. **Figure 2** illustrates a schematic of this process, in addition to displaying an example of this printer.

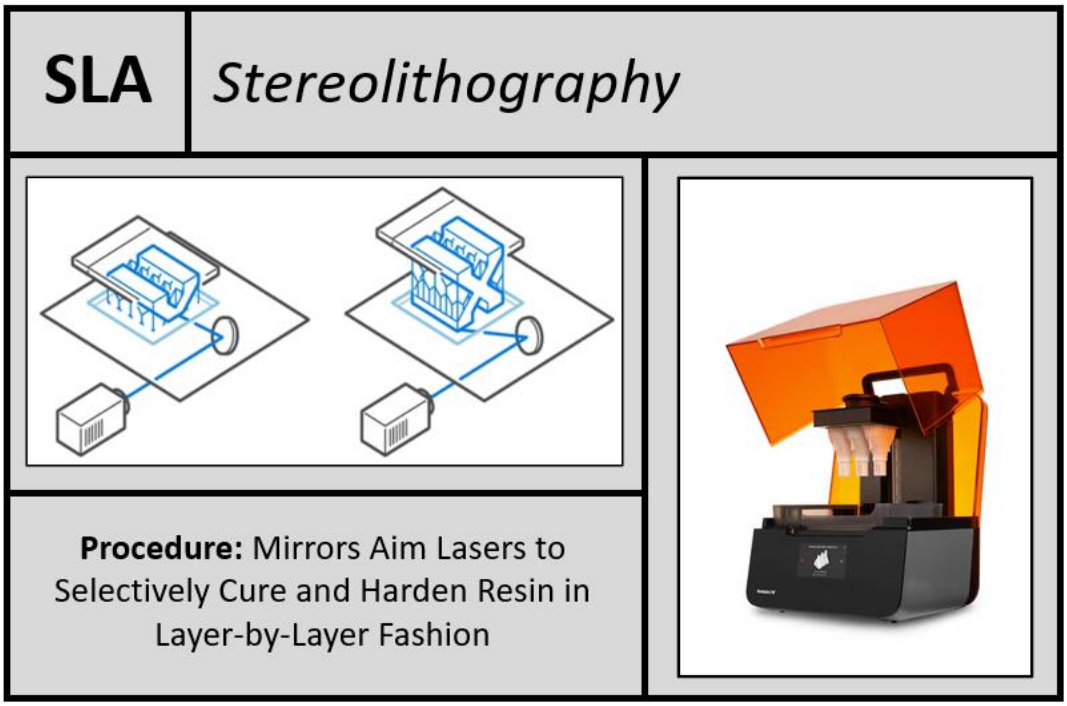

Figure 2: Stereolithography (SLA) 3D Printing Process (All3DP, 2023)

As an alternative to FDM printers, vat polymerization printers—such as SLA—offer much more efficient print times. Additionally, employing lasers as the light source to cure resin offers the stronger light required by some engineering-grade resins. In part because vat polymerization printers can be more expensive than their extrusion-based counterparts, high resolution detail is not sacrificed.

Digital Light Processing (DLP) printers offer another form of vat polymerization 3D printing that allows models to be printed even more rapidly than SLA. DLP printing employs a digital light projector in lieu of a laser beam to project a cross-section of a 3D model onto the liquid resin in the tub above it. This exposure to light selectively hardens the resin, curing it in the shape of the model cross-section. After the first layer of the model solidifies onto the build plate, the plate is raised on the Z-axis and the process is repeated until the entire model has been generated. **Figure 3** illustrates a schematic of this process, in addition to displaying an example of this printer type.

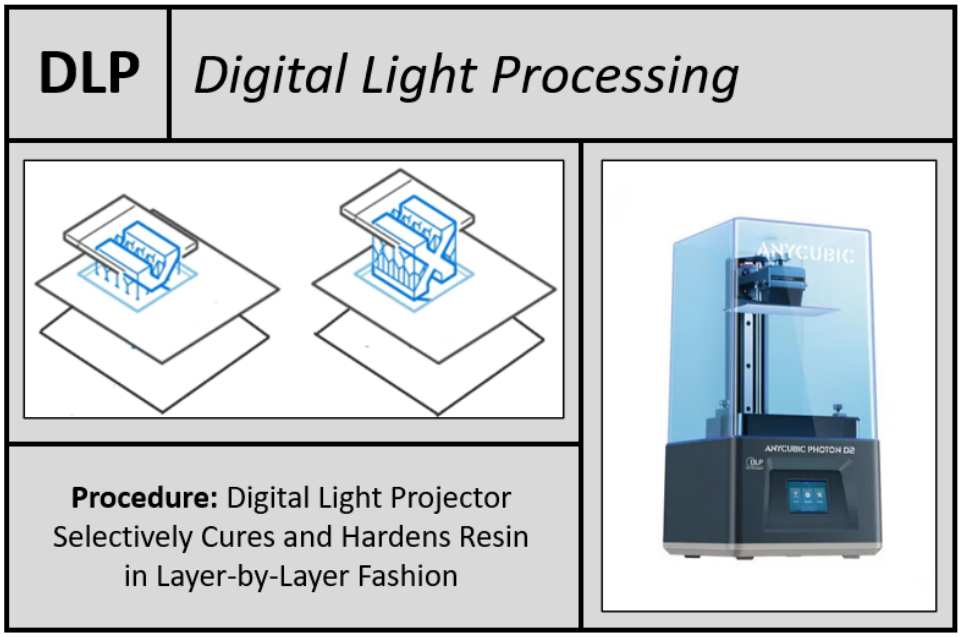

Figure 3: Digital Light Processing (DLP) 3D Printing Process (All3DP, 2023)

DLP 3D printers offer the same benefits as SLA printers—high resolution model outputs and high-strength light sources provided for engineering-grade resins— while also achieving fast model print times. This, of course, is due to the fact that the projected light source characteristic of DLP is able to cure an entire model cross-section at once, while the lasers required by SLA must gradually trace the cross-section of the model.

Figure 4 demonstrates the tradeoff between print time and print resolution discussed briefly above. Given that DLP 3D printers are the best balance of cost, time, size, and resolution—specifically for this laboratory scale application—it was the 3D printing technique carried through the studies discussed in subsequent sections.

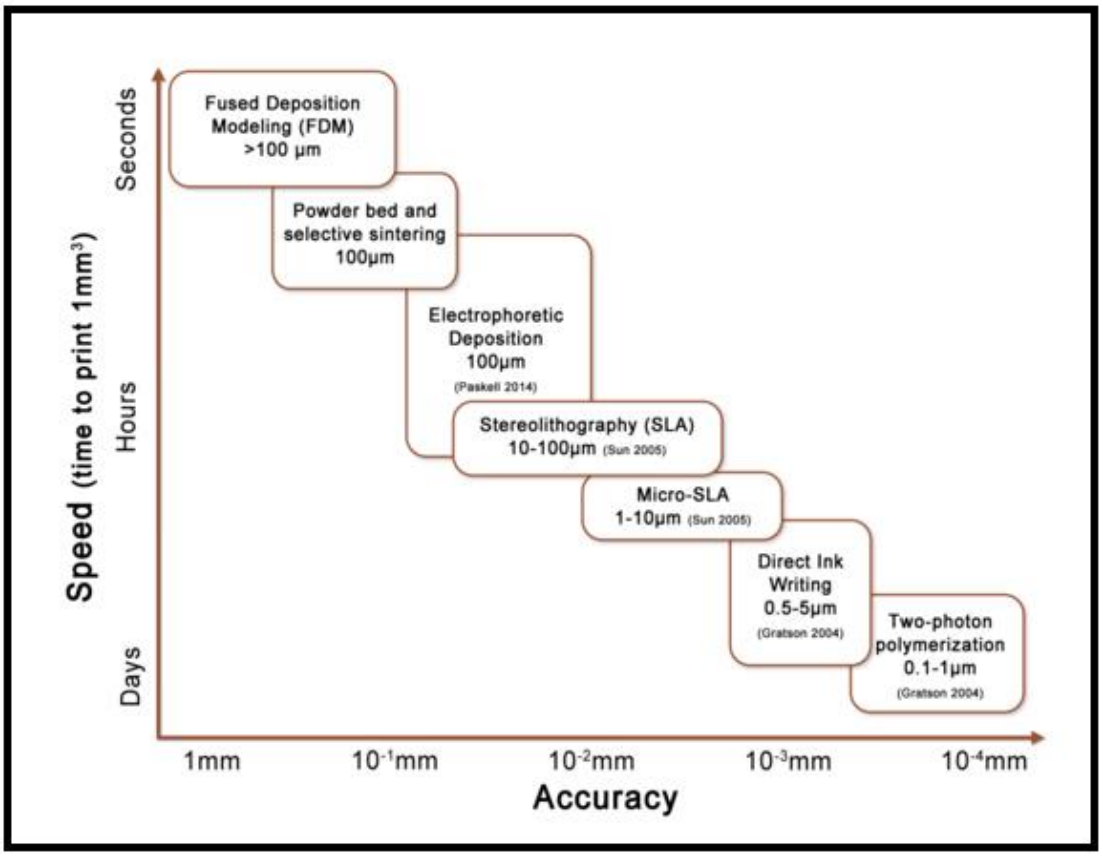

Figure 4: Balance of Resolution / Speed in 3D Printing Techniques (Anderson, 2016)

1.2.2 3D Printing in Oil & Gas Research

As 3D printing continues to become less cost-prohibitive while also achieving higher model resolutions and faster print times, application to oil and gas research at the laboratory scale is becoming increasingly feasible.

For instance, Ma et al. (2023) have attempted to 3D print proxies of reservoir rock from high-resolution micro-CT images. This 2023 publication reviews current 3D printing technologies and assesses the capabilities of these techniques in their ability to appropriately mimic reservoir rock in terms of scale, resolution, accuracy, and repeatability (Ma et al. 2023).

In their efforts to produce a reservoir rock replica 3D model with adequate porosity and permeability, the authors first created a digital core sample by computer-generating a randomly uniform sphere pack and scaling it to appropriate core sample size. Ma et al. (2023) then further processed and converted that digital file to a polygon mesh model, required for 3D printing and most commonly referred to as an ".stl" file. This model was subsequently printed. Micro-CT scan technology was then implemented to compare the 3D print to both the original model (referred to as "Design Model" in **Figure 5**) and model converted to appropriate printing format (referred to as "STL Model" in **Figure 5**). **Figure 5** represents a visual comparison of the three models.

The authors note that, while the 3D print captures most of the detail constructed in the STL model, two-thirds of the porosity built into the original design model was lost when converting the file to an STL model.

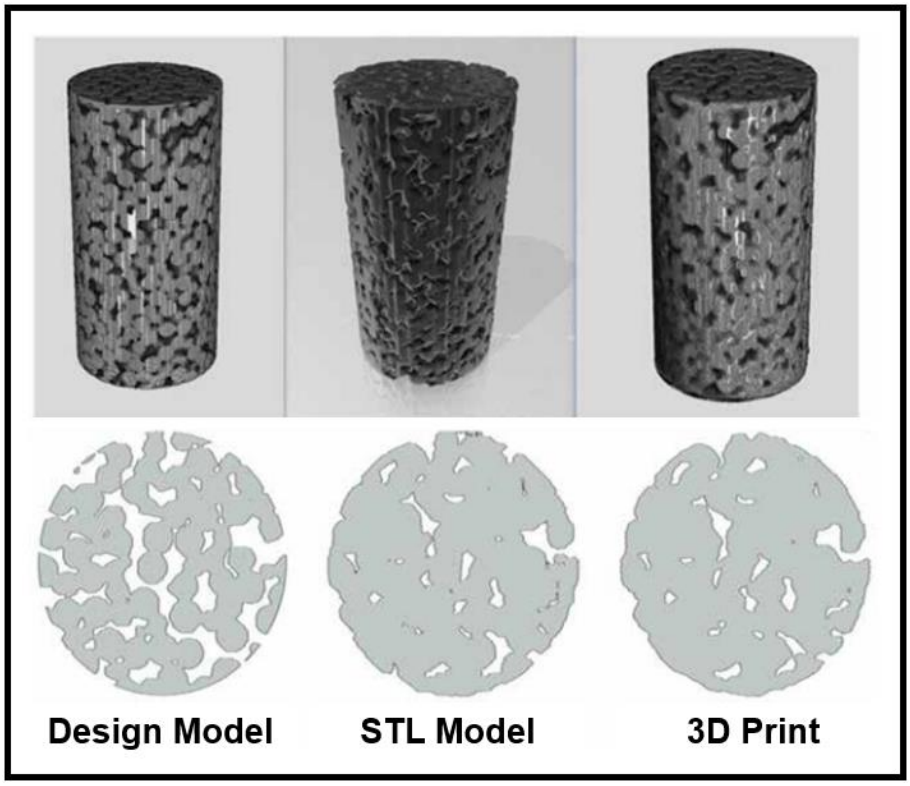

Figure 5: Comparison of 3D-Print with Initial Design / Model (Ma et al. 2023)

While Ma et al. (2023) study findings illustrate some potential for capturing reservoir rock properties on the core plug scale with the help of 3D printing, major conversion issues from digital model to STL model exist and must be resolved before any practical application with this technology is prudent (Ma et al. 2023).

Another area of recent interest adjacent to the aforementioned experimental program is a study geared towards evaluating secondary permeability in a controlled laboratory scale with a 3D-printed discrete fracture network (DFN) model (Baidoo et al. 2022). In this study, a DFN model is built with MoFrac (a commercial DFN generation software). With the help of SOLIDWORKS, this simulated DFN is converted to a 3D physical model and subsequently printed with a 3D printer. The study workflow is summarized in **Figure 6** at the top of the following page.

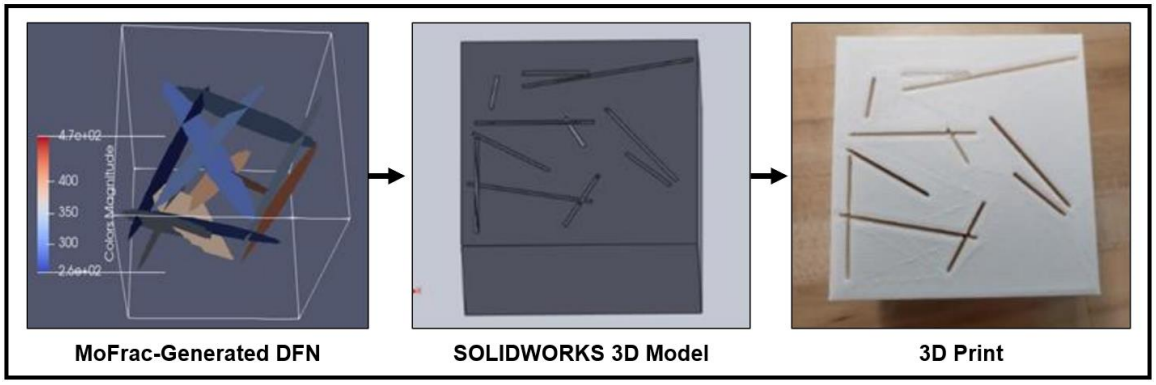

Figure 6: Discrete Fracture Network (DFN) 3D Printing Process (Baidoo et al. 2022)

The 3D-printed DFN model was then employed in an experimental set-up which functioned as a differential pressure meter by restricting airflow through a transition duct (Baidoo et al. 2022). This set-up allowed Baidoo et al. (2022) to assess the behavior of fluid flow through this particular DFN. Study results demonstrate that accurate measurements can be obtained in this experimental set-up with the 3D-printed DFN model shown in **Figure 6**. This study illustrates that 3D printing techniques can be employed successfully to better characterize the influence of fracture intensity, connectivity, aperture, and more on fluid flow through a fracture network (Baidoo et al. 2022).

1.2.3 Fracture Conductivity Experimental Studies

This thesis discusses the application of 3D printing in two experimental studies. These two workflows can be summarized as (1) fracture conductivity and (2) proppant transport. This portion of the literature review aims to highlight fracture conductivity experimental studies that have been conducted to date, while also addressing their respective limitations.

Given that fracture conductivity is critical in determining how prolific a fractured well in a given resource is, significant effort has been made to better understand how the completion design and subsurface characteristics interact to inform fracture conductivity (Sistrunk et al. 2023). For an operator to design the completion best suited for the intrinsic properties of the rock they are hydraulically fracturing, it is imperative that proppant size, proppant strength, and proppant concentration decisions are informed considering stress profiles, elastic properties, surface topography, and mineral composition. Most efforts to understand these interactions to date have been in experimental settings given they are more cost-effective and easier from a logistical standpoint than evaluating these complex relationships on a field-wide scale.

Fracture conductivity is typically investigated experimentally on the laboratory scale using the API Fracture Conductivity Test outlined by the American Petroleum Institute (API). Cooke (1973) was amongst the first experimentalists to investigate how conductivity varies relative to different fluid types, temperatures, and flowrates.

Many of the experimental studies since then have illustrated that rock surface topography and a variety of proppant characteristics are the two primary contributors in determining fracture conductivity (Lai et al. 2019). Because surface topography was identified as a primary informant of fracture conductivity in early experimental studies and because the relationship between the two has proven to be complex to characterize, great emphasis has been placed on better understanding this relationship in existing literature (Enriquez-Tenorio et al. 2019).

Of course, in these experimental studies aimed towards understanding how fluid flows through a fracture, two matching fracture surfaces are required for experimentation. In some studies, rock samples are split in tension to capture surface topography and features as true to the given rock subsurface nature as possible (Sistrunk et al. 2023). This provides a challenge in that reservoir rock is inherently heterogeneous, yielding inconsistent and unpredictable surface topography when broken in tension. This makes it almost impossible to replicate surface topography across multiple rock samples, even when using small samples taken from the same block. The result is an inability to actually isolate and evaluate parameters in a methodical manner which leads to significant uncertainty associated with experimental results (Sistrunk et al. 2023).

One attempt to circumvent this challenge, presented most recently by Brashear et al. (2022), is to employ sawcut rock samples with smooth fracture faces in lieu of rough surfaces. Recall that the two primary contributors in determining fracture conductivity are reservoir rock properties and proppant size, quality, and concentration. Smooth-surface fractures are a great tool that allow for isolation and evaluation of the impact of proppant size, strength, concentration, and more on fracture conductivity, but this approach leaves the experimentalist unable to characterize the relationship between surface topography and conductivity. While saw-cut fractures allow for methodical evaluation of proppant properties, the relevance of these results can be disputed given that the conductivity of these smooth-surface samples varies significantly relative to their rough fracture surface counterparts (Zhang et al. 2013).

Pena et al. (2016) recognized and attempted to resolve the shortcomings associated with inconsistent and unpredictable rock samples. The authors acknowledged that failing

to replicate rock samples with consistent surface topographies and reservoir properties can yield inconsistent or even incorrect conclusions. They took steps to evade this limitation by testing each set of samples in their experimental study multiple times (Pena et al. 2016). After analyzing results, Pena et al. (2016) concluded that this methodology was not entirely effective in reducing uncertainty associated with experimental results given that changes in elastic mechanical properties through the first and subsequent loading cycles led to persistent variation in resulting conductivity values.

Perhaps the most effective attempt in resolving the challenges associated with reproducing rock samples that are inherently difficult to replicate was presented by Chen et al. (2021). This study—similar to the work presented in this thesis—prioritizes capturing a wide and realistic range of subsurface fracture topographies while also striving to reduce uncertainty associated with results by replicating these surfaces with precision.

Chen et al. (2021) seek to do this by breaking a given rock sample in half with tension to produce matching fracture surfaces, scanning and processing these rough fracture surfaces with laser technology, and employing these measurements to produce nearly identical samples with digital engraving technology. Chen et al. (2021) leverage this methodology to execute conductivity experiments on samples with uniform surface morphology and consistent mechanical properties. Again, similar to the study presented in subsequent sections, the authors carefully evaluate the accuracy and precision of the procedure to reproduce identical samples as outlined above. They conclude that there is little difference in the topography elevation distribution between the original rock sample and the sample that was reproduced with digital engraving technology (Chen et al. 2021). **Figure 7** illustrates a direct comparison of the two surface distributions.

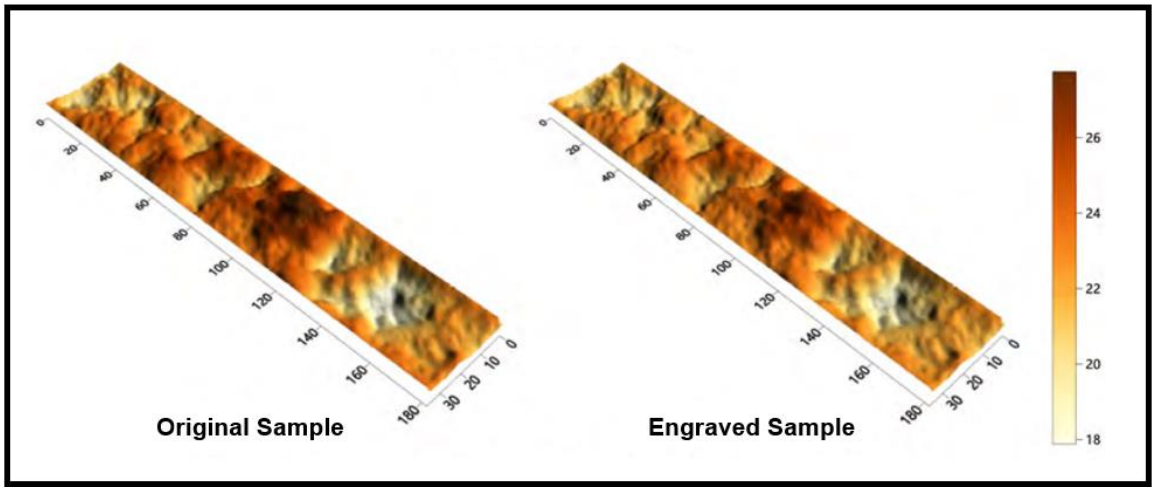

Figure 7: Comparison of Original Shale to Engraved Replica (Chen et al. 2021)

After successfully illustrating that their methodology results in the generation of identical conductivity samples, Chen et al. (2021) carried out an experimental study with results illustrating that propped fracture conductivity is most significantly impacted by proppant properties and fracture surface topography, especially at low proppant concentrations.

Although Chen et al. (2021) are able to propose a comprehensive approach to circumventing the study limitations outlined above, there are both significant cost and significant time constraints associated with using the digital engraving technology described in their proposed workflow.

The study summarized in this thesis prioritizes consistency in experimental samples while preserving the natural surface topography of the rock by employing 3D printing technology. Subsequent sections will explore in detail how this was achieved.

1.2.4 Proppant Transport Experimental Studies

Similar to fracture conductivity, how effectively proppant is transported through a fracture network and subsequently distributed throughout that network is a key determining factor in the success of a fracture treatment.

Kern et al. (1959) were amongst the first to recognize and study the importance of proppant distribution and transportation in a fracture network. In their efforts to study this phenomenon, Kern et al. (1959) employed the first slot-flow experiment, where slurry comprised of just water and proppant was pumped through two smooth glass sheets (each approximately two feet long) placed 0.25 inches apart from one another. This experimental set-up is illustrated in the schematic displayed in **Figure 8** below.

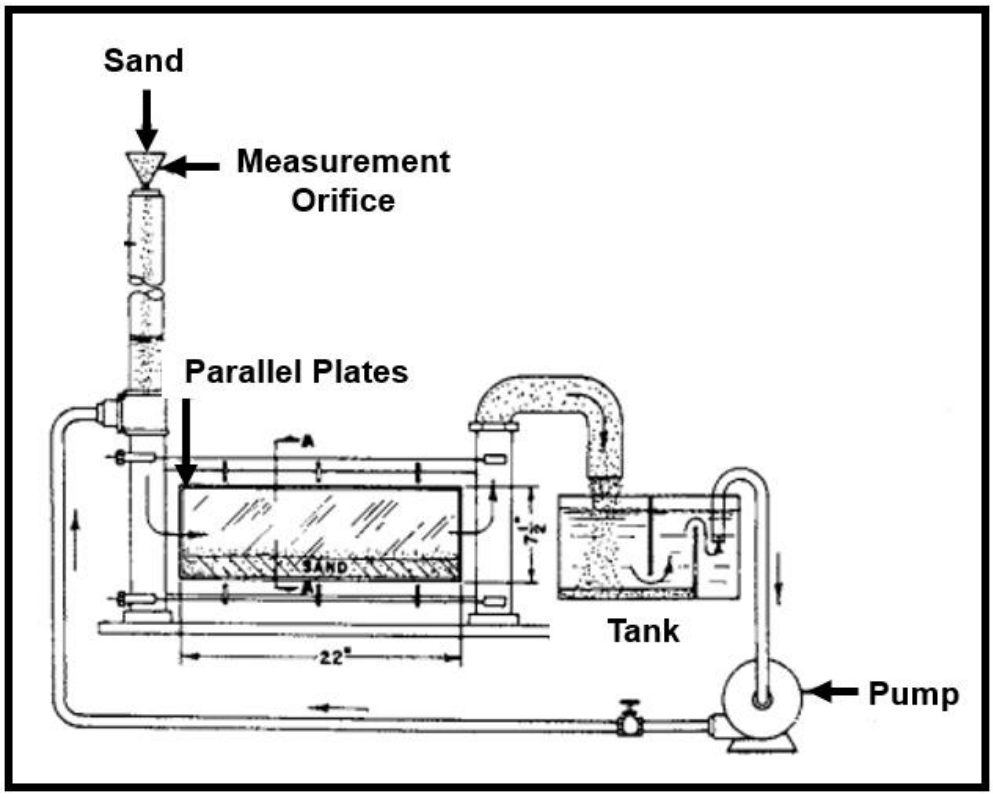

Figure 8: Proppant Transport Experimental Apparatus (Kern et al. 1959)

Through the use of the apparatus illustrated in **Figure 8**, Kern et al. (1959) concluded that a bed of settled proppant will build up towards the bottom of a fracture unless the injection rate passes some upper threshold. They further noted that proppant injected towards the end of the treatment will wash over this previously settled sand bed. An illustration of the resulting proppant dune between the two smooth glass fracture faces is illustrated in **Figure 9** below.

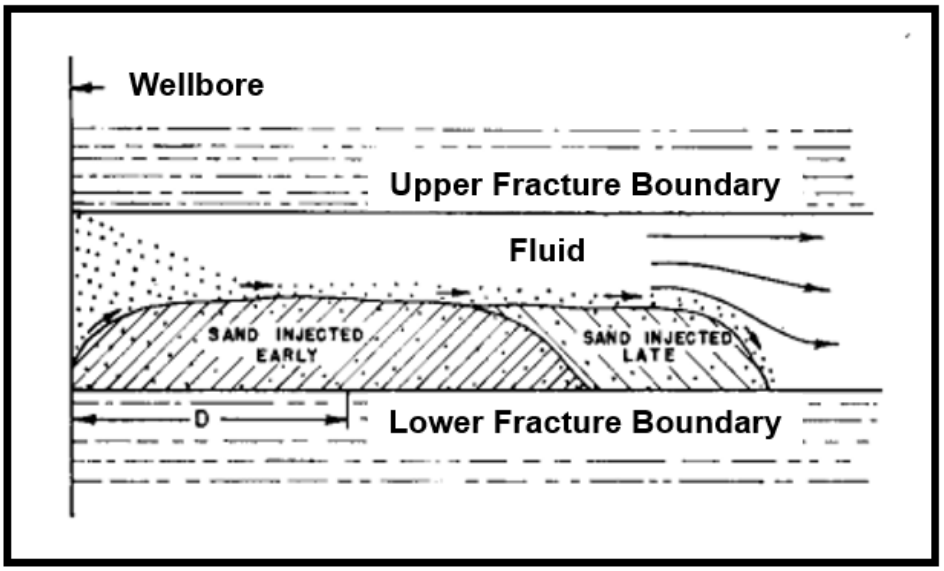

Figure 9: Post-Fracture Treatment Settled Proppant Dune (Kern et al. 1959)

The foundation of these proppant transport and distribution experiments remains largely unchanged to date. That being said, there are many studies working to layer in additional subsurface complexities to make proppant transport and distribution analyses more modern and comprehensive.

Several such examples of this are presented in studies conducted by Alotaibi & Miskimins (2020) and Bahri & Miskimins (2021). Both of these studies aim to better understand proppant transport and distribution in subsidiary fractures, long believed to have lower propped area relative to primary fractures associated with higher fluid velocities

(Alotaibi & Miskimins, 2020). Both experimental programs employ the apparatus illustrated in **Figure 10** below to analyze proppant transportation and settling in secondary and tertiary fractures.

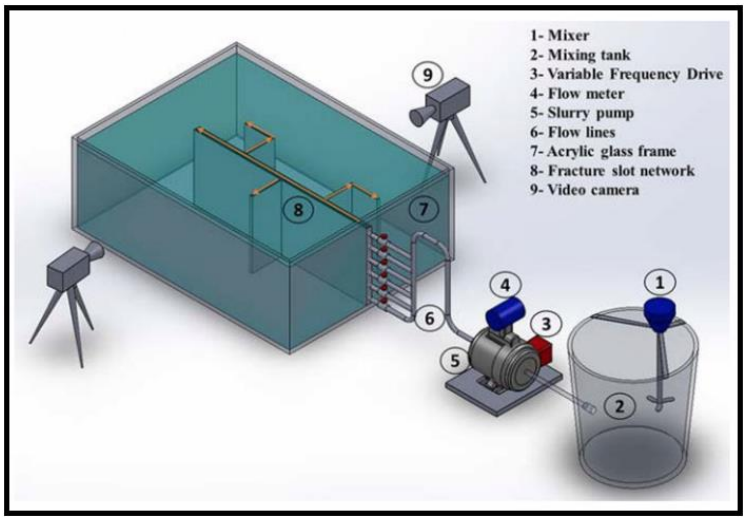

Figure 10: Proppant Transport Experimental Apparatus (Bahri & Miskimins, 2021)

Qualitative results from both studies were documented in pictures—like that displayed in **Figure 11** below—and subsequently analyzed to better understand how proppant size, fluid density, fluid rate, and fracture complexity all interact to inform proppant transport and distribution (Bahri & Miskimins, 2021).

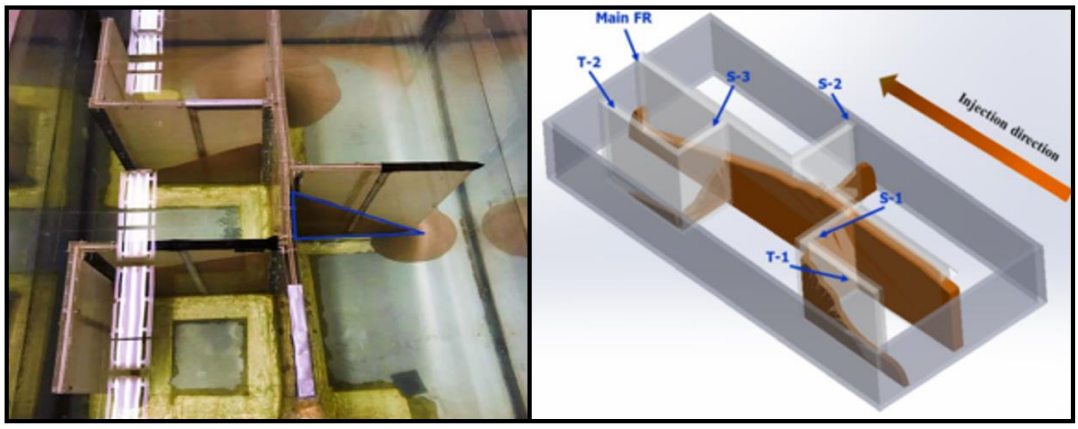

Figure 11: Top View of Post-Injection Dune Shapes (Bahri & Miskimins, 2021)

This thesis aims to incorporate another layer of subsurface complexity by creating a fracture network for proppant transport experimentation characterized by rough-wall fracture surfaces. Subsequent sections will explore in detail the approach that was taken in executing this.

1.3 Problem Description and Objectives

Again, experimental studies geared towards understanding the relationships between well stimulation parameters and subsurface characteristics are inherently difficult to design and execute given the challenges associated with reproducing realistic subsurface scenarios in laboratory settings.

The first part of the study in this thesis aims to demonstrate that 3D printing can be employed to generate identical high-strength cement samples with geostatistically-informed rough fracture surfaces, in addition to exhibiting that this high-strength cement is an adequate proxy for unconventional reservoir rock in fracture conductivity experiments.

The second portion of the study outlined in this thesis serves to highlight the workflow that has been established for 3D printing a rough fracture network to be used in proppant transport experimentation.

Given that fracture surface topography is instrumental in informing results across both fracture conductivity and proppant transport stimulation experimental workflows, great care is taken in establishing and vetting a method to inform rough fracture surfaces with geostatistical parameters.

1.4 Content of Thesis

The content of this thesis is presented in four chapters. The first chapter provides comprehensive background information in the form of a literature review, problem description, and objectives outline. The literature review serves to provide context on existing studies relevant to the work presented in this thesis regarding 3D printing processes, 3D printing in oil and gas research, fracture conductivity experimental studies, and proppant transport experimental studies.

The second chapter presents the introduction, methodology, results, discussion, and conclusions associated with the fracture conductivity study summarized in this thesis. This study aims to summarize innovation achieved in amending fracture conductivity experimental workflows to be more robust.

The third chapter is also organized in sections representing the introduction, methodology, results, discussion, and conclusions, but serves instead to summarize the proppant transport study in this thesis. This study is geared towards amending proppant transport experimental inputs to be more complex and informative.

The fourth and final chapter in this thesis serves to review the major takeaways from both stimulation studies described above, in addition to highlighting study limitations and future work.

2. FRACTURE CONDUCTIVITY [*]

2.1 Introduction

This chapter presents the workflow organized to generate identical high-strength cement samples with geostatistically-informed rough fracture surfaces, in addition to exhibiting that this high-strength cement is an adequate proxy for unconventional reservoir rock in fracture conductivity experiments.

The primary objective of the study presented in this chapter was to prioritize consistency in rock samples, while also preserving a realistic subsurface fracture topography of unconventional reservoir rock.

A rough fracture surface is first simulated with a group of geostatistical parameters serving as inputs to a geostatistical library. The output simulated rough fracture surface is then scaled to the appropriate size for fracture conductivity experimentation and printed with a Digital Light Processing (DLP) 3D printer.

Following this, the 3D print is used to create a rubber silicone casting. High-strength cement is poured into this casting after it has finished curing. This cement serves as a proxy for unconventional reservoir rock in future conductivity experiments. Each casting characterized by a respective rough fracture surface can be used to produce as many identical "rock" samples as necessary for experimentation. This process is repeated for as many different surface morphologies as the experimental study plans to incorporate.

[*] Part of this chapter is reprinted with permission from "The Effect of Fracture Surface Roughness on Propped Fracture Conductivity Using 3D-Printed Fracture Surfaces" by Sistrunk, C., Brashear, A.T., Zhu, D., Hill, A. D., and T. Tajima, 2023. *OnePetro*, SPE-213032-MS, Copyright 2023 by Society of Petroleum Engineers.

2.2 Methodology

To generate identical conductivity samples, reducing uncertainty associated with experimental results, the following procedure is employed:

1) Simulate Rough Fracture Surface
2) Generate 3D Model for 3D Printer
3) Prepare 3D Model for 3D Printer
4) Print 3D Model
5) Post-Process 3D Print
6) Create Sample Mold
7) Produce Cement Samples
8) Execute Fracture Conductivity Experiments

Each subsection in this chapter represents a step in the procedure outlined above.

2.2.1 Simulating Rough Fracture Surface

Given the importance of surface topography in determining fracture conductivity, it is critical to come up with a workflow, not just to generate identical conductivity samples, but also to ensure that these identical surfaces are geostatistically informed. In their efforts to do just this, Tatman et al. (2022) demonstrated a procedure to characterize and simulate rough fracture surfaces with GSLIB, a geostatistical software library created by Stanford University (Deutsch & Journel, 2017). In applying this methodology, a set of geostatistical parameters—mean, standard deviation, correlation length in the X direction, and

correlation length in the Y direction— are input into a geostatistical library to generate a rough fracture surface with the appropriate responding surface characteristics.

Given the statistic distribution of a rough surface, mean and standard deviation are straight-forward to determine. To determine the correlation length in either direction of a given rough fracture surface, a variogram—such as that pictured in **Figure 12** below—is used.

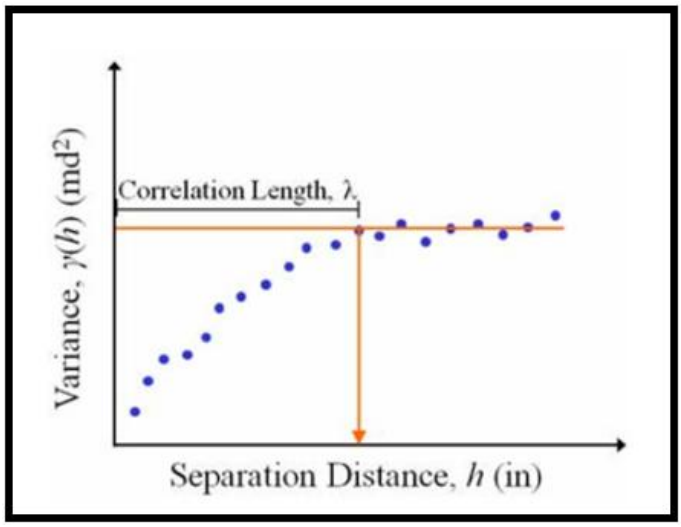

Figure 12: Correlation Length Illustrated on Variogram (Tatman et al. 2022)

The correlation length is defined by the separation distance at which the variance of a given surface distribution approaches its respective asymptote (Isaaks and Srivastava, 1989). The variance is defined in **Equation 1** below.

$$\gamma(h) = \frac{1}{2N}\sum_{i=1}^{N}(z_i - z_{i+h})^2 \quad \textbf{(1)}$$

Again, mean, standard deviation, correlation length in the X direction, and correlation length in the Y direction are all geostatistical inputs that can be amended to

generate varied rough surfaces. **Figure 13** demonstrates what changes to these geostatistical inputs look like from a qualitative standpoint.

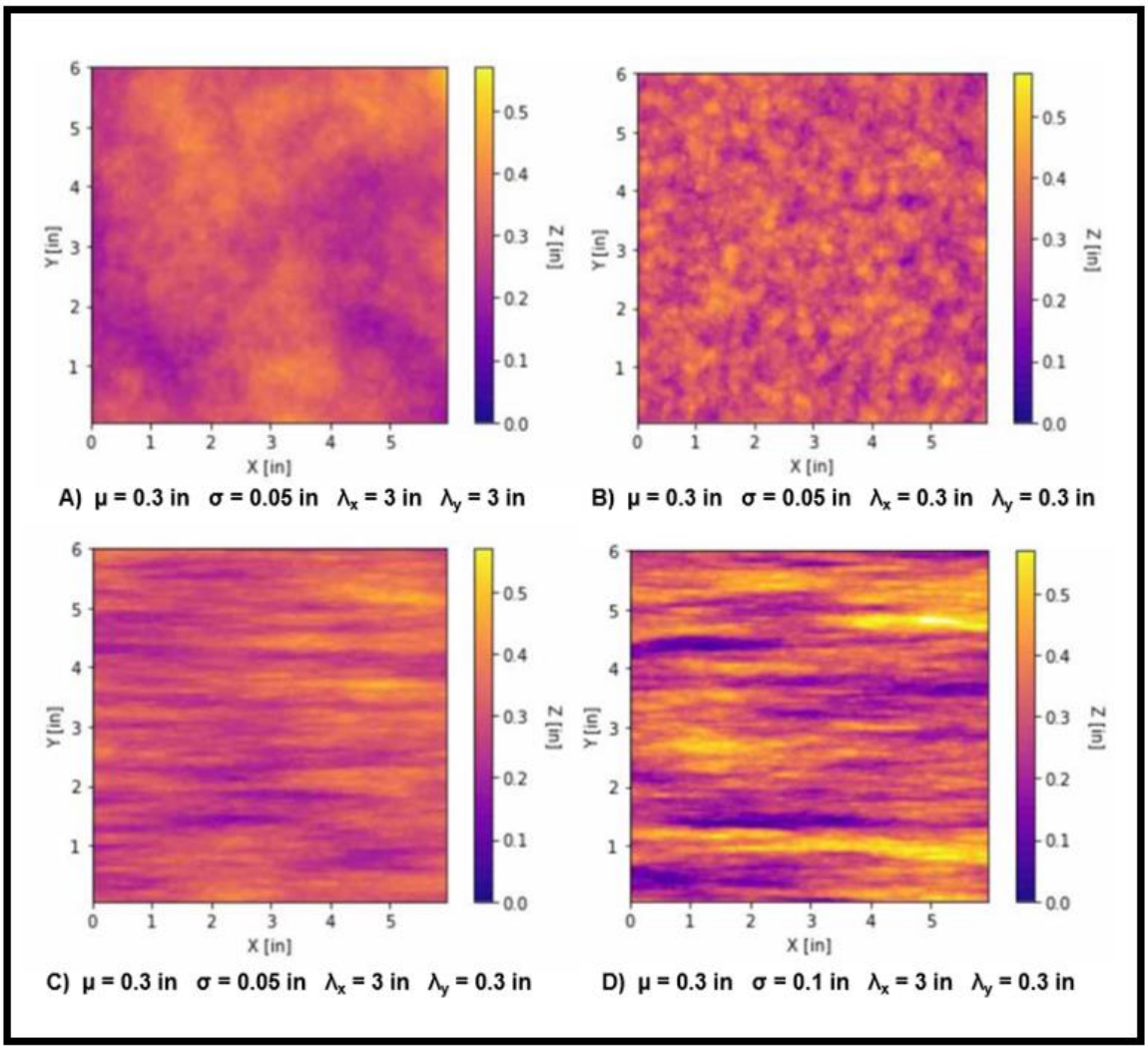

Figure 13: Rough Surfaces with Varied Geostatistics (Reprinted from Sistrunk et al. 2023)

All of the simulated surfaces displayed above are identical in size: six inches in the X direction and six inches in the Y direction. Each simulation carries the same mean, which represents the average height of the surface in the Z direction. Because **Figure 13A** has equal correlation length in the X direction and in the Y direction, the height of the surface

in the Z direction shows no particular affinity for features in either direction on the plane. This remains true for **Figure 13B**, which is also characterized by equal correlation lengths in both directions. Because the correlation length in both directions is reduced by a factor of ten in **Figure 13B** relative to **Figure 13A**, changes in height in both directions occur much more frequently on this surface. Because the surface simulated and displayed in **Figure 13C** was characterized by correlation length in the X direction an order of magnitude greater than correlation length in the Y direction, changes in height occur over shorter distances in the Y direction. Features across the surface show a particular affinity for the X direction, across which change in height occurs much more gradually. Finally, **Figure 13D** demonstrates that doubling the standard deviation of a surface while holding other parameters constant results in more dramatic changes in the magnitude of the height across the simulated surface (Sistrunk et al. 2023).

The methodology portion of this chapter represents the proof-of-concept work used to demonstrate that the workflow outlined above is adequate in achieving study objectives. For this proof-of-concept work, a mean of 0.3 inches, a standard deviation of 0.05 inches, a correlation length in the X direction of 3 inches, and a correlation length in the Y direction of 3 inches, were all used to characterize and simulate one square foot of rough fracture surface to be used in the following subsections.

2.2.2 Generating 3D Model for 3D Printer

It is important to note that the simulated rough fracture surfaces displayed in **Figure 13** do not actually represent one continuous surface, but rather a series of coordinates spaced tightly together. In order to produce a 3D model appropriately formatted for 3D

printing, this computer-generated series of points must be processed and converted into a polygon mesh model. This is most commonly referred to as an ".stl" file, which represents the geometry of a 3D object in a manner that makes the file compatible with a variety of applications including prototyping, 3D printing, and computer-aided manufacturing.

Tatman et al. (2022) explain that this file type represents 3D objects as an amalgamation of small triangles that fully describe the surface geometry of the associated object. This process is executed with an in-house Python code and is illustrated in **Figure 14** below on a previously generated rough fracture surface. Also executed with an in-house Python code is a process to generate the opposite and matching fracture face following the conversion of the simulated surface to an ".stl" file.

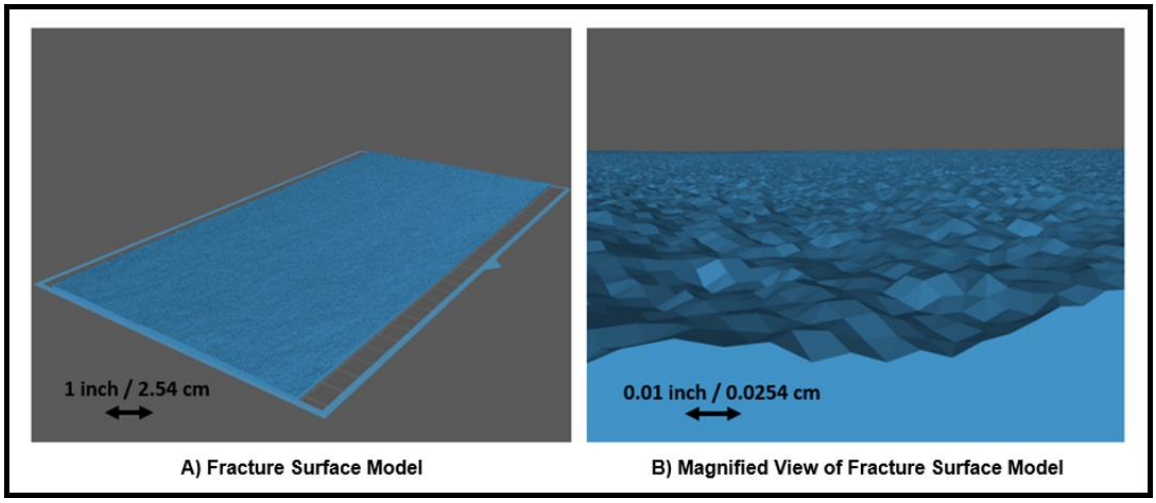

Figure 14: Simulated Coordinates Converted to 3D Model (Tatman et al. 2022)

Even following the conversion of the simulated rough fracture surfaces to two continuous 3D models (one surface representing the original simulated surface and another surface representing its mirror image), additional steps must be taken to scale the generated rough surfaces to the appropriate size. The API Fracture Conductivity Test, as outlined by

API, requires precise sample dimensions for successful experimentation. The required sample size for the modified-API conductivity cell used in the aforementioned experimental workflow is roughly 7 inches long and 2 inches wide, with rounded semi-circles on the short sides of the sample. The height of the conductivity sample can be varied as necessary and adjusted prior to experimentation.

ChiTuBox—a popular 3D printing pre-processing software— can be used to scale the 12-inch long by 12-inch wide rough surfaces that were originally generated and meshed into two continuous matching surfaces to be the appropriate size (CBD-Tech, 2021). While there are a variety of approaches that can be taken to scaling the rough fracture surfaces to conductivity sample size, ChiTuBox offers a "Boolean" operation that can be employed to easily cut the desired geometry of the fracture conductivity sample from a large, simulated fracture surface.

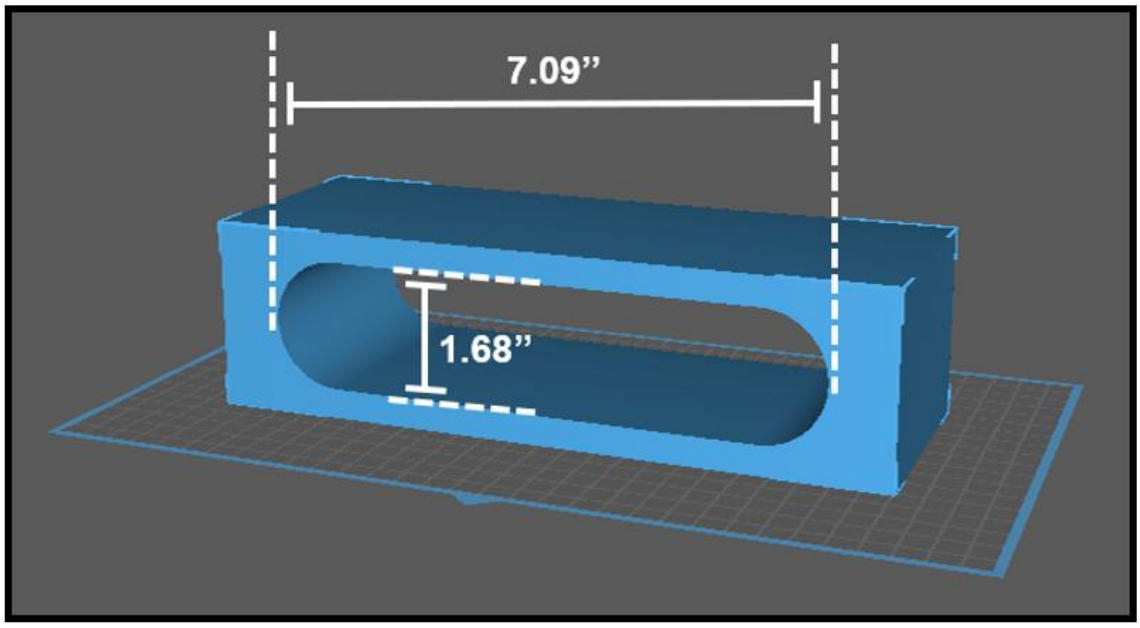

Figure 15: Conductivity Sample Cell Model Employed to Scale Rough Surface

ChiTuBox's "Boolean" operation simply allows the user to subtract one surface geometry from another. For this process, a conductivity sample cell model is used and is displayed in **Figure 15** on the previous page. After both the sample cell model and previously generated fracture surface are imported into ChiTuBox and aligned appropriately, their surface geometries can be subtracted from one another. The regions of the models that fail to intersect—in this case the desired 3D model of a conductivity sample—are left behind (Tatman et al. 2022). This operation is illustrated in **Figure 16**.

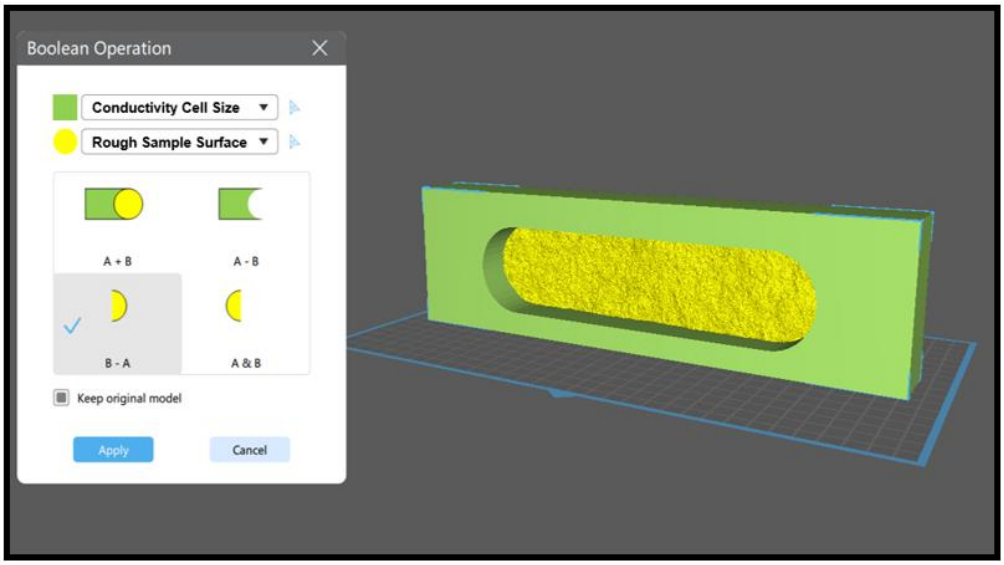

Figure 16: Sizing Rough Sample Surface with ChiTuBox "Boolean" Operation

This operation must be completed for both halves of the 3D conductivity sample models representing matching fracture faces. Following this, the remaining two 3D models can be prepared for 3D printing.

2.2.3 Preparing 3D Model for 3D Printer

Up to this point, the workflow outlined in the steps above has illustrated how to simulate a rough fracture surface with geostatistical inputs, how to appropriately convert

that simulated surface into a 3D model, and how to scale that 3D model to the size required for fracture conductivity experiments. An example of the resulting matching fracture faces—sized appropriately and characterized with geostatistical parameters—is displayed in **Figure 17** below.

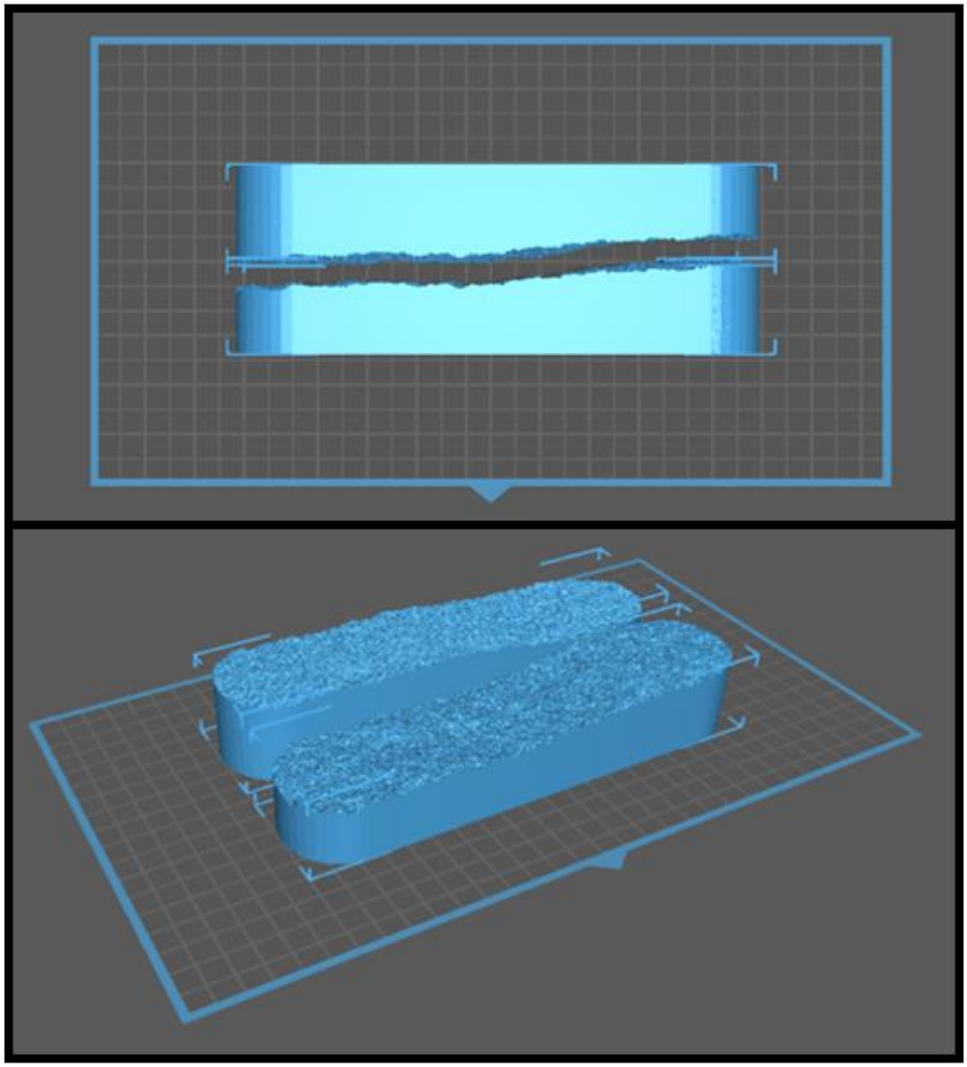

Figure 17: 3D Model Cell with Simulated Roughness (Reprinted from Sistrunk et al. 2023)

Prior to printing the 3D model displayed in **Figure 17**, appropriate steps must be taken to give the model the best opportunity for a successful print as is possible. First, both

halves of the conductivity sample 3D model should be hollowed with the ChiTuBox function “Hollow”. This lightens the weight of the 3D print, reducing the stress on the connection point where the model adheres to the build plate. Lightening the 3D print maximizes the probability of a successful outcome on the first attempt.

Additionally, because each cross-section of the model is printed one at a time while fully submerged in a tub of liquid resin—and because each cross-section of the model is now hollow—orienting the print to minimize the cross-sectional area being printed at a given time reduces the risk that the model will suction off of the build plate and onto the flexible plastic filament protecting the LCD screen. To do just that, model supports are fashioned to angle the 3D model such that the cross-sectional area being printed at a given time is minimized. These supports also provide a foundation for the 3D print so that it does not begin to sag and change shape under its own weight. These supports are easily removed after the print is complete. The resulting 3D model adequately prepared for printing is displayed in **Figure 18** below.

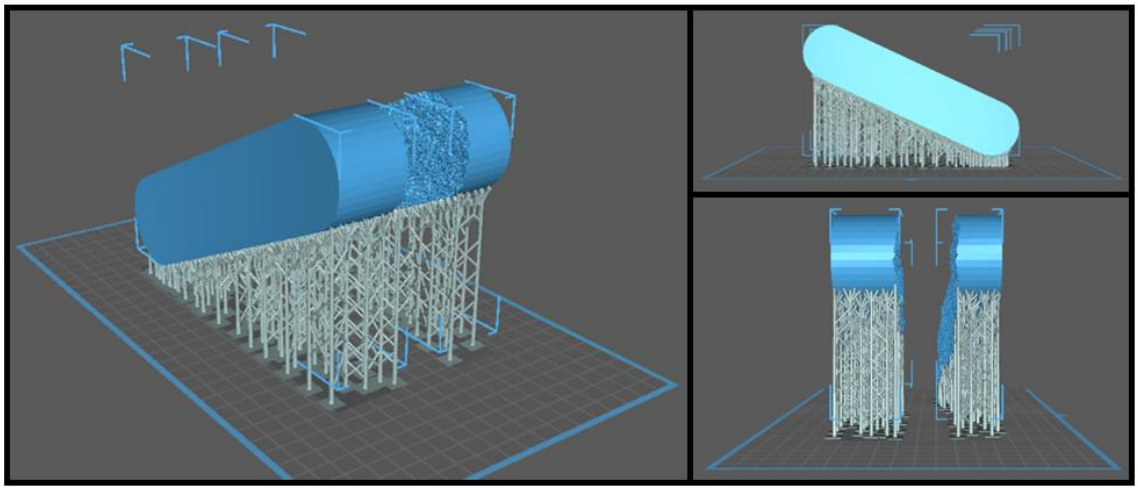

Figure 18: 3D Model Orientation Prior to 3D Printing (Reprinted from Sistrunk et al. 2023)

2.2.4 Printing 3D Model

As mentioned previously, this study employs a Digital Light Processing (DLP) 3D printer to print the 3D models required for experimentation. More specifically, this study leverages a Phrozen Transform Fast 3D Printer, pictured in **Figure 19**.

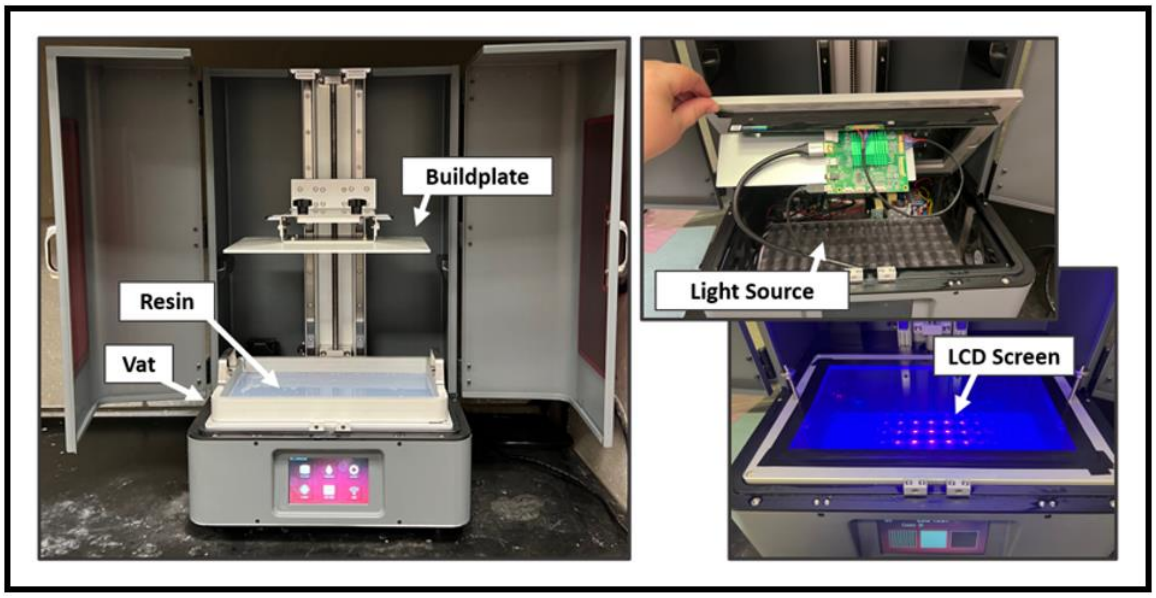

Figure 19: Phrozen Transform Fast 3D Printer (Reprinted from Sistrunk et al. 2023)

Recall that DLP printers are unique in that they leverage one light source in the form of an LCD screen to selectively cure, or harden, liquid resin. More specifically, the build plate pictured in **Figure 19** above is slowly lowered into a vat of liquid resin. Difficult to see in the image above, but critical in understanding the printing procedure, is a clear plastic filament called the FEP (Fluorinated Ethylene Propylene) sheet. The FEP sheet holds liquid resin in the vat while allowing light from the LCD screen to be transmitted up from the screen and into the tub of resin. The ultraviolet screen in the housing of the printer displays a cross-section, or a "slice", of the 3D model being printed. When the liquid resin

is exposed to light from the LCD screen below, it hardens. After a cross section of the model has cured onto the build plate, the plate is raised on the Z-axis, the next "slice" of the object is displayed on the screen, liquid resin hardens where it is exposed to this light onto the previous model layer, and the Z-axis moves up once again. This process is repeated until the entire model has been generated. An example of what this conductivity sample 3D model looks like halfway through printing is illustrated in **Figure 20**.

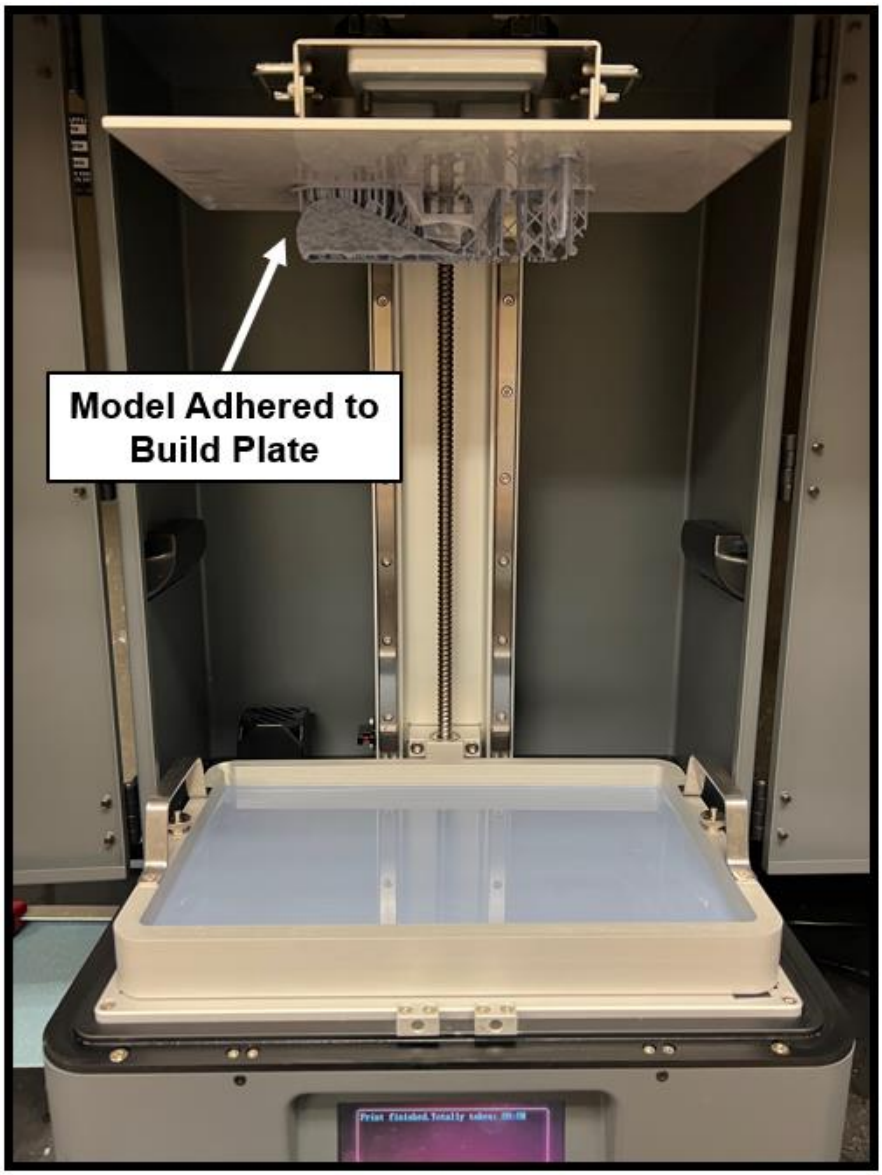

Figure 20: Model Adhered to Build Plate Halfway Through Print Process

The Phrozen Transform Fast uses a 13.3'' Mono-LCD screen and has a print volume 11.5 inches wide, 6.5 inches deep, and 15.8 inches high. The maximum XY resolution of the printer is on the order of microns at 0.0018 inches. It is important to note that prior to actually printing the 3D model in the procedure outlined above, there are three additional steps that must be taken to ensure a successful print on the first attempt: (1) leveling the build plate, (2) calibrating exposure time, and (3) slicing the 3D model with the correct printer settings. Each of these steps is discussed thoroughly in the following three subsections.

2.2.4.1 Leveling the Build Plate

Prior to actually 3D printing any models, the build plate must be leveled to ensure that the Z-axis of the machine is calibrated correctly. This should be done at least once annually and each time the printer is moved, even across small distances. Failing to calibrate the Z-axis correctly will cause significant damage to the printer. The following steps can be taken to level the build plate:

1) Clean the resin vat and build plate with isopropyl alcohol to ensure there is no residual resin or foreign objects remaining that could potentially puncture the FEP sheet or the LCD screen.
2) Use a hex wrench to loosen the four screws on the side of the build platform. The plate should now be hanging freely and should respond by moving when pressure is applied to it.
3) Select "Z-Axis" on the home screen of the digital printer interface.
4) Use the arrows—highlighted in **Figure 21**— to adjust the build plate until it is flush with the FEP sheet on top of the LCD screen.

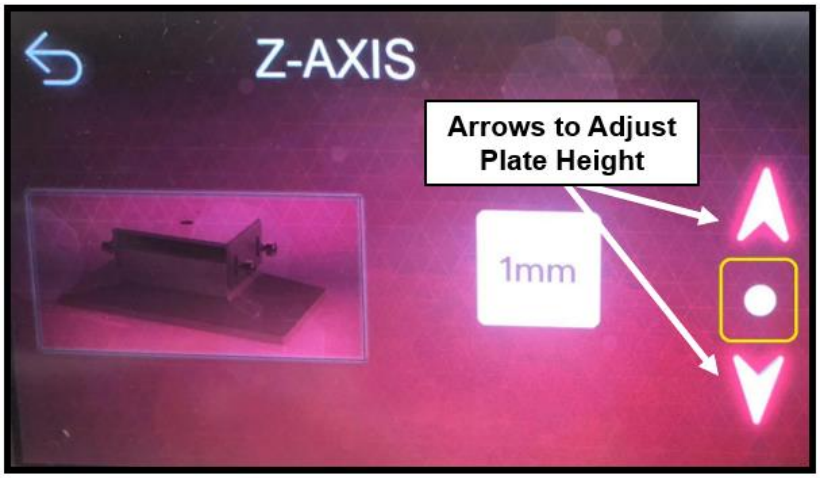

Figure 21: Adjusting Z-Axis Height with Printer User Interface (Tatman et al. 2022)

5) Replace the screws previously removed from the side of the build platform and tighten with the hex wrench. Over-tightening will strip the screws.
6) Select "Done" in the printer digital interface. The build plate will then be raised automatically to the top of the Z-axis.
7) Ensure that the build plate is secure by applying pressure to the edges of the platform and ensuring there is no resulting movement. After confirming the build platform is secure and level to the eye, the leveling process is concluded.

2.2.4.2 Calibrating Exposure Time

Recall that Digital Light Processing (DLP) 3D printers cure resin by selectively exposing one cross section, or model "slice", at a time to light. In achieving a successful print on the first attempt and avoiding any damage to the 3D printer, it is critical to adjust printer settings for the shape and size of the model being printed, for the strength of the machine's light source, for the resin being used, and even for the humidity and temperature of the environment outside. This subsection focuses on the most important of these setting

adjustments, which is the duration that resin is exposed to light for in order to cure each "slice", or cross-section, of the 3D model. This is known as the model "Exposure Time".

Resin that is overexposed to UV light will swell and harden the model, while washing out more minute details. Resin that is underexposed to UV light may result in missing model parts, less resolution, and even failure for the model to adhere to the build plate at all. Given that fracture conductivity experiments require precision on the order of microns, it is critical to the integrity of the experimental study that 3D models are not over or underexposed. As such, an exposure time calibration should be conducted at least every few weeks, when a new resin is being used, when the LCD screen or FEP sheet are replaced, or in response to seasonal changes in temperature and humidity.

In summary, the following procedure should be followed when calibrating exposure time for a given machine, resin, and model:

1) Load the "Resin XP2 Validation Matrix" (displayed in **Figure 22**) into ChiTuBox.
2) Create a new resin profile in the "Prepare" window in ChiTuBox.
3) Adjust the "Bottom Layer Count" to be 4. In 3D printing, "Bottom" refers to the settings applied only to the bottom-most layers of the model. This adjustment should be made given that the calibration model to be printed is only 30 layers in total (assuming a layer height of 0.05 mm). If this setting is not reduced from the default of 20 layers, almost the entire model will be cured with the default "Bottom Exposure Time" of 20 seconds. Not amending these settings appropriately will dictate that layers of the model are cured with 20 seconds of exposure, rendering calibration useless.
4) Set the "Exposure Time" to 1.5 seconds.

5) Ensure all other resin profile settings are set to their respective default values.
6) Close out of the “Slice Settings” menu.
7) Select the model to be printed in ChiTuBox. Select the appropriate resin profile created in previous steps.
8) “Slice” the model by selecting “Single Parameter Slice” in ChiTuBox. This process may take ChiTuBox up to an hour to complete.
9) Save the sliced model and model instructions by selecting “Save” in ChiTuBox. Save the resulting “.zip” file to the computer.
10) Duplicate the “.zip” file. In the duplicated file, change the “.zip” distinction to “.phz”. This will result in a file name extension warning which can be dismissed.
11) Load the “.phz” file onto a USB. Use the USB to upload the file to the 3D printer. This process may take printer software up to ten minutes to complete.
12) While the model file is loading onto the 3D printer, ensure that the build plate and resin vat are totally clear of debris and residual resin from prior print jobs before installing them on the 3D printer appropriately.
13) Pour the liquid resin being calibrated into the resin vat. Do not fill the vat more than halfway. Because the build plate and 3D print will ultimately be submerged in the liquid resin, the liquid level will rise in the vat substantially.
14) After the build plate and resin vat have been secured in the 3D printer and after the model has been loaded successfully, select the checkmark on the interface of the 3D printer to start the printing process.
15) The printer will indicate when the model has been printed by returning the build plate to its default position at the top of the Z-axis and offering a “Print Complete”

message on the printer interface. When this occurs, the build plate (with the model adhered to it) can be removed from the printer.

16) Use a metal scraper to remove the 3D print from the build plate. The longer the exposure time, the more difficult the print will be to remove. This is why it is recommended to start at lower exposure times for calibration.

17) After it has been removed from the build plate, wash the 3D print with isopropyl alcohol. After residual liquid resin has been removed, set the print on a paper towel to dry.

18) While the 3D print is drying, the build plate, resin vat, and LCD screen should all be thoroughly cleaned with isopropyl alcohol. Remaining resin can be returned to its original container as long as it is poured through a strainer to remove any potential foreign objects. Skipping this step poses significant risk to the printer. It is very common for hardened resin pieces to break off from 3D prints as they are in the process of being printed. If these small pieces are not removed from the resin vat prior to printing another model, the FEP sheet and LCD screen will both be damaged.

19) After the 3D print has dried, the model can be assessed to determine if exposure time needs to be adjusted. If the print is indicating signatures of overexposure, the process above should be repeated, this time adjusting the “Exposure Time” to 0.5 seconds less than the previous iteration of calibration. If the print is illustrating signatures of underexposure, the process above should be repeated, this time adjusting “Exposure Time” to 0.5 seconds more than the previous iteration of calibration.

20) This process should be repeated until a 3D model is produced that demonstrates it was printed with the appropriate exposure time for a given machine and resin.

PPE required for this procedure includes gloves, eye protection, and a lab coat. While resin is non-hazardous and non-toxic when used as directed, care should be exercised in keeping it off of skin and out of eyes as it can cause minor irritation.

For this particular study, AnyCubic Colored UV Resin (Grey) was calibrated for subsequent 3D model printing. To adequately calibrate the exposure time for a given printer, resin, and model, there are a variety of calibration models that exist to test varied exposure times without sacrificing a great deal of time and material or leaving the machine susceptible to damage (Tatman et al. 2022). The calibration model most commonly used for the Phrozen Transform Fast is displayed in **Figure 22**.

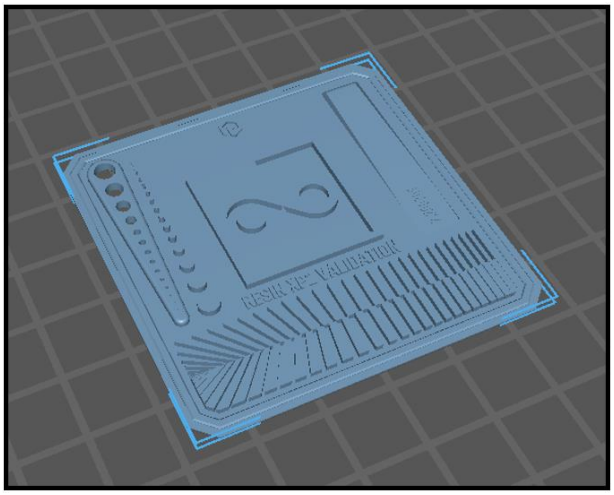

Figure 22: Resin XP2 Validation Matrix for Exposure Time Calibration

As mentioned in the calibration procedure previously outlined, the resulting character of the 3D-printed validation matrix indicates whether the model has been overexposed, underexposed, or exposed for an appropriate amount of time. An example of

this iterative processes is displayed in **Figure 23**. Each of the features on the 3D model shown in **Figure 23** is a tool to make observations regarding over or underexposure of the 3D print.

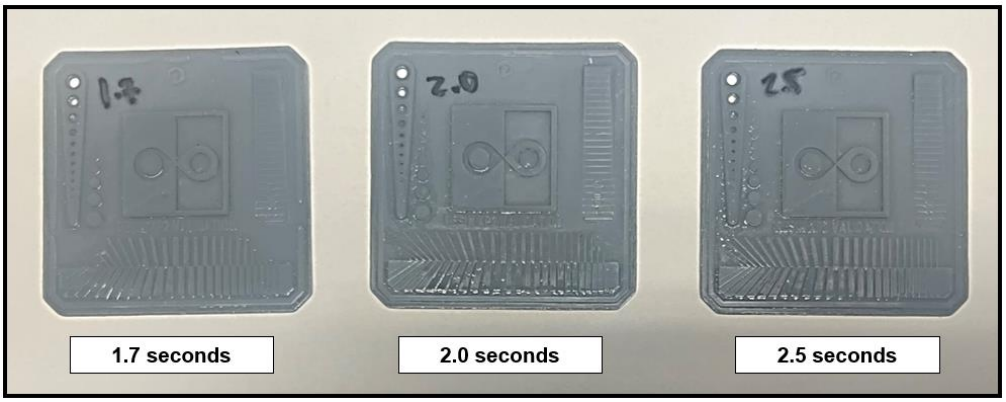

Figure 23: Impact of Exposure Time on Validation Matrix Model Character

The first feature to consider is the stack of rectangles at the bottom of the 3D model. When the print is overexposed to light, the rectangles will swell and begin merging together. When the print is underexposed to light, the thinnest rectangles will be wispy and easily rubbed off with a soft touch. When the top and bottom rectangles are observed to align perfectly with one another, the exposure time is considered correct. Additionally, the pins and holes on the left side of the model are a feature that can be used to determine appropriate exposure time. When exposed to light for the perfect amount of time, the number of pins and holes on the matrix are the same. When the quantity of pins outnumber the holes, the model was likely overcured. When there are more holes than there are pins, the model was likely undercured.

In the calibration case presented in **Figure 23**, an exposure time of two seconds appears to be the most appropriate for this application. The calibration matrix on the left

appears to be underexposed given that the rectangles on the bottom flanks have fallen off and the number of holes is far larger than the number of pins. The calibration matrix on the right is showing subtle signs of overexposure given that the rectangles at the bottom of the print are starting to merge together.

2.2.4.3 Slicing the 3D Model

The final step prior to actually 3D printing the model that has been prepared thus far is to "slice" the model. This is the term that 3D printing hobbyists and academics use to describe the process by which a file comprised of instructions to appropriately print the 3D model is prepared and generated. This file contains two important pieces of information for the 3D printer: (1) images representing each cross section of the model, and (2) instructions that dictate printer settings including exposure time, lift speed, positioning information, and more.

ChiTuBox—which was also used to appropriately orient, support, and hollow the conductivity sample 3D models—is the 3D printing pre-processing software used to prepare these images and instructions for the 3D printer. After appropriately positioning the model or models to be printed, the ChiTuBox "Slice Settings" feature allows for printer and resin settings to be adjusted prior to export.

Machine settings for the Phrozen Transform Fast are illustrated in **Figure 24** and should never change when using this machine. On the other hand, print slice configuration settings dictate the aforementioned set of instructions sent to the printer. These settings can and should be adjusted for different resin profiles and for different model shapes and sizes.

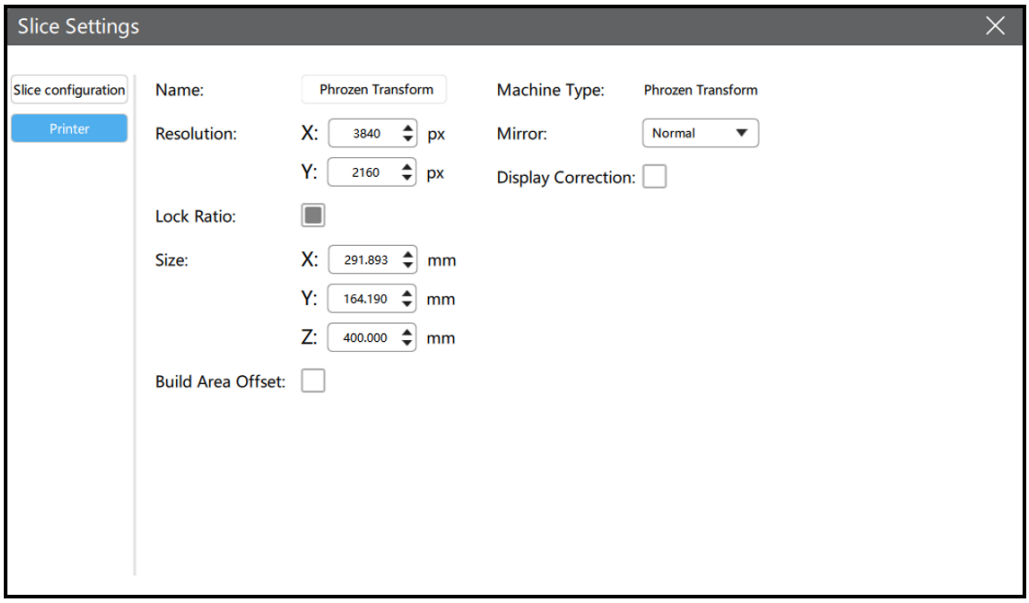

Figure 24: Phrozen Transform Fast 3D Printer ChiTuBox Settings

When printing a 3D model in the shape and size of a 7-inch long, 2-inch wide conductivity sample, most of the settings listed in the print slice configuration settings menu can be left as their default values. In reality, most of these settings need not be adjusted unless an exceptionally large or exceptionally heavy 3D model is being printed. For other, less complex applications, including the scenario described in this section, "Layer Height", "Bottom Layer Count", "Light-Off Delay", "Bottom Light-Off Delay", "Bottom Lift Distance", "Lifting Distance", "Bottom Retract Distance", "Retract Distance", "Bottom Lift Speed", "Lifting Speed", "Bottom Retract Speed", and "Retract Speed" do not need to be adjusted.

Exposure time was discussed in the previous subsection. "Bottom Exposure Time" refers to the exposure time applied only to the bottom-most layers of the model. This distinction allows the user to set longer exposure times for only the layers closest to where the model adheres to the build plate. Generally, appropriate values for this exposure range

between five to ten times longer than the exposure time for the rest of the model. For this application, “Bottom Layer Count” should be left near its default value of 20 layers. If the 3D print is having difficulty adhering to the build plate for the duration of the print, “Bottom Exposure Time” and “Bottom Layer Count” are among the first parameters that should be adjusted. Increasing both of these settings from their default values will yield a stronger foundation for subsequent layers of the model without forfeiting print resolution to overexposure on the model itself.

Very rarely do lifting or retracting speeds need to be adjusted. That being said, if the 3D print is heavy enough that rapid lifting speeds strain the connection between the print and the build plate, these settings may need to be amended to slower speeds. This adjustment will increase print time drastically and should only be used as a last resort.

Ultimately, the printer settings used to generate conductivity sample 3D prints with AnyCubic Colored Resin (Grey) are outlined in **Figure 25**.

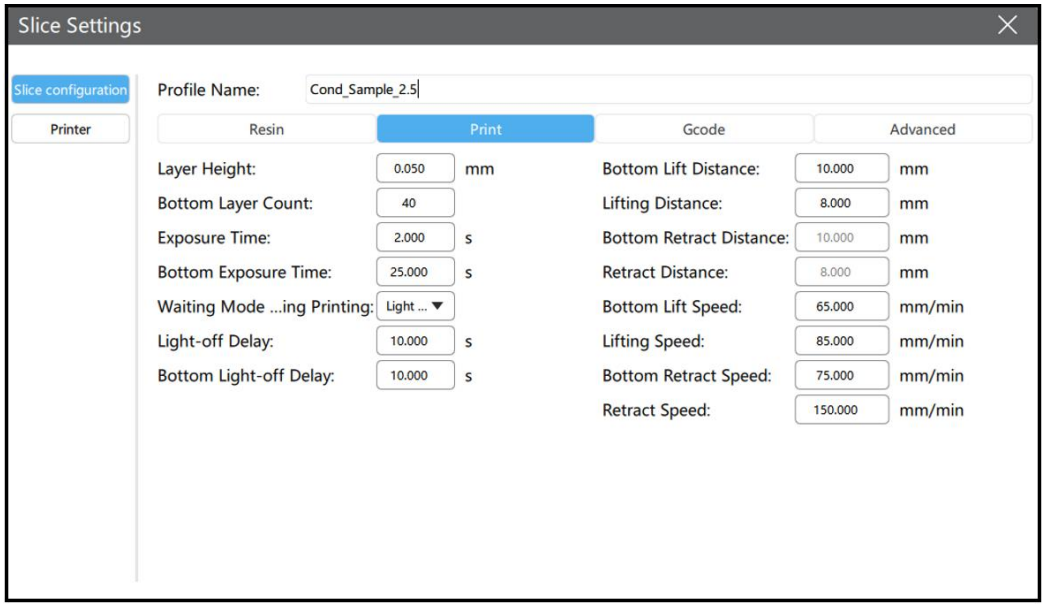

Figure 25: Conductivity Sample + AnyCubic Colored Resin Printer Settings

With the appropriate printer settings input and with the 3D model positioned appropriately on the build plate, the model (or models) can be sliced. Again, the output of this procedure will consist of both images representing every cross-section of the model and instructions that dictate printer settings including exposure time, layer height, and lift speed. An example of one of the images sent as instruction to the 3D printer after slicing is illustrated in **Figure 26**.

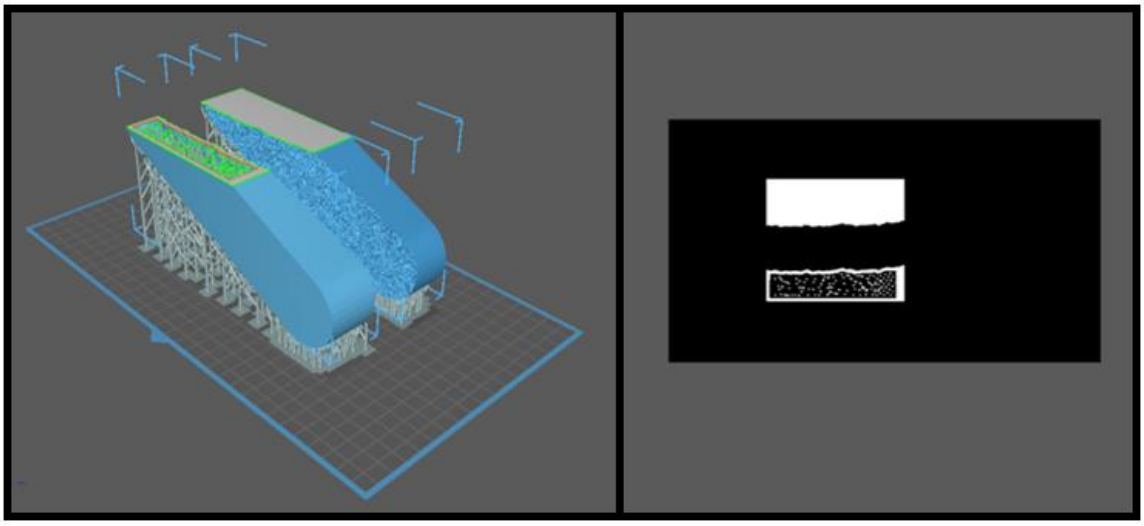

Figure 26: Example "Slice" of Conductivity Sample 3D Model

After the build plate has been leveled, exposure time has been calibrated, and the 3D model has been sliced with the appropriate printer settings, the model can be printed. This procedure is summarized as follows:

1) Select the model to be printed in ChiTuBox. Select the appropriate resin profile to communicate exposure and lift instructions to the printer.
2) "Slice" the model by selecting "Single Parameter Slice" in ChiTuBox.
3) Save the sliced model and model instructions by selecting "Save" in ChiTuBox. Save the resulting ".zip" file to the computer.

4) Duplicate the ".zip" file. In the duplicated file, change the ".zip" distinction to ".phz".
5) Load the ".phz" file onto a USB. Use the USB to upload the file to the 3D printer.
6) While the model file is loading onto the 3D printer, ensure that the build plate and resin vat are totally clear of debris and residual resin from prior print jobs before installing them on the 3D printer.
7) Pour the liquid resin previously calibrated for exposure time into the resin vat.
8) After the build plate and resin vat have been secured in the 3D printer and after the model has been loaded successfully, select the checkmark on the interface of the 3D printer to commence the printing process.
9) After the print is finished, remove the build plate (with the model adhered to it) from the printer.
10) Use a metal scraper to remove the 3D print from the build plate.
11) Remove and discard remaining supports from the 3D print by hand.
12) Wash the 3D print with isopropyl alcohol. Set the print on a paper towel to dry.
13) While the 3D print is drying, the build plate, resin vat, and LCD screen should all be thoroughly cleaned with isopropyl alcohol.
14) If the print is unsuccessful, adjust print slice configuration settings and repeat the process until success is achieved.

In summary, it is critical to calibrate the Z-axis any time the 3D printer is moved or when models are consistently having difficulty adhering to the build platform. Calibrating exposure time, as discussed above, is imperative in preserving model detail any time there is a change in model shape or size, resin, machine, or outside environment. Properly

preparing 3D models by orienting, supporting, and positioning them correctly on the build plate will ensure that the 3D model is given the greatest opportunity to be printed successfully on the first attempt. Adjusting printer settings such as exposure time, lift speed, and retract speed prior to slicing the model will ensure that model resolution is maintained and the machine is protected from damage due to model over or underexposure.

2.2.5 Post-Processing 3D Print

After the 3D print is removed from the build plate, it is important to wash the model with isopropyl alcohol to ensure all residual resin is removed. Following this, the print should be thoroughly dried and cured under UV light for approximately 30 minutes. If the print is not totally dry prior to additional exposure to UV light, a white powder-like substance will solidify on the surface of the print. This is undesirable as it makes additional steps of the workflow more difficult to complete. The resulting conductivity sample 3D print is displayed in **Figure 27** below.

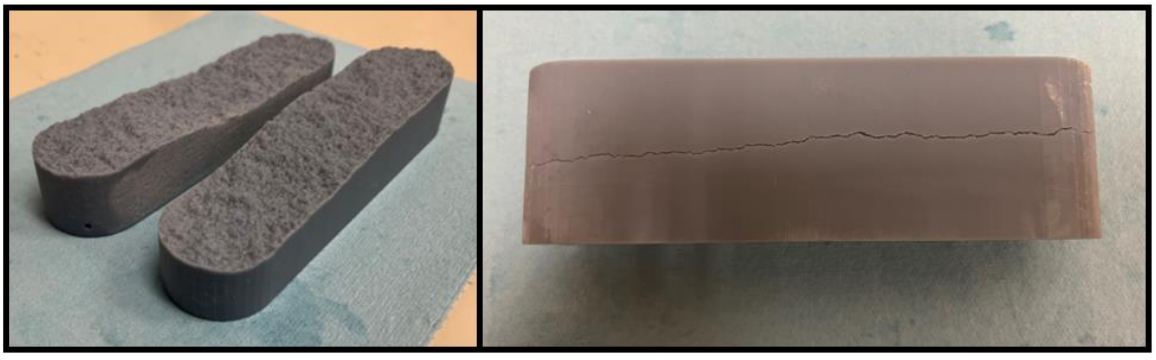

Figure 27: Printed Sample Fracture with Roughness (Reprinted from Sistrunk et al. 2023)

Observe that the two respective fracture faces align perfectly with one another in an attempt to mimic subsurface fracture behavior.

2.2.6 Creating Sample Mold

Because the 3D print output from the workflow thus far is not made of material strong enough to support the closure stress typically carried in conductivity experiments, it was critical to transfer the high-resolution surface roughness characterizing the 3D print to another material better suited for conductivity experimentation with appropriate mechanical properties.

In doing so, liquid silicone rubber was used to create a casting of both halves of the 3D-printed conductivity sample. For this, both halves of the printed samples were secured, with their surfaces facing upward, on a flat surface in a wood enclosure. The silicone liquid was then poured in the enclosure until both fracture faces were entirely submerged. It is important in this step not to pour the liquid directly onto the fracture faces, but rather into the void space surrounding them. After the silicone cured into a hardened rubber mold, the casting was removed from the 3D prints and set aside for future use. This process is demonstrated in **Figure 28**.

Figure 28: Conductivity Cell Fracture Sample Casting (Reprinted from Sistrunk et al. 2023)

2.2.7 Producing Cement Samples

In efforts to find an adequate proxy for unconventional reservoir rock to replace the plastic 3D prints output to this point, there were several non-negotiable criteria required from a material standpoint. First, the material was required to have similar properties to unconventional reservoir rock from an intrinsic rock properties standpoint so that conductivity results were relatively comparable to experimental data from previous conductivity studies. Second, the material was required to adequately preserve granular detail so far maintained with high resolution models and 3D prints.

High-strength cement was proposed as having the necessary intrinsic material properties to be an adequate unconventional reservoir rock proxy. Jansen et al. (2015) made significant contributions to the fracture conductivity knowledge base by establishing relationships between intrinsic rock properties and conductivity. Through their experimental study, Jansen et al. (2015) found that conductivity lost to additional closure stress in un-propped fractures was reduced with a greater Young's modulus. The authors also discovered that a greater Young's modulus yielded less reduction in conductivity due to proppant embedment in higher closure stress scenarios (Jansen et al. 2015).

Given the importance of Young's modulus, Poisson's ratio, and compressive strength outlined in prior study publications (Zhang et al. 2013; Jansen et al. 2015), a series of triaxial compression tests were run to vet the ability of this high-strength cement to mimic the intrinsic rock properties associated with unconventional reservoir rock and crucial in informing conductivity. Three triaxial compression tests were conducted on

cylindrical cement samples. The resulting stress-strain curves and radial strain-axial strain curves are displayed in **Figure 29A** and **Figure 29B**, respectively.

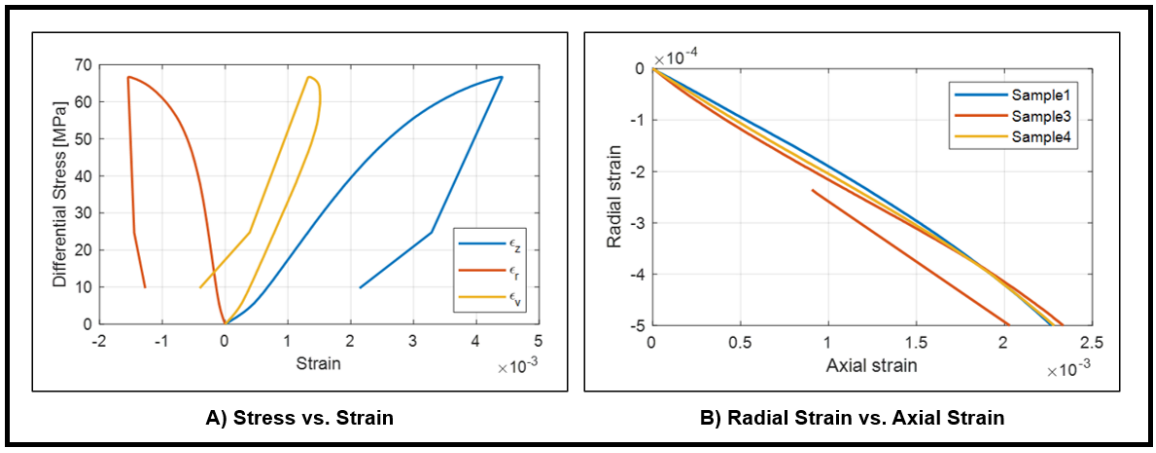

Figure 29: Cement Triaxial Compression Tests (Reprinted from Sistrunk et al. 2023)

The relationships in both **Figure 29A** and **Figure 29B** are in line with what would be expected from unconventional reservoir rock in practice. **Figure 29B** illustrates a linear relationship between axial and radial strain with a consistent slope across all three tests.

Young's modulus and Poisson's ratio were determined to be 3.25 Mpsi and 0.19, respectively. The compressive strength of the cement was determined to be 62 MPa, or just under 9,000 psi. These values are, again, in line with intrinsic unconventional reservoir rock properties.

For comparison, in their efforts to understand how intrinsic rock properties impacted fracture conductivity in the Marcellus Shale, Pena et al. (2016) summarized eighteen separate triaxial compression tests conducted on a series of outcrop cores with different orientations relative to bedding. The Young's modulus associated with each of

these samples ranged from 1.07 Mpsi to 4.44 Mpsi. Poisson's ratio ranged from 0.20 to 0.31 across cores. Compressive strength ranged from roughly 9,000 psi to 14,000 psi.

Prior to this study, Jansen et al. (2015) also looked into the effects of rock mechanical properties on fracture conductivity. Samples for this study were taken from both the Fayetteville Shale and Eagle Ford Shale. In their evaluation of the Fayetteville Shale, Jansen et al. (2015) summarized triaxial compression tests conducted on five Fayetteville cores taken from two separate vertical zones of an outcrop. The Young's modulus associated with each of these samples ranged from 0.46 Mpsi to 1.26 Mpsi and Poisson's ratio ranged from 0.13 to 0.19. In their evaluation of the Eagle Ford Shale, Jansen et al. (2015) summarized thirteen triaxial compression tests conducted on Eagle Ford cores taken from different lateral locations from a South Texas outcrop. The Young's modulus associated with each of these samples ranged from 2.02 Mpsi to 2.71 Mpsi. Poisson's ratio ranged from 0.19 to 0.23. It is worth noting that these measurements were taken from samples with 2 MPa confining stress applied to them during triaxial compression testing to hold fragile cores together and prevent damage to instrumentation in a rock burst event. While this should not result in major material impact, the addition of confining stress likely subtly increases the measured Young's modulus and decreases measured Poisson's ratio of each sample (Jansen et al. 2015).

Even with this taken into consideration, studies summarized in this section illustrate that intrinsic rock property measurements associated with cement are reasonable relative to previous Marcellus, Fayetteville, and Eagle Ford measurements.

In addition to confirming that the high-strength cement proposed as an adequate proxy for unconventional reservoir rock was appropriate from a rock characteristic standpoint, it was a priority to find a material that preserved the resolution of the workflow up until this point. **Figure 30** illustrates that—at least from a visual standpoint—acceptable granularity was maintained from 3D model to 3D print to cement sample.

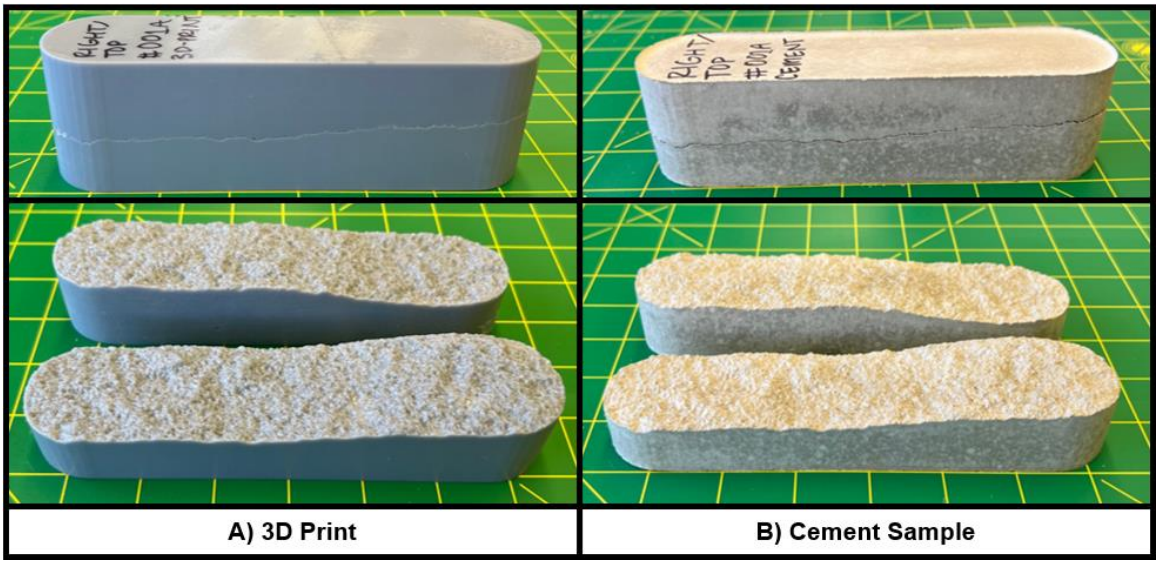

Figure 30: Cement Sample Qualitative Comparison (Reprinted from Sistrunk et al. 2023)

Because detail on the order of microns can impact the fracture conductivity of a given fracture surface, it was important to quantitatively assess the granularity of the detail captured from the 3D print into the cement sample replica. For this, a profilometer was used to characterize the respective surface height distributions of both halves of the 3D print and cement sample. This analysis is displayed in **Figure 31** on the next page.

The profilometer data associated with the cement replica was then transformed into a cumulative distribution function for comparison to the surface height distribution assigned to the 3D model. This is illustrated in **Figure 32**.

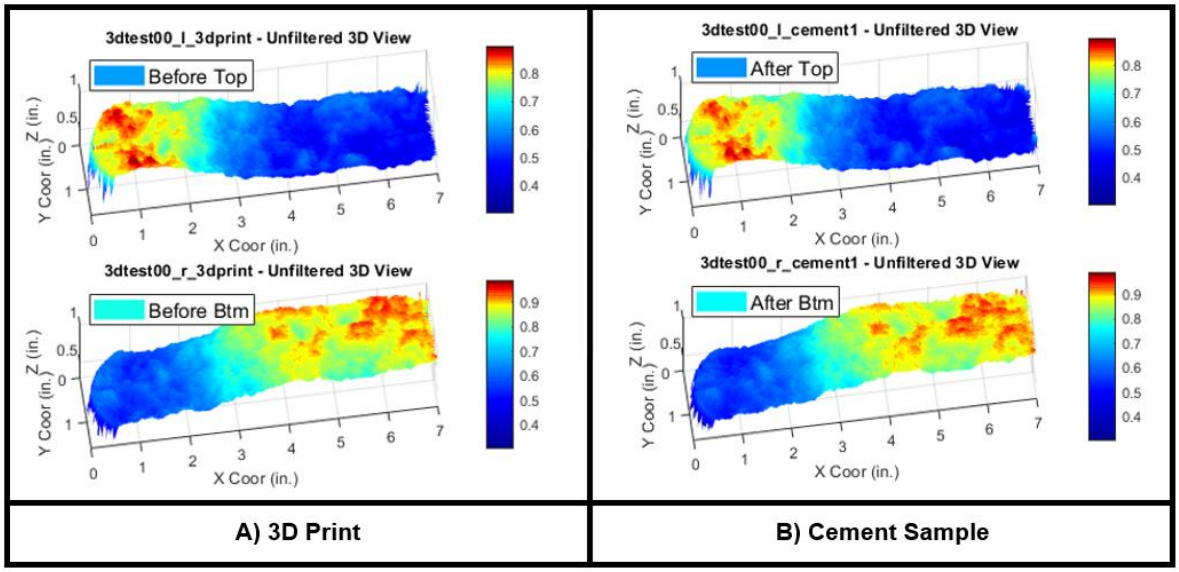

Figure 31: Cement Sample Quantitative Comparison (Reprinted from Sistrunk et al. 2023)

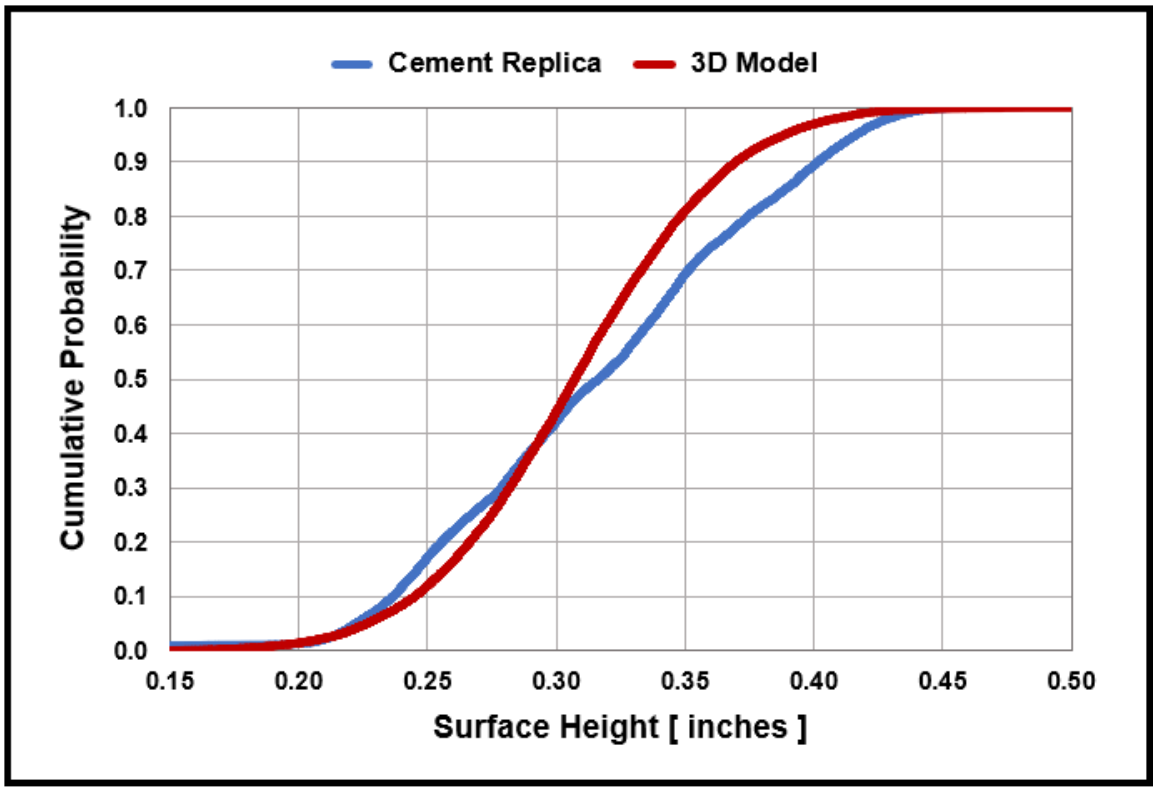

Figure 32: Cumulative Distribution Function— Cement/Model Surface Distribution

As is illustrated in **Figure 31** and **Figure 32**, comparing the surface distributions of the 3D print and cement sample replica quantitatively also demonstrated sufficient resolution carried across the workflow.

The high-strength cement evaluated in this subsection proved to be both intrinsically similar to unconventional reservoir rock and successful at preserving surface roughness detail maintained in previous segments of the workflow. Because this high-strength cement satisfied both of the criteria outlined above, it was carried forward through this study as an acceptable proxy for unconventional reservoir rock.

2.2.8 Executing Fracture Conductivity Experiments

After producing several identical high-strength cement samples, all with the same rough surface, it was time to attempt a conductivity experiment with the Modified-API Conductivity Workflow. Again, these experiments are aimed at determining the resistance to fluid flow through two matching fracture faces.

Quantitatively, the fracture conductivity is described in **Equation 2**, where C_f represents the fracture conductivity, k_f represents the permeability inside of the fracture, and w_f represents the width of the fracture.

$$C_f = k_f w_f \tag{2}$$

Because fracture permeability and fracture width are so difficult to determine separately in a laboratory setting, an experimental apparatus is leveraged to make flowrate and pressure measurements that allow experimentalists to circumvent this obstacle.

The experimental set-up is illustrated in **Figure 33**. In a single iteration of this experiment, the conductivity sample comprised of matching fracture faces is loaded into the modified-API conductivity cell represented by the stainless-steel rectangular prism centered under the load frame in **Figure 33**.

The inlet and outlet lines, in addition to three pressure gauges, are connected to fully assemble the apparatus. After applying a given closure stress with the load frame, nitrogen is introduced to the system to establish flow through the fracture. A series of valves and backpressure regulators ensure that the nitrogen flows from the nitrogen tank into the cell inlet line and through the fracture face before being expelled by the cell outlet line.

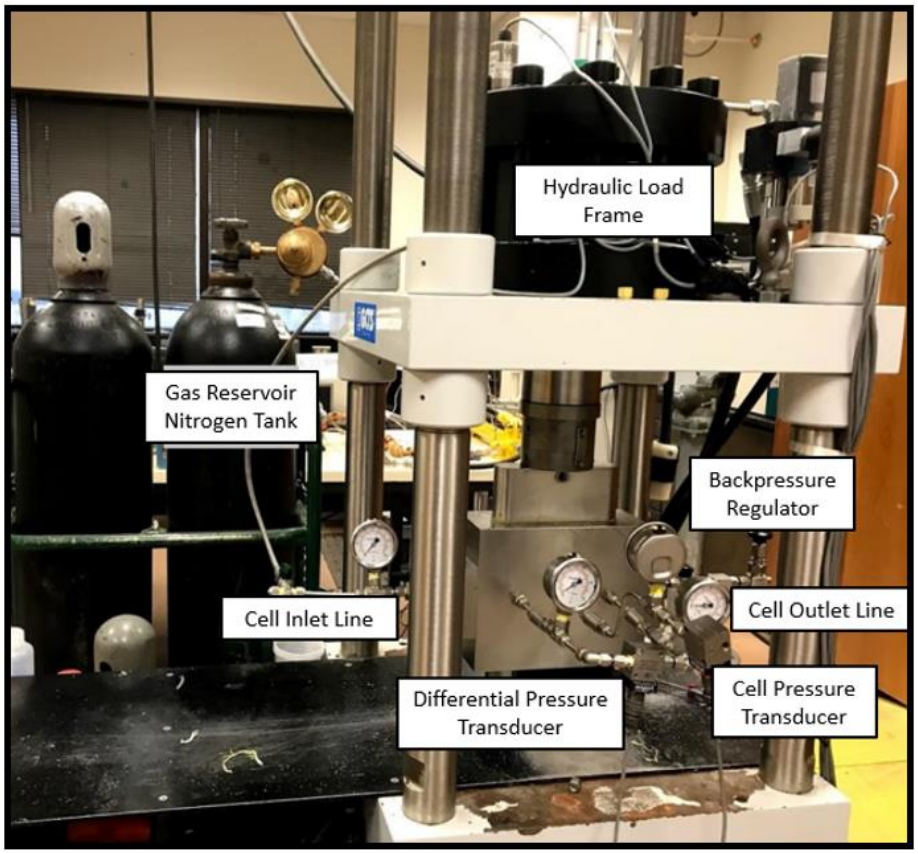

Figure 33: Modified-API Fracture Conductivity Test Apparatus (Guerra, 2021)

In executing a conductivity experiment successfully, it is critical to prepare the matching fracture face conductivity sample correctly. In this experimental procedure, great care is taken in preparing the sample to be loaded into the modified-API conductivity cell in order to properly isolate five openings from one another with an epoxy seal. Two of these openings—on either side of the short sample ends—are used as the inlet and outlet for the fluid flowing through the fracture, respectively. On the long side of the sample, the port in the middle (P_{Cell}) is used to determine the average pressure in the cell. The two openings on either side of this port (P_1 and P_2) are used to measure the differential pressure across the fracture. Following this preparation, the sample, pictured on the right of **Figure 34** below, is ready to be loaded into the modified-API conductivity cell.

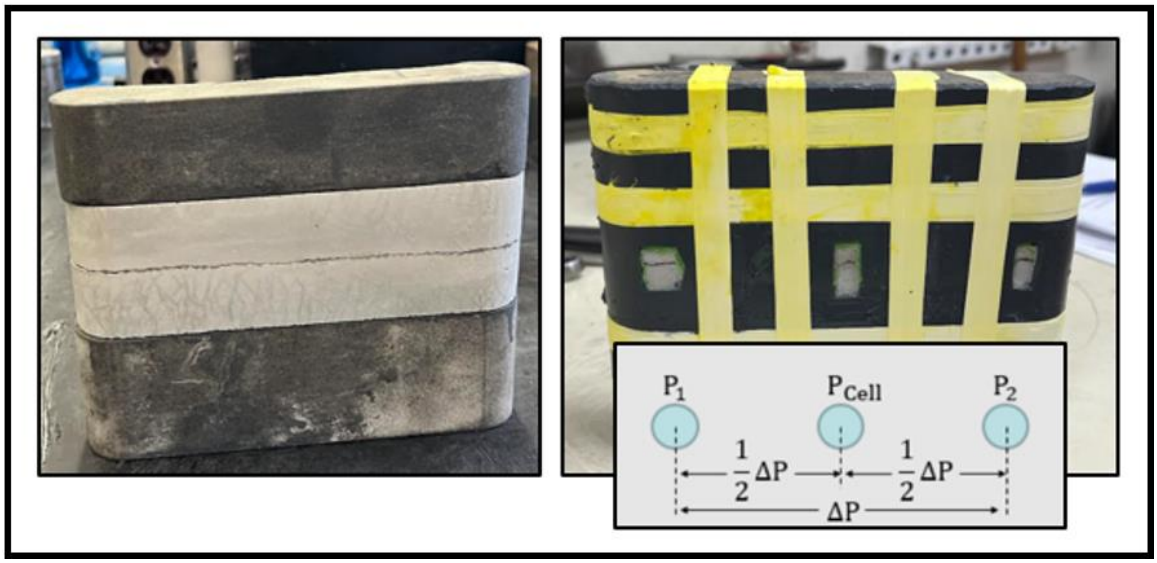

Figure 34: Conductivity Sample Preparation (Reprinted from Sistrunk et al. 2023)

After sample preparation and loading, nitrogen is introduced to the system by slowly opening the valve between the cell inlet line and the conductivity cell. This should be done as gradually as possible to ensure that proppant in the fracture is not redistributed with incoming flow. After the average pressure in the conductivity cell stabilizes, the valve

on the cell outlet line is slowly opened to allow flow through the system. This valve is gently opened further and further until the flowrate through the system reaches 1.0 L/min. The valve remains open in this position while flowrate and pressure through the system stabilize for a minimum of five minutes. Following this stabilization period, the flowrate, average pressure in the cell, and differential pressure across the fracture are recorded for forthcoming calculations.

Following the recording of these measurements, the valve on the cell outlet line is partially closed to reduce the flowrate by roughly 0.25 L/min. After the system stabilizes, the appropriate measurements are recorded. This process continues until four different data points (representing four different flowrates and their responding pressure environments) for a given closure stress scenario have been obtained. After this data has been collected, valves on both the cell inlet and cell outlet lines are closed. The closure stress is increased in increments of either 500 psi or 1,000 psi depending on the level of data granularity required for the experiment. The procedure described above is then replicated to obtain data for four different flowrates at an additional closure stress. This is repeated for as many closure stresses as desired until the maximum closure stress for a given rock sample is reached. The recorded flow rates, cell pressures, and differential pressures are then used to calculate the fracture conductivity at varied closure stresses through a given fracture surface.

The Darcy equation and Forchheimer equation (shown in **Equation 3** and **Equation 4,** respectively), in conjunction with the real gas law, are used to derive conductivity in the laboratory setting (Copeland, 2020). McGinley et al. (2015) concluded that the Darcy equation is valid in the laboratory setting for nitrogen flow rates less than

2.0 L/min. At flow rates exceeding this, the Forchheimer equation should be applied (McGinley et al. 2015; Winner, 2018).

$$-\frac{\Delta P}{\Delta L} = \frac{\mu v}{k_f} \tag{3}$$

$$-\frac{\Delta P}{\Delta L} = \frac{\mu v}{k_f} + \beta \rho_f v^2 \tag{4}$$

In **Equation 3** and **Equation 4** above, $\Delta P/\Delta L$ represents the change in pressure over a given length, μ represents fluid viscosity, v represents fluid velocity, k_f represents permeability in the fracture, ρ_f represents the density of the fluid, and β represents an inertial factor. With the equations summarized above, the real gas law, and simple material balance, **Equation 5** is derived.

$$\frac{(P_{cell} + 0.5\Delta P)^2 - (P_{cell} - 0.5\Delta P)^2}{2L} \frac{M_g}{zRT} = \frac{\mu q \rho_f}{h_f} \frac{1}{C_f} \tag{5}$$

Recall that P_{cell} represents the average pressure in the fracture, ΔP represents the pressure drop across the fracture, L represents the length of the sample, M_g represents the molecular weight of the gas, z represents the gas compressibility factor, R represents the universal gas constant, T represents the temperature of the fluid, μ represents the viscosity of the fluid, q represents the flowrate of the fluid through the fracture, ρ_f represents the density of the fluid, h_f represents the width of the sample, and C_f represents the fracture

conductivity associated with the sample. In **Equation 5**, the fracture conductivity represents the only remaining unknown.

To determine fracture conductivity, $\frac{(P_{cell}+0.5\Delta P)^2-(P_{cell}-0.5\Delta P)^2}{2L}\frac{M_g}{zRT}$ is plotted relative to $\frac{\mu q \rho_f}{h_f}$, where the inverse of the slope on the resulting plot is taken to be the fracture conductivity. This relationship is illustrated in **Figure 35** below.

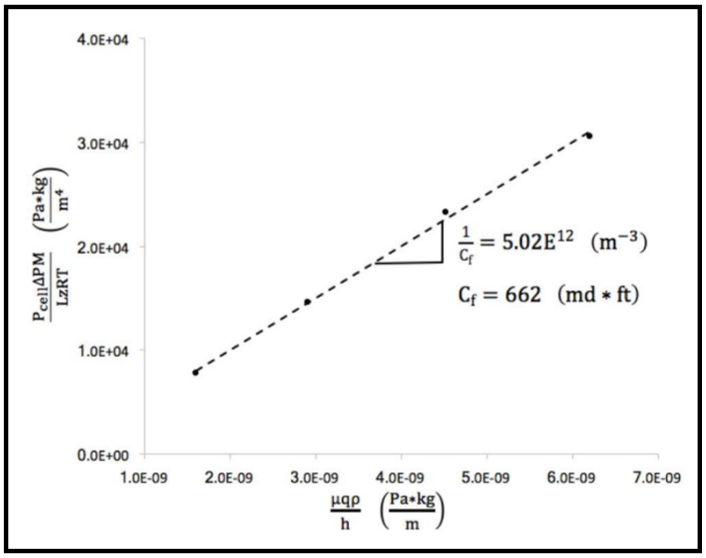

Figure 35: Fracture Conductivity Experimental Determination (Copeland, 2020)

For this particular experimental study, flow rates through the fracture face did not exceed 2 L/min, so the Forchheimer equation was not necessary to apply. More specifically, closure stress was ramped up from 500 psi to 3,000 psi in increments of 500 psi. At each of these six different closure stresses, flow rate was adjusted four times. The fracture conductivity at each closure stress was then calculated with the relationship depicted in **Figure 35**. **Figure 36**, at the top of the next page, illustrates an example of the data that is actually monitored and recorded throughout the duration of an experiment.

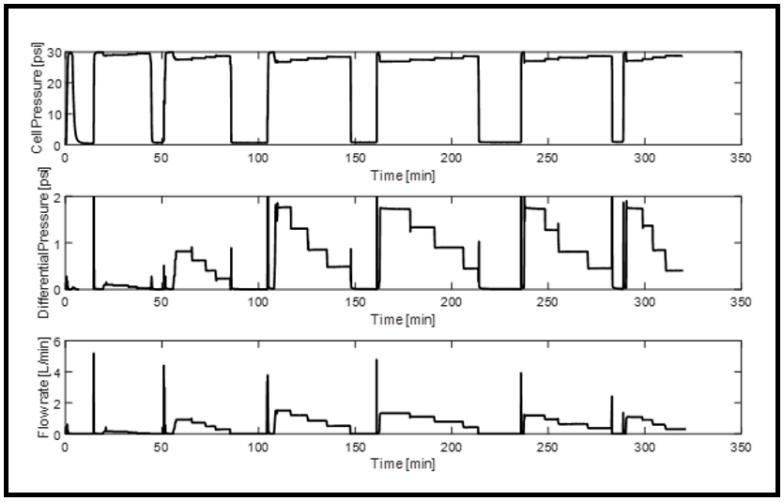

Figure 36: Conductivity Experimental Data (Reprinted from Sistrunk et al. 2023)

This data was used to determine the un-propped fracture conductivity of the cement sample pictured in **Figure 34** at a variety of closure stresses. The resulting fracture conductivity curve is illustrated in **Figure 37**. As expected, fracture conductivity values for this un-propped fracture sample decline steadily as the closure stress applied to the sample increases.

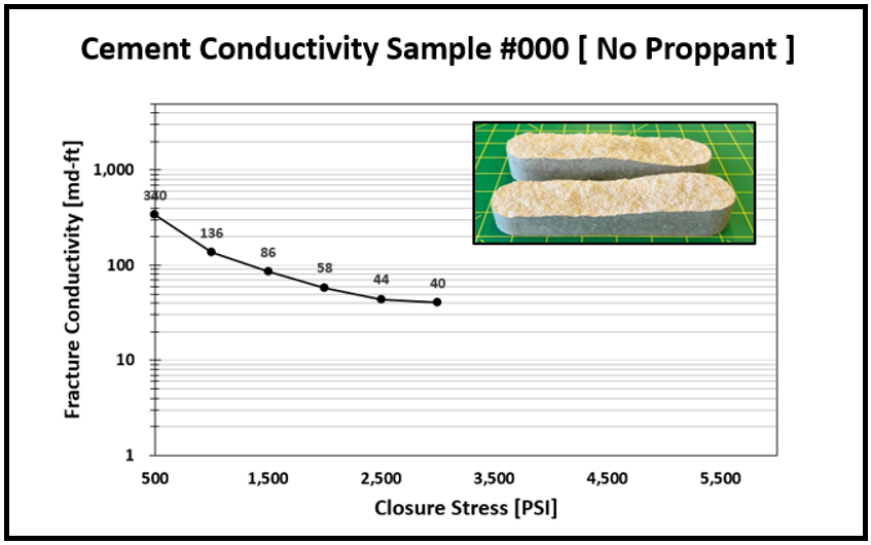

Figure 37: Un-propped Fracture Conductivity (Reprinted from Sistrunk et al. 2023)

2.2.9 Comparing Results to Previous Experiments

Although the fracture conductivity curve displayed in **Figure 37** appears to behave similarly to historic conductivity experimental data anecdotally, it was important to directly compare results before claiming the workflow outlined above was successful in establishing a proof-of-concept for future experiments. The direct comparison shown in **Figure 38** illustrates how the high-strength cement sample that has been an output of this workflow thus far compares to historical conductivity data from the Fayetteville Shale, Eagle Ford Shale, Mahantango Formation, and Barnett Shale. These domestic basins are distinguished from one another on the comparison figure below with different colors. Each curve represents an individual un-propped fracture conductivity experiment.

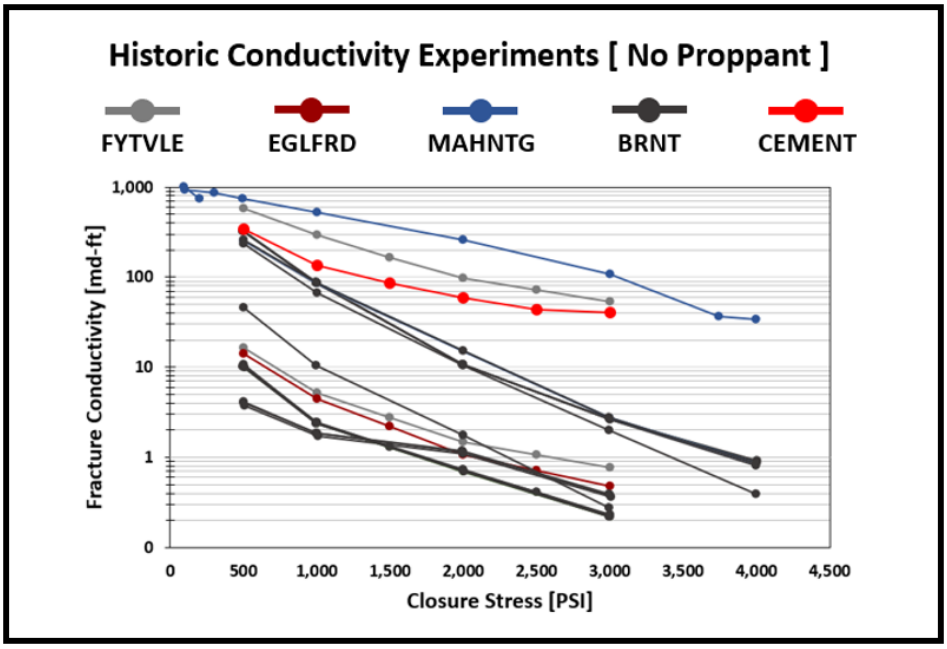

Figure 38: Historic Conductivity Sample Comparison (Reprinted from Sistrunk et al. 2023)

All of the fracture conductivity curves displayed on **Figure 38** were obtained with rough, un-propped rock samples from previously published experimental studies.

Fayetteville Shale conductivity data was originally published by Briggs et al. (2014). Samples were taken from a Fayetteville Shale outcrop and artificially fractured to preserve surface roughness for conductivity measurements. Eagle Ford conductivity data was originally published by Enriquez-Tenorio et al. (2019). Samples were taken from an Eagle Ford Shale outcrop over the entire vertical extent of a complete exposure of the Eagle Ford Shale in Antonio Creek and Lozier Canyon near Langtry, Texas and artificially fractured prior to experimentation. Mahantango conductivity experiments were conducted by Guerra (2021) with artificially induced fractures in outcrop rock samples. Finally, Barnett Shale conductivity data was originally published by Zhang et al. (2013) in a paper detailing their robust Barnett experimental program. These samples were taken from a Barnett Shale outcrop and fractures were artificially induced by breaking the shale rock along its laminated bedding planes.

Because all previous conductivity data displayed on **Figure 38** was obtained by experimentation on un-propped fracture conductivity samples with varied surface roughness, it was appropriate to use this data in an effort to determine whether or not the cement conductivity sample results were reasonable. In this case, the fracture conductivity associated with the un-propped cement sample was in range relative to previous experimental data, albeit it in the upper part of that range.

Because results aligned appropriately with previous un-propped conductivity samples, this high-strength cement was deemed an appropriate proxy for unconventional reservoir rock and the workflow detailed above was regarded as having successfully established proof-of-concept for subsequent experimentation.

2.3 Results & Discussion

After establishing proof-of-concept for the workflow outlined above successfully, it was time to commence the resulting experimental study.

2.3.1 Baseline Sample Design

As with any experimental study, it was important to start by establishing a strong baseline sample for future comparison. Because proppant characteristics are easily amended from experiment to experiment, establishing a baseline for the experimental study was limited to establishing a baseline surface topography.

Recall that the workflow established in previous sections required mean, standard deviation, correlation length in the X direction, and correlation length in the Y direction to simulate a rough fracture surface. It was crucial to the integrity of the experimental study that these parameters were not selected randomly, but rather informed appropriately to represent a reasonable formation rock roughness. For this, a variety of shale samples from previous experimental programs were scanned with a profilometer to obtain the height of the surface (represented by the Z coordinate) across a set of X and Y coordinates. This was done for a variety of samples across several domestic plays to obtain a general range for unconventional reservoir rock surface roughness associated with historical conductivity samples. This data was then used to determine an average roughness defined by mean, standard deviation, and correlation lengths in both the X and Y direction. A reasonable representation of a shale conductivity sample was subsequently defined by a standard deviation of 0.025 inches, a correlation length in the X direction of 1 inch, and a correlation length in the Y direction of 1 inch. A mean of 1.25 inches was assigned in order to give the

sample adequate height for experimentation. These parameters characterized the baseline surface topography moving forward.

These parameters were taken as inputs into Stanford University's geostatistical library, GSLIB. The output was the simulated rough surface displayed in **Figure 39**.

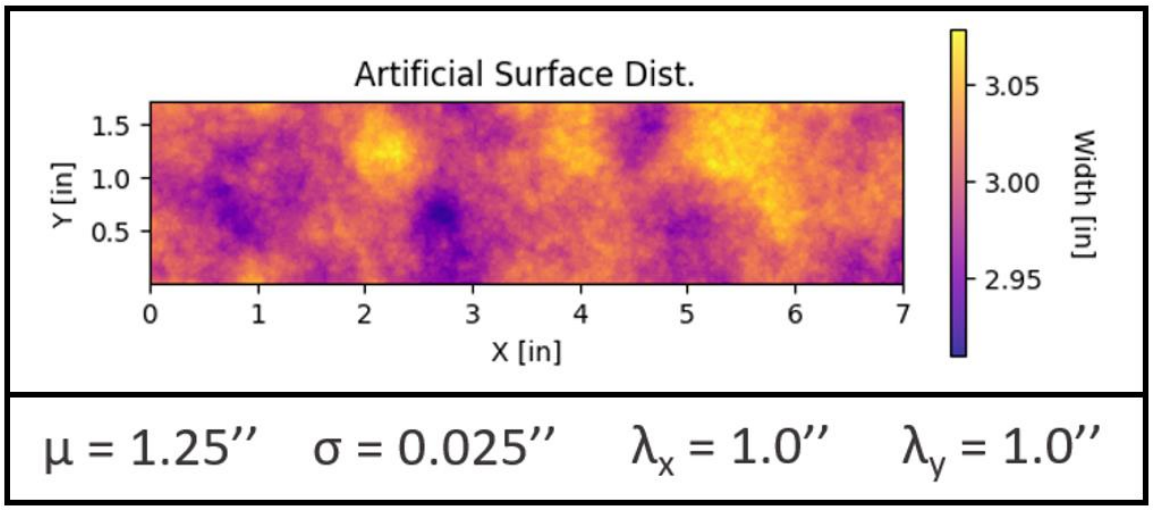

Figure 39: Geostatistically-Simulated Surface Roughness for Baseline Sample

The resulting set of coordinates was then used to generate a 3D mesh in the form of an ".stl" file, which represents the model as an amalgamation of small triangles that fully describe the appropriate surface geometry. The desired geometry of the 3D model was then cut from an existing fracture surface to fit the modified-API conductivity cell size requirements. The 3D model was then printed with a Phrozen Transform Fast Digital Light Processing (DLP) 3D Printer. The resulting 3D print was post-processed and used to make a silicone mold casting. Finally, the silicone mold was used to generate cement samples to be used in later experiments. The 3D model, 3D print, and resulting cement sample created from the simulated surface roughness shown in **Figure 39** are displayed in **Figure 40**. The

baseline cement samples produced for the experimental program—as defined above—are shown in **Figure 41**.

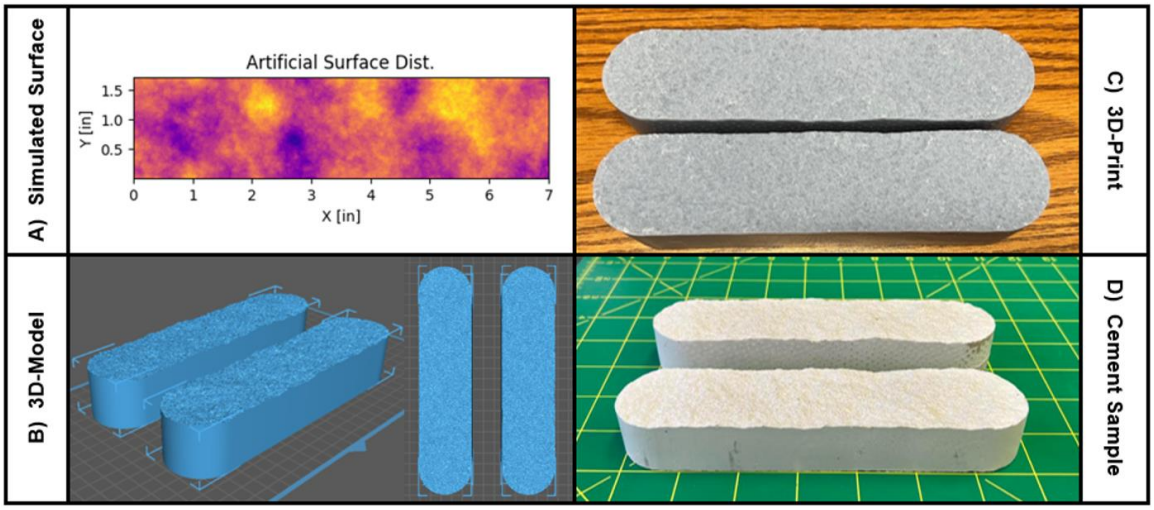

Figure 40: Generating Cement Baseline Samples with Simulated Surface Roughness

Figure 41: Baseline Cement Conductivity Sample for Experimental Program

2.3.2 Baseline Sample Experimentation

Cement samples were prepared for experiments as outlined in previous sections. Two identical sample sets were produced as inputs to compare the conductivity in both a propped and un-propped fracture scenario. In the case of the sample being prepared for a propped conductivity experiment, South Texas-mined 100-mesh sand from Webb County, Texas was distributed at 0.2 lb/ft^2 prior to sealing the sample with epoxy.

During both propped and un-propped experiments, closure stress was ramped up from a starting point of 1,000 psi to 4,000 psi in increments of 1,000 psi. At each closure stress, four different flow rates were recorded to comprehensively determine what the fracture conductivity associated with the sample for each closure stress was. The results are displayed in **Figure 42**.

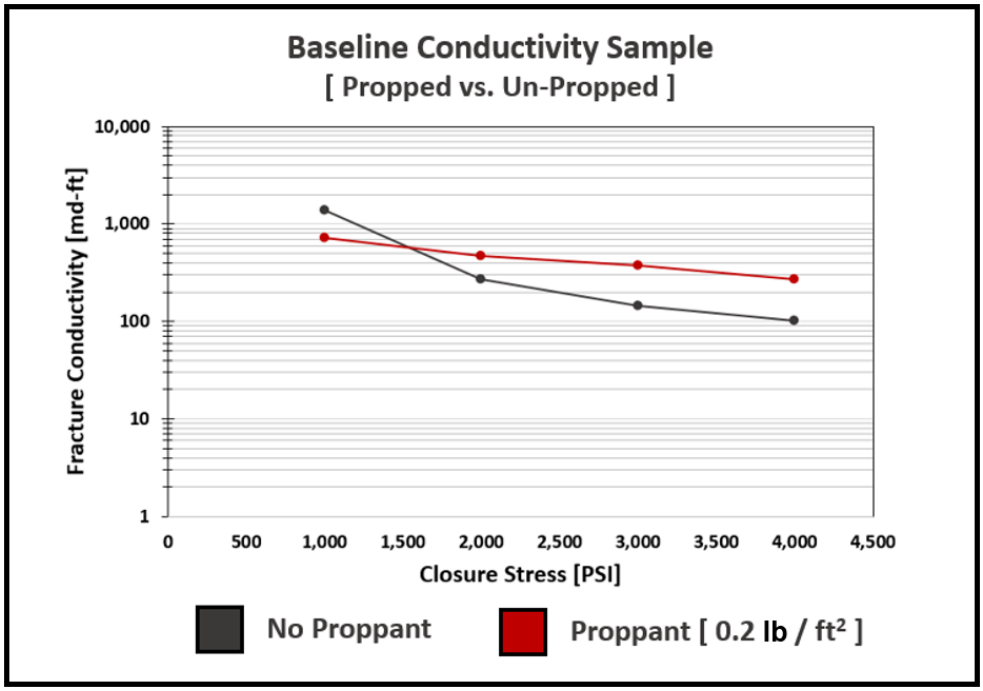

Figure 42: Baseline Sample Conductivity (Reprinted from Sistrunk et al. 2023)

The red curve displayed on **Figure 42** represents the rough fracture surface propped open with 0.2 lb/ft^2 of 100-mesh proppant. The black curve on the plot represents the exact same rough fracture surface without any proppant holding the fracture open. As expected, the propped sample is associated with higher conductivity at higher closure stresses due to proppant holding the fracture open as more and more closure stress is applied to the cement sample.

2.3.3 Demonstrating Repeatability

As mentioned in the introduction, the major objective of this study was to successfully establish a workflow to generate identical high-strength cement samples with geostatistically-informed rough fracture surfaces, in addition to exhibiting that this high-strength cement is an adequate proxy for unconventional reservoir rock in fracture conductivity experiments. The primary motivation for this objective was to reduce the uncertainty associated with experimental results in fracture conductivity workflows.

It was important to the validity of the experimental study to assess how well the established workflow satisfied this study motivation. If experimental results for a given surface topography, proppant size, proppant concentration, and proppant distribution are not consistent, the overall value of the workflow would be diminished.

To assess this, two identical cement sample sets characterized with the baseline surface topography described in the previous section were produced with the same silicone casting. Samples were prepared identically to one another. Each sample was loaded with 0.2 lb/ft^2 of 100-mesh proppant from South Texas.

Conductivity experiments were run on both samples. The results are illustrated in **Figure 43**. The red curve and green curve displayed on the plot represent the exact same experimental conditions from surface topography to proppant characteristics.

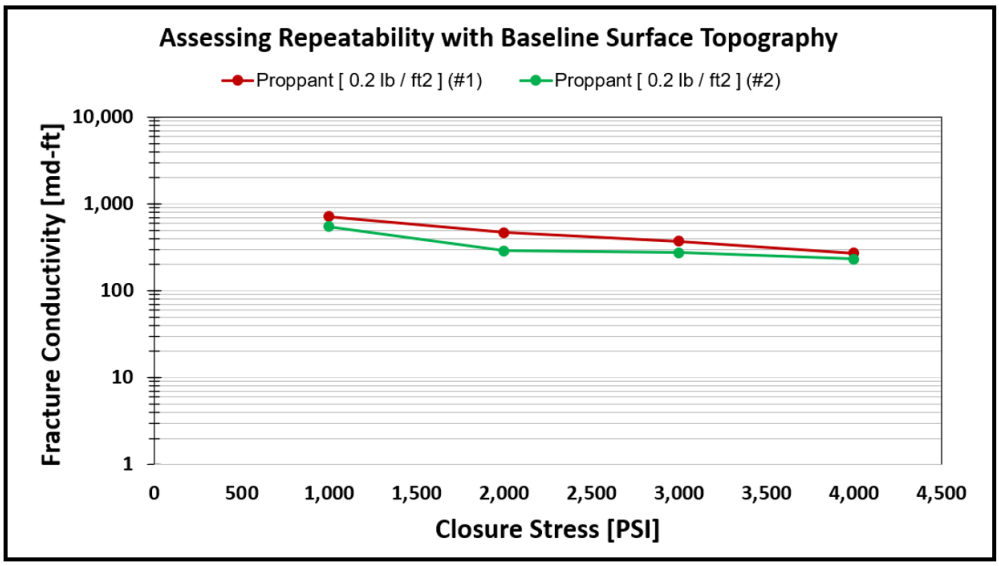

Figure 43: Assessing Experimental Repeatability with Baseline Surface Topography

Observe that the experimental results for both tests align closely, especially at the lowest and highest closure stresses applied to the sample. Slight deviation in results can likely be attributed to manually loading proppant into the samples, which requires a great deal of precision and consistency.

2.4 Conclusions

This chapter comprehensively summarizes a workflow created to generate identical high-strength cement samples with geostatistically-informed rough fracture surfaces, while also illustrating that this high-strength cement is an adequate proxy for unconventional reservoir rock in fracture conductivity experiments.

After successfully establishing and vetting proof-of-concept for this workflow with published conductivity experimental data, a baseline surface topography was established to anchor the forthcoming experimental program. The baseline was then benchmarked in both propped and un-propped fracture scenarios. Finally, experimental repeatability was verified by conducting identical experiments back-to-back and comparing results.

The technical work presented in this section successfully demonstrated the following:

1) A robust workflow was successfully developed to generate identical high-strength cement samples with different geostatistically defined surface topographies through the use of 3D printing.
2) The high-strength cement used in this study has both sufficient intrinsic mechanical properties and adequately captures granular detail carried through the 3D printing process.
3) Cement sample fracture conductivity experimental results are in a reasonable range relative to historic experimentation, although conductivity associated with cement samples is generally in the upper quartile of the established range.
4) Un-propped and propped experiments on the same baseline surface topography yielded results in line with convention.
5) Repeatability of experiments was established by running identical experiments back-to-back and garnering similar results.

3. PROPPANT TRANSPORT

3.1 Introduction

The primary objective of the study presented in this chapter was to incorporate another layer of subsurface complexity to proppant transport experiments by creating a fracture network characterized by rough-wall fracture surfaces.

Similar to the fracture conductivity stimulation workflow discussed in the previous chapter, fracture surface topography is instrumental in informing results of proppant transport experimental workflows. Because of this, it is important to take great care in establishing and vetting a method to inform rough fracture surfaces with geostatistical parameters, ensuring that no resolution is lost in the 3D printing process.

This chapter summarizes the workflow created to generate fracture networks with geostatistically-informed rough surfaces, while highlighting difficulties with the 3D printing process unique to this application.

In short, a rough fracture surface is first simulated with a series of geostatistical parameters serving as inputs to a geostatistical library. The simulated rough fracture surface is then scaled to the appropriate size for proppant transport experiments and printed with a Digital Light Processing (DLP) 3D printer. Following this, the fracture network is assembled and deployed for experimentation.

Tatman et al. (2022) spearheaded efforts to simulate and print a rough-wall fracture network that serves as the baseline for the greater experimental program (Tatman et al. 2022). Tatman's work is germane to the generation and analysis of the fracture network

described in this study and will be referred to throughout this section as the “first iteration” of proppant transport plates. The fracture network produced as a result of the study summarized in this chapter is referred to as the “second iteration” of proppant transport plates.

3.2 Methodology

Again, the primary objective of the study presented in this chapter was to create a workflow to generate a rough-wall fracture network, introducing another layer of subsurface complexity to proppant transport experimentation. The procedure employed is outlined as follows:

1) Simulate Rough Fracture Surface
2) Generate 3D Model for 3D Printer
3) Prepare 3D Model for 3D Printer
4) Print 3D Model
5) Post-Process 3D Print
6) Assemble Fracture Network
7) Execute Proppant Transport Experiments

Each subsection in this chapter describes the steps to the procedure outlined above in detail.

3.2.1 Simulating Rough Fracture Surface

The first few steps of the methodology outlined above do not deviate significantly from their counterparts in the fracture conductivity experimental workflow presented in the second chapter of this thesis. A geostatistical library—GSLIB—is again used to simulate

a rough fracture surface given a mean, standard deviation, and correlation lengths in both the X and Y directions.

The first iteration of the fracture network produced for proppant transport experiments by Tatman et al. (2022) was characterized by a mean of 0.3 inches, a standard deviation of 0.025 inches, a correlation length in the X direction of 1 inch, and a correlation length in the Y direction of 1 inch. This characterization was applied to a 48-inch long and 24-inch wide surface representing the dimensions required for the main fracture and a 12-inch long and 24-inch wide surface representing the dimensions required for a secondary fracture in the proppant transport apparatus. This experimental apparatus will be discussed in further detail in the following subsections.

The baseline surface simulation differs from the second set of surfaces simulated for proppant transport experiments through varied correlation length in the X direction. While mean, standard deviation, correlation length in the Y direction, and surface size remain constant, correlation length in the X direction is amended from 1 inch to 3 inches. A 6-inch by 6-inch comparison of the two simulated surfaces is displayed in **Figure 44**.

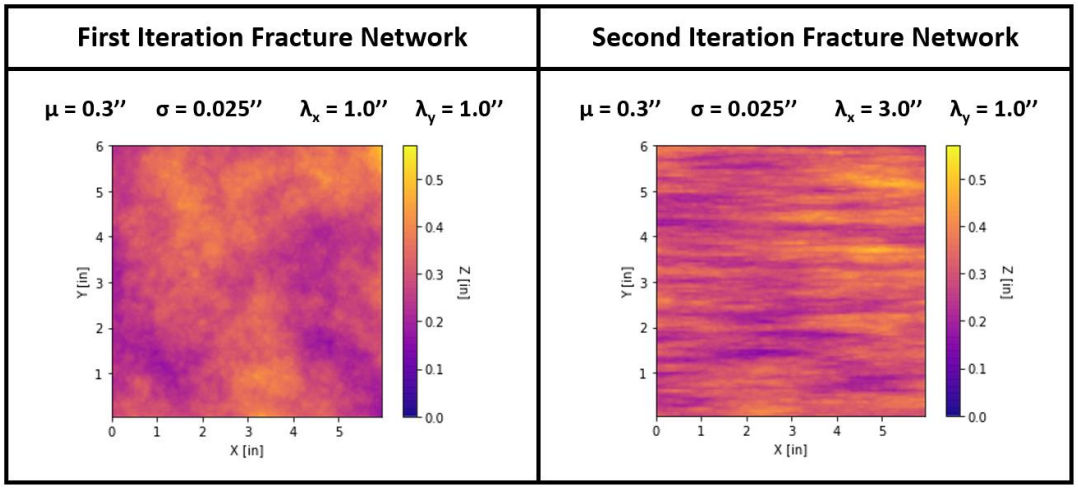

Figure 44: Comparison of Fracture Networks Generated for Proppant Transport

3.2.2 Generating 3D Model for 3D Printer

Recall from the previous chapter that the simulated rough fracture surfaces displayed in **Figure 44** do not actually represent one continuous surface, but rather a series of coordinates spaced tightly together. To produce a 3D model appropriately formatted for 3D printing, this computer-generated series of points was processed and converted into the ".stl" file required for communication with the 3D printer.

This process, in addition to the generation of the mirror fracture surface, is executed with an in-house Python code. The code utilized for this research was amended from Stanford University's Geostatistical Software Library (GSLIB) and from Dr. Michael Pyrcz's Geostats Py Python Library with modification help from Tohoko Tajima and Gabriel Tatman. Also executed with this in-house Python code is a process to cut the greater fracture network into one square foot pieces. Recall that the main fracture surface is 4 feet long and 2 feet wide and that the side fracture surface is 1 foot long and 2 feet wide. The print volume is not large enough to print this entire fracture network at once, so the 3D model is divided into twenty separate 1-foot by 1-foot fracture tiles.

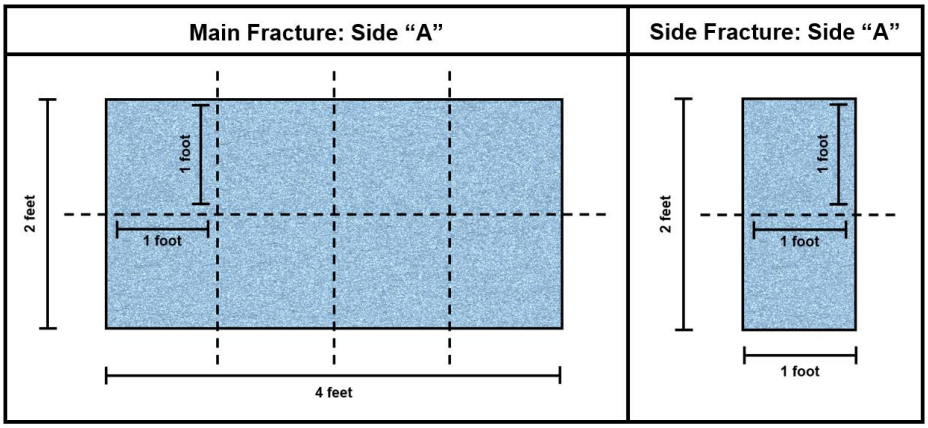

Figure 45: Scaling Fracture Network Model to 1' x 1' Tiles for 3D Printing

An illustration of the scaling process for the greater fracture network is pictured in **Figure 45**. This illustration only depicts one half of the fracture network. The other mirroring surface is scaled with the same procedure. The twenty resulting tiles are comprised of eight tiles that together represent one half of the main fracture, eight tiles that represent the mirror half of the main fracture, two tiles that together represent one half of the secondary fracture, and two tiles that represent the mirror half of the secondary fracture.

3.2.3 Preparing 3D Model for 3D Printer

The workflow outlined in the steps above has illustrated how to simulate a rough fracture surface with geostatistical inputs, how to appropriately convert that simulated surface into a 3D model, and how to divide that 3D model to the size required for 3D printing. An example of the resulting matching fracture surface tiles—sized appropriately and characterized with geostatistical parameters—is displayed in **Figure 46** below.

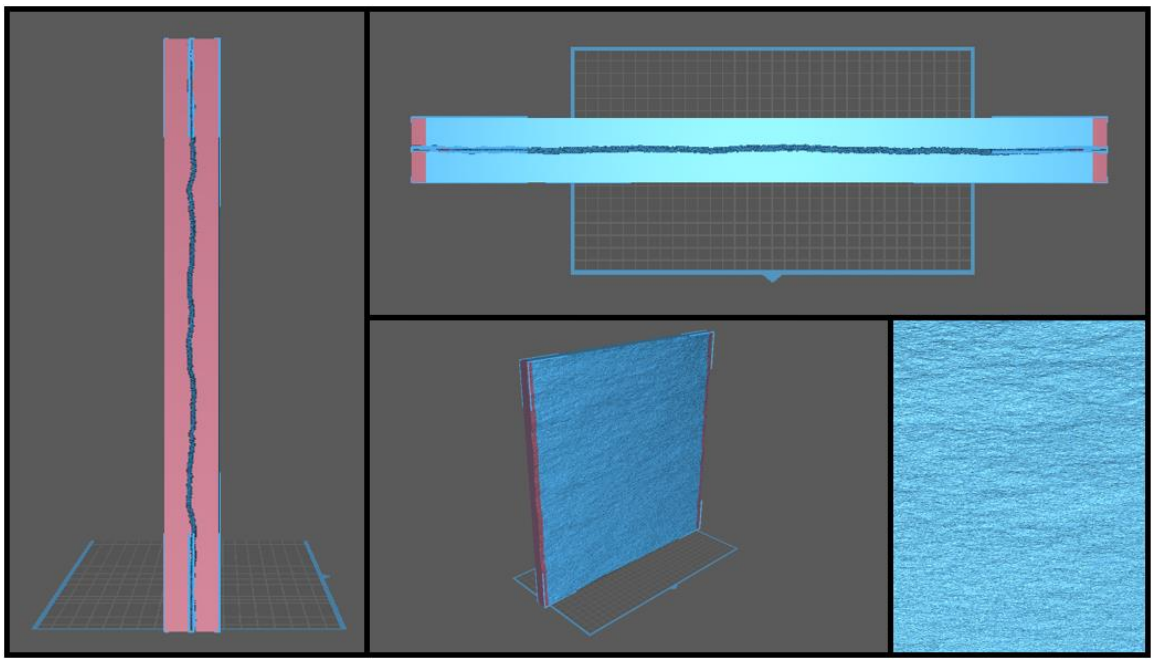

Figure 46: Example of Second Iteration Proppant Transport Matching Fractures

Observe in **Figure 46** that, while the two mirror fracture surfaces perfectly match, they do not fit on the build plate together at the same time. To ensure that the tiles are printed successfully, each must be printed individually and oriented as illustrated in **Figure 47** to fit on the build plate.

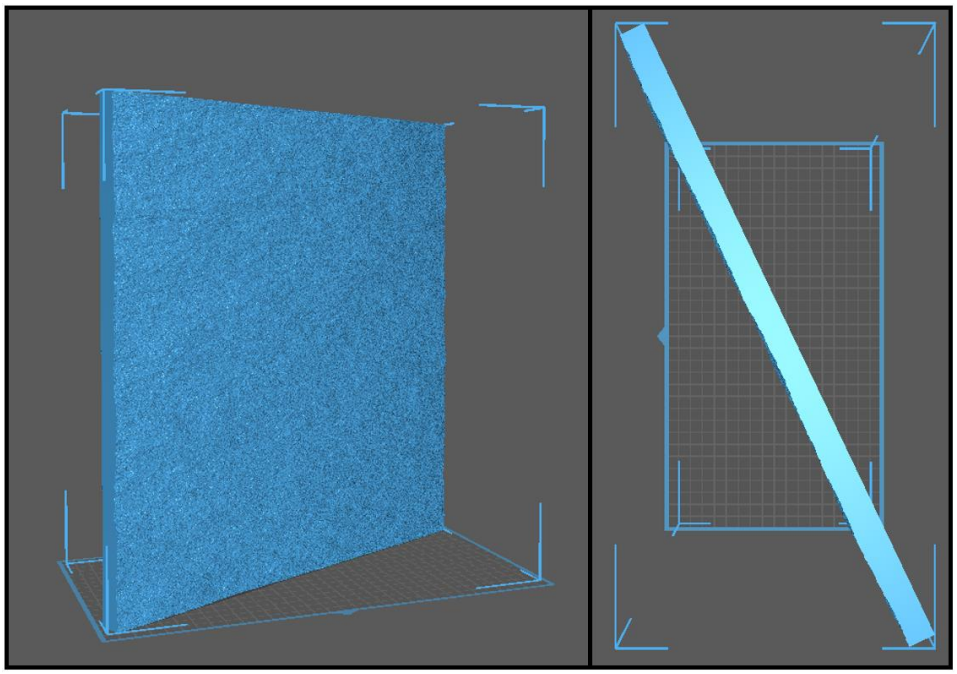

Figure 47: Orienting Fracture Tile Appropriately Prior to 3D Printing

In preparing these fracture tiles for 3D printing, it is important to note that they should not be hollowed out as was done for the fracture conductivity models. This would make the tiles more susceptible to warping after exposure to pressure and temperature changes in the proppant transport apparatus.

At least 15 mm of supports should also be incorporated to ensure that no resolution on the tile itself is lost to the overexposure required of the bottom model layers necessary to create a strong base foundation for the print. The manner in which these supports should be attached to the model is illustrated in **Figure 48**.

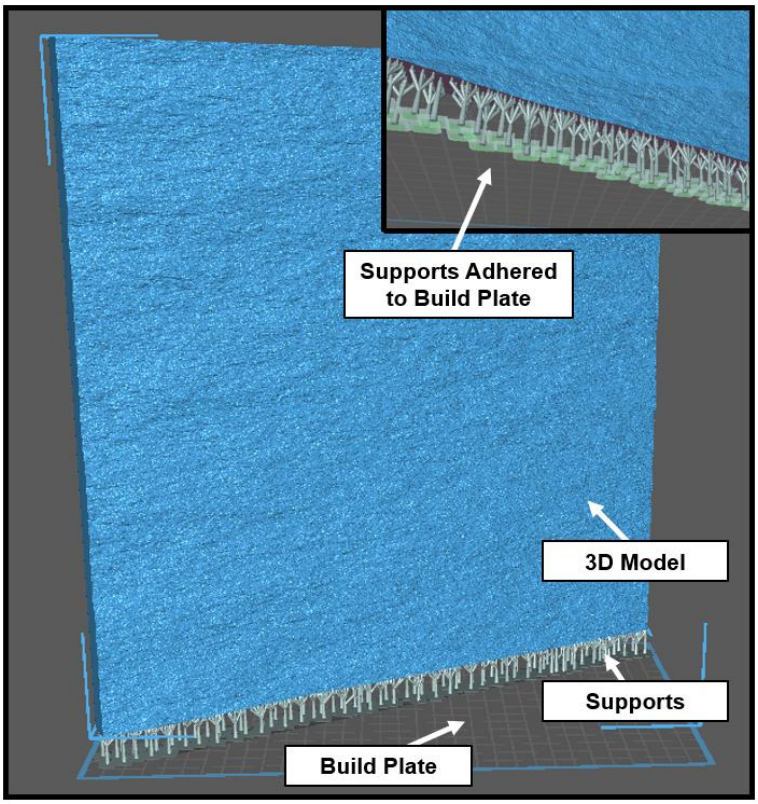

Figure 48: Appropriate Support Applied to 3D Fracture Surface Model

Because incorporating supports into the model can potentially leave behind unwanted signatures, each tile should be oriented prior to printing so that the supports for a respective tile are always on the side of the fracture that will not serve as a connection point to another neighboring tile during fracture network assembly.

In **Figure 49**, the red lines annotated on each respective 1-foot by 1-foot fracture tile represent the side of the fracture tile that should have supports on it during the model preparation and printing stages. This dictates that each of the fracture tiles displayed in **Figure 49** must be oriented prior to slicing such that the side of the tile highlighted by the red line is positioned on the build plate. Failure to align the potential for imperfections

towards the outskirts of the fracture system will result in difficulty assembling the fracture network seamlessly.

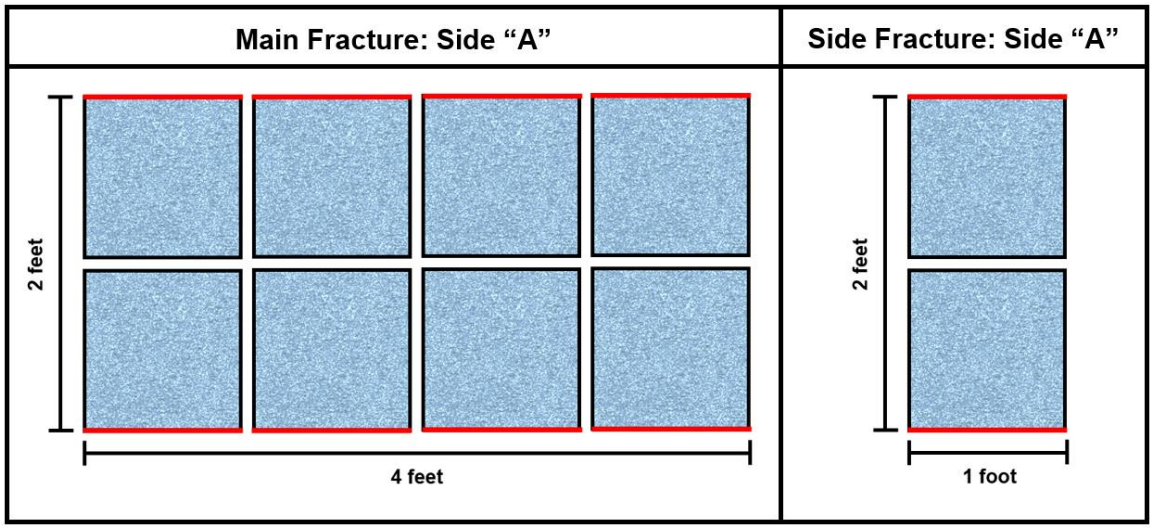

Figure 49: Appropriate Support Orientation on Tiles Comprising Fracture Network

3.2.4 Printing the 3D Model

The Phrozen Transform Fast was the Digital Light Processing (DLP) 3D printer used in this study. Recall that DLP printers are unique in that they leverage one light source in the form of an LCD screen to selectively cure, or harden, liquid resin. The 3D printing process required for success in this particular application varies slightly from the application outlined in the second chapter of this thesis.

Similar to printing conductivity samples, the Z-axis must be leveled and the exposure time for the resin used must be calibrated prior to printing. In this case, AnyCubic Clear Resin was used to print this rough fracture surface to ensure proppant visibility through the fracture system. Both of these procedures were reviewed thoroughly in the previous chapter and will not be included in this one. That said, it is worth noting that the

appropriate exposure time found for the AnyCubic Clear Resin with the calibration process previously outlined differs from the appropriate exposure time for the AnyCubic Grey Resin used to print fracture conductivity samples. Appropriate exposure time for the AnyCubic Clear Resin for this application was found to be 2.5 seconds. This is 0.5 seconds longer than the appropriate exposure time for the previously used AnyCubic Grey Resin.

Recall that, prior to slicing the model (thereby sending instructions to the printer), it is necessary to make appropriate adjustments to the printer settings for this specific 3D printing application. These adjustments are displayed in **Figure 50** and represent appropriate changes to settings required to print a much larger and heavier 3D model. Machine settings (previously shown in **Figure 24**) should remain the same.

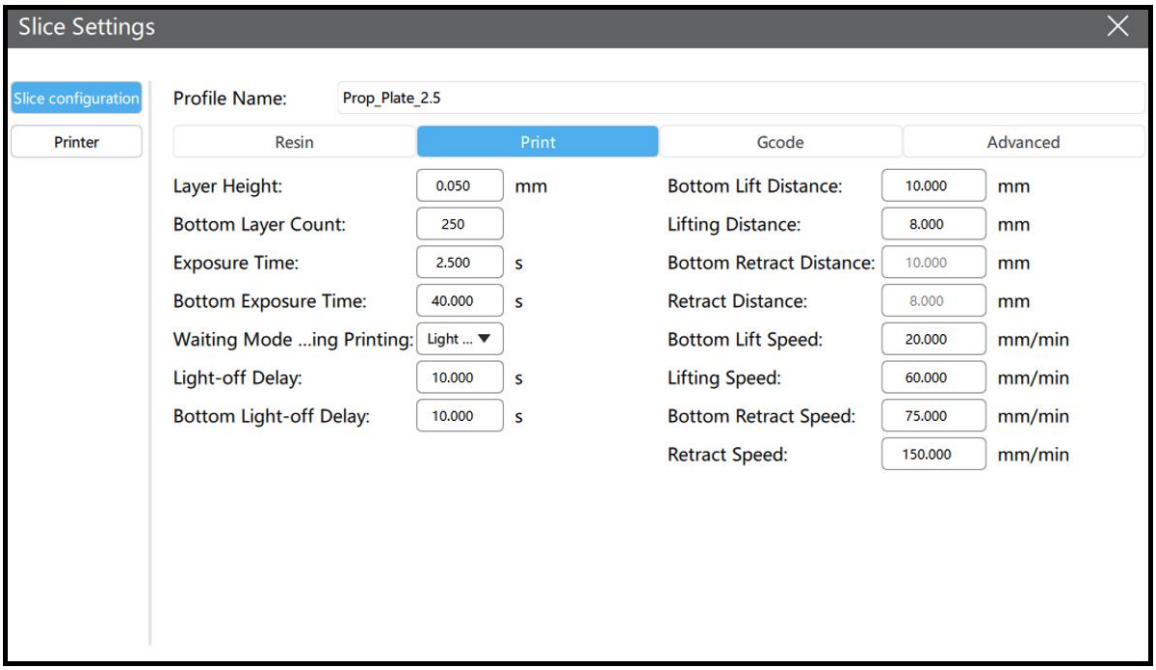

Figure 50: Proppant Transport Plate + AnyCubic Clear Resin Printer Settings

Observe that, given this change in application, these printer settings differ significantly from their fracture conductivity model counterparts. When printing proppant

transport tiles, “Bottom Layer Count” should be increased to at least 200 layers. This parameter can be increased as much as is necessary to ensure that the model adheres successfully to the build plate, so long as this value does not surpass the layer count of the supports. If this parameter exceeds this maximum value, the model itself will be left susceptible to unwanted signatures caused by the overexposure that characterizes the bottom-most layers of the model.

Because of their weight, it is also necessary to increase the “Bottom Exposure Time” of the 3D model to ensure proper adhesion to the build plate when printing. As mentioned in the second chapter, general guidance suggests appropriate values for this exposure range between five to ten times longer than the exposure time required for the rest of the model. In this heavy-weight case, the exposure for the bottom-most layers of the model should be set between twenty and forty times longer than the exposure time required for the rest of the model. As such, “Bottom Exposure Time” was amended to 40 seconds for proppant transport plate printing.

Because, in this case, adjusting both “Bottom Layer Count” and “Bottom Exposure Time” was not sufficient in achieving consistent model adhesion to the build plate, “Bottom Lift Speed” was adjusted from 65 mm/min to 20 mm/min and “Lifting Speed” was adjusted from 85 mm/min to 60 mm/min. When printing heavy-weight models, reducing lift speed settings can help successful adhesion to the build plate by minimizing the force pulling the model off of the build plate during its ascent.

Because the amendments to printer settings outlined above dictate that resin is exposed to UV light for longer periods of time, these adjustments will extend print time

and make removing the partially-overcured tile from the build plate much more difficult. As such, these setting adjustments should only be made when poor model adhesion to the build plate is being observed consistently and is impacting the quality of the print.

After appropriately orienting and supporting the 3D model and after adjusting printer settings to be appropriate for this printing application, the 3D model can be sliced, saved, and exported to the 3D printer. Recall that slicing the model is jargon for converting the ChiTuBox user settings to a printer-compatible file containing two important pieces of information for the 3D printer: (1) images representing each cross section of the model, and (2) instructions that dictate printer settings including exposure time, lift speed, positioning information, and more.

An example of this slicing process is depicted in **Figure 51**.

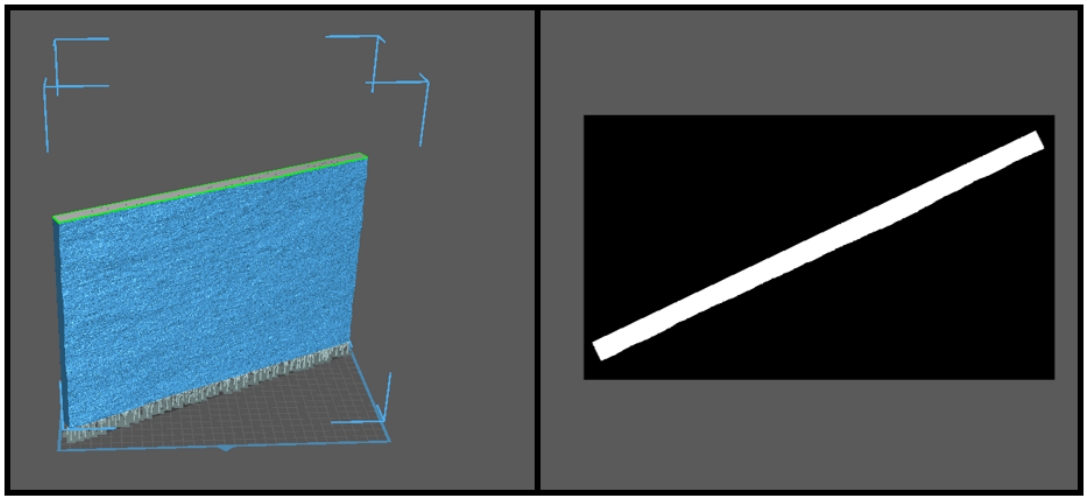

Figure 51: Example "Slice" of Proppant Transport Plate 3D Model

After the build plate has been leveled, exposure time has been calibrated, and the 3D model has been sliced with the appropriate printer settings, the following procedure should be followed to print the 3D model:

1) Select the model to be printed in ChiTuBox. Select the appropriate resin profile to communicate exposure and lift instructions to the printer.
2) “Slice” the model by selecting “Single Parameter Slice” in ChiTuBox.
3) Save the sliced model and model instructions by selecting “Save” in ChiTuBox. Save the resulting “.zip” file to the computer.
4) Duplicate the “.zip” file. In the duplicated file, change the “.zip” distinction to “.phz”.
5) Load the “.phz” file onto a USB. Use the USB to upload the file to the 3D printer.
6) While the model file is loading onto the 3D printer, ensure that the build plate and resin vat are totally clear of debris and residual resin from prior print jobs before installing them on the 3D printer.
7) Pour the liquid resin previously calibrated for exposure time into the resin vat.
8) After the build plate and resin vat have been secured in the 3D printer and after the model has been loaded successfully, select the checkmark on the interface of the 3D printer to commence the printing process.
9) After the print is finished, remove the build plate (with the model adhered to it) from the printer.
10) Use a metal scraper to remove the 3D print from the build plate. If the model will not detach from the build plate with a metal scraper alone, apply 550 ºF of heat to the area where the model adheres to the build plate with a heat gun for 30 seconds. Use heat-resistant gloves as necessary.

11) Remove and discard remaining supports from the 3D print by hand. If the supports will not detach from the build plate by hand or with the help of a metal scraper, a wet saw can be used to cut the remaining supports off of the printed model.
12) Wash the 3D print with isopropyl alcohol. Set the print on a paper towel to dry.
13) While the 3D print is drying, the build plate, resin vat, and LCD screen should all be thoroughly cleaned with isopropyl alcohol.
14) If the print is unsuccessful, adjust print slice configuration settings and repeat the process until success is achieved.

PPE required for this process includes gloves, eye protection, and a lab coat. While resin is non-hazardous and non-toxic when used as directed, care should be exercised in keeping it off of skin and out of eyes as it can cause minor irritation.

3.2.5 Post-Processing 3D Print

Several of the resulting 3D-printed fracture tiles are displayed in **Figure 52** below. Arrows annotated on the image illustrate the direction of greater correlation length.

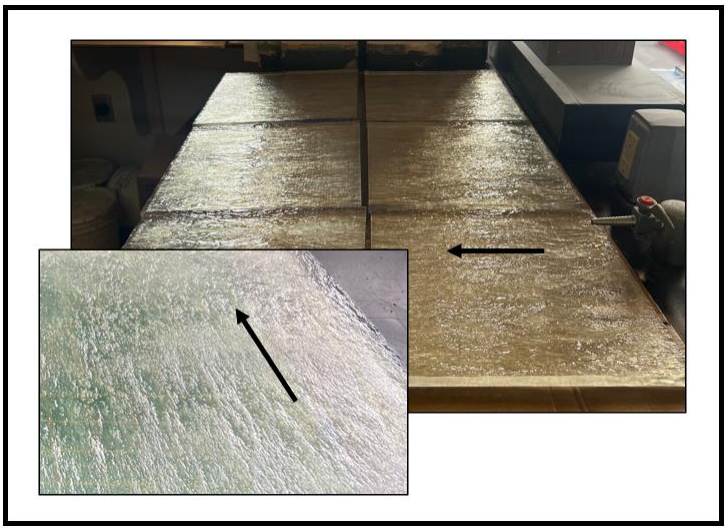

Figure 52: 3D-Printed Fracture Tiles Prior to Assembly

Similar to the workflow established for printing fracture conductivity samples, each proppant transport tile should be washed with isopropyl alcohol and thoroughly dried. Unlike the workflow outlined in the previous chapter, the 3D print should not be subsequently cured under additional UV light. Doing so will turn the clear surface yellow or brown, reducing the visibility that is critical to result interpretation in proppant transport experiments.

Additionally, Rust-Oleum Crystal Clear Enamel should be used to coat both the front and back of the fracture face at least three times each. This epoxy coat will serve to enhance the visibility through the fracture network while also protecting it from erosion by the water, sand, and diverter it will be exposed to in proppant transport experiments. **Figure 53** demonstrates the enhanced clarity that results as a function of the post-processing procedure described in this section.

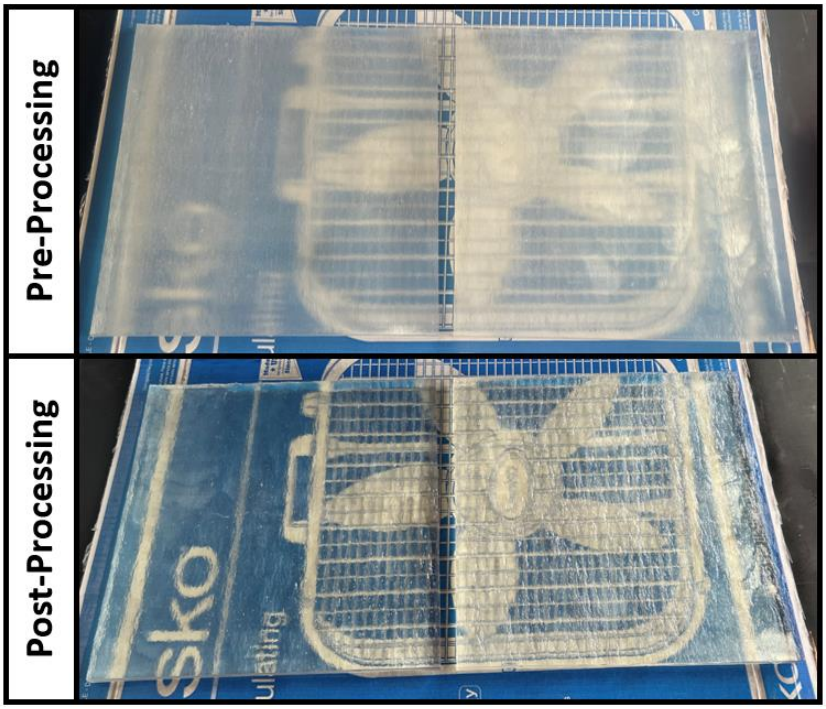

Figure 53: Improving Visibility Through Fracture with Post-Processing Procedure

The visibility through the fracture plates will be improved even further when they are submerged in water in the proppant transport experimental mechanism.

After all twenty plates comprising the greater fracture network have been printed and post-processed, they are carefully packed and shipped to Colorado School of Mines for assembly and experimentation.

3.2.6 Assembling Fracture Network

As described in a previous subsection, a geostatistical characterization was applied to a 48-inch long, 24-inch wide surface representing the dimensions required for the main fracture in the fracture network and a 12-inch long, 24-inch wide surface representing the dimensions required for a secondary fracture in the fracture network. Due to printer volume constraints, these surfaces were divided into twenty separate 1-foot by 1-foot tiles to be assembled after printing. Tiles should fit together seamlessly as illustrated in **Figure 54** and **Figure 55**.

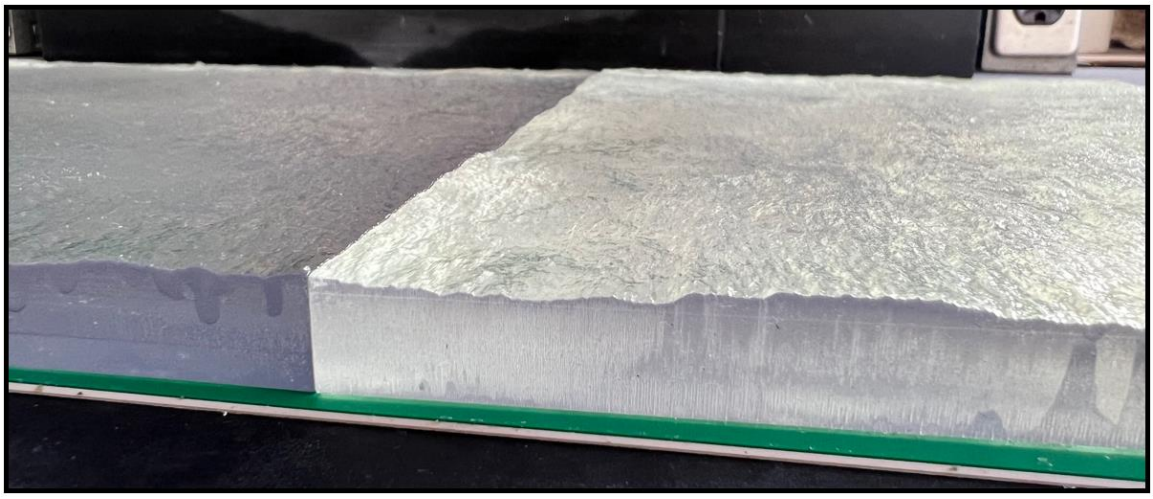

Figure 54: Seamless Transition Between Neighboring Fracture Tiles

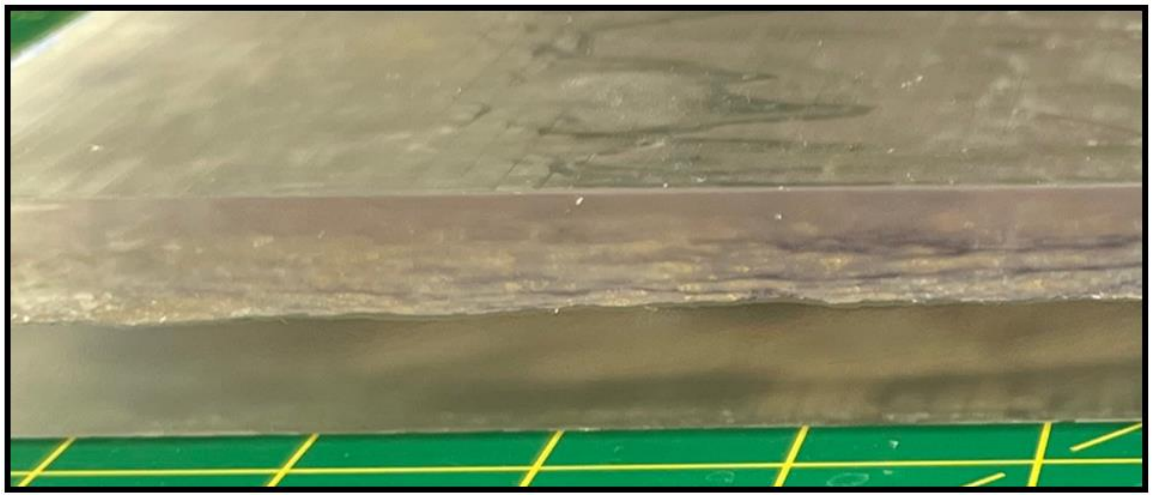

Figure 55: Mirroring Fracture Surfaces Align Precisely

Tiles were assembled into continuous fracture faces with clear contact cement applied to the tile edges prior to clamping neighboring surfaces together (Tatman et al. 2022). A 0.2-inch spacer was used to dictate the width between the matching fracture faces in the main fracture. A 0.1-inch spacer was used to dictate the width between the matching fracture faces in the secondary fracture. **Figure 56** illustrates tiles assembled on both sides of the main fracture.

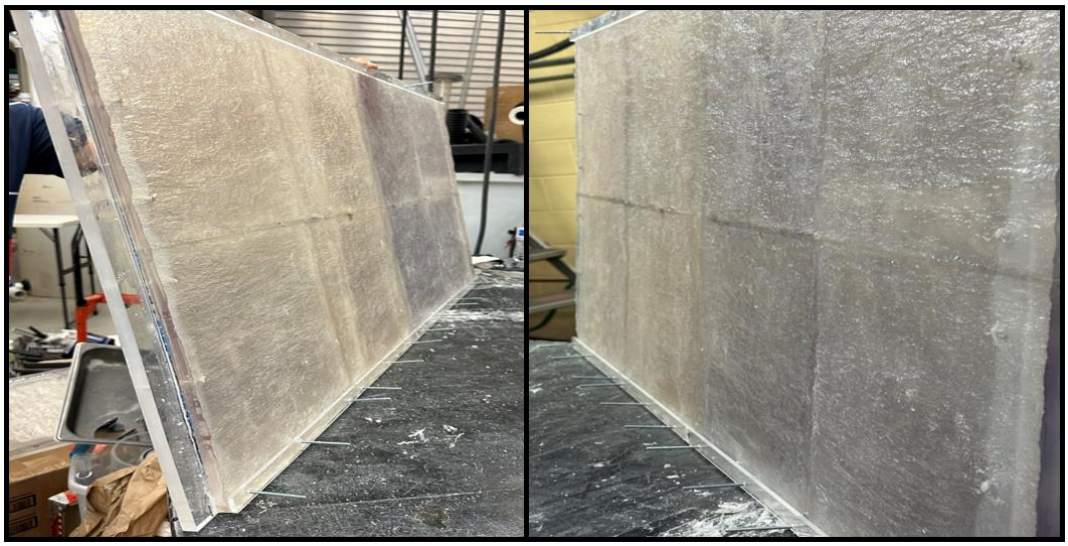

Figure 56: Post-Assembly Main Fracture

3.2.7 Executing Proppant Transport Experiments

The Colorado School of Mines experimental apparatus used for this proppant transport experimental program is illustrated in **Figure 57**.

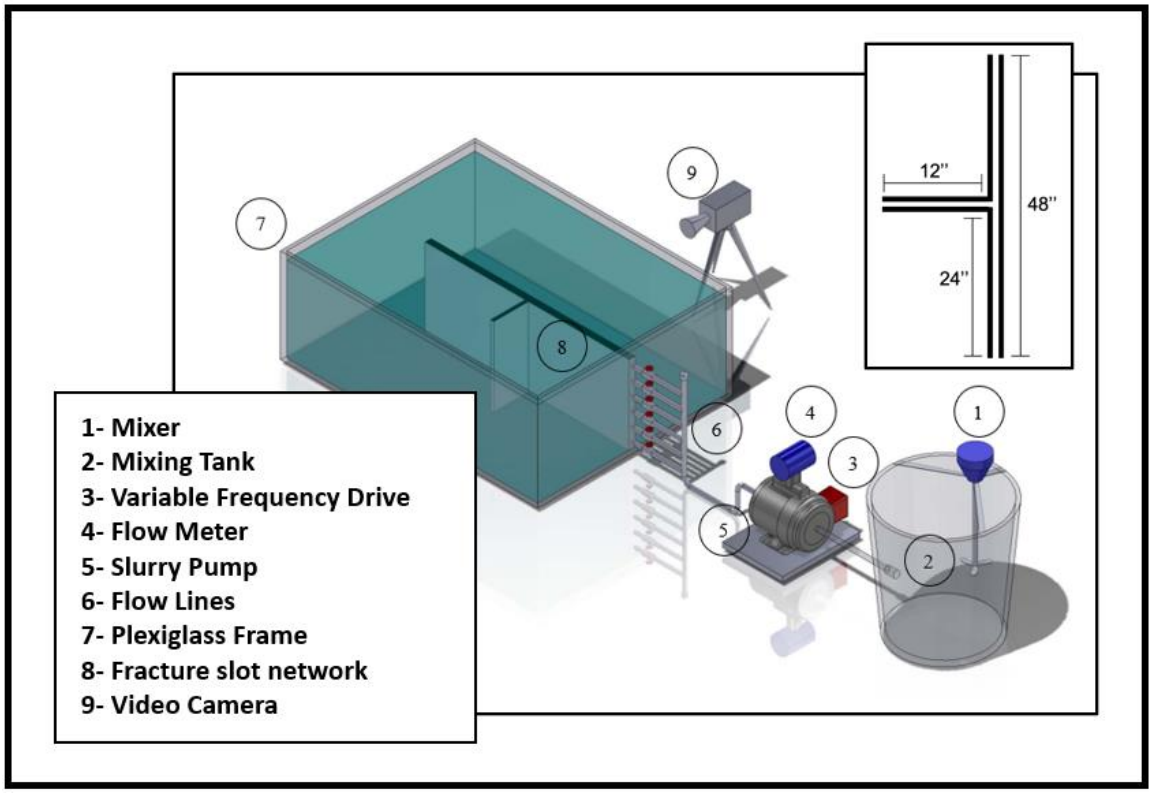

Figure 57: Colorado School of Mines Proppant Transport Experimental Apparatus

Figure 58 displays the proppant transport apparatus with the fully assembled fracture network in place.

After confirming that the assembled fracture surfaces were able to withstand the pressures and rate associated with pumping slurry through the system, the experimental study was commenced. Proppant size, proppant concentration, proppant type, diverter concentration, diverter type, injection rate, and fracture width are variables amended to better understand how these parameters relate to proppant transportation and distribution.

Figure 58: Post-Assembly Proppant Transport Experimental Apparatus

Although experimental results obtained with this iteration of rough fracture surface are still preliminary, they will be briefly addressed in the following section.

3.3 Results & Discussion

As was mentioned in the introduction to this chapter, this study attempts to layer an additional subsurface complexity into existing proppant transport experimental studies. The first iteration of plates was printed and analyzed by Tatman et al. (2022). Equal correlation length in both the X and Y directions dictates that the surface roughness of this fracture system shows no particular affinity for features in either direction. Variation in height appears randomly. The second iteration of plates was presented in the workflow outlined above. Geostatistical parameters remain the same relative to the first iteration fracture system with the exception of correlation length in the X direction which was amended from 1 inch to 3 inches. The resulting surface—previously depicted in **Figure 44**—is characterized by striations aligned parallel to the direction of flow. While results

from the second iteration of proppant transport plates are still being processed, the purpose of this impending analysis will be to compare the results associated with the first iteration fracture system with the preliminary findings associated with the most recent iteration of proppant transport tiles.

To make direct comparisons across fracture systems with varied surface roughness, experimental conditions will be held constant while proppant size, proppant concentration, proppant type, diverter type, diverter concentration, injection rate, and fracture width are all varied individually to isolate their impact on proppant transportation and distribution.

While experiments are still in the process of being conducted with the fracture network most recently produced, preliminary experimental results—such as those displayed in **Figure 59**— indicate that experiments to date have been not only successful, but also offer unique insights.

Figure 59 demonstrates the impact that varied surface roughness has on proppant transportation and distribution in the 0.2-inch main fracture with 1 ppg of 40/70-mesh proppant at a flowrate equivalent to 40 bbl/min.

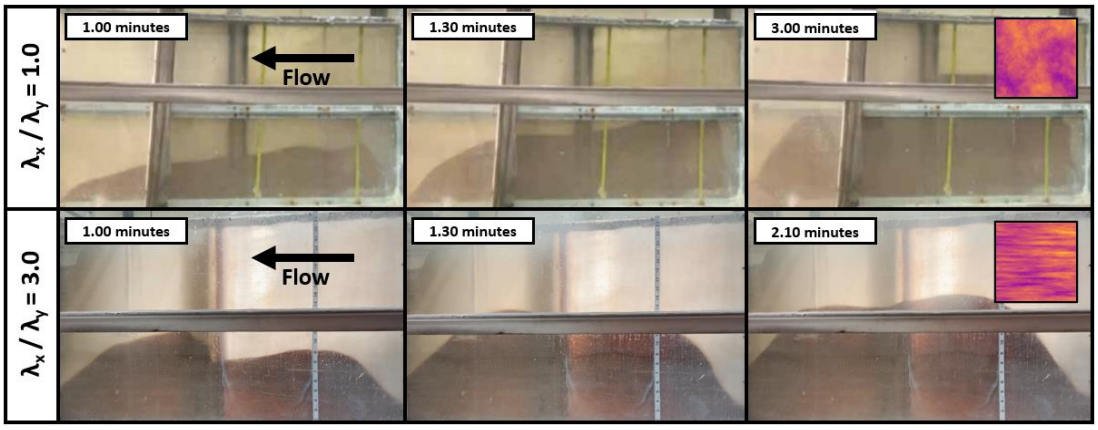

Figure 59: Proppant Transport Summary – Main Fracture (1 ppg, 40/70 mesh)

Because experimental results have yet to be published by principal investigators, further explanation and analysis of experiments conducted to date will be left to Dr. Ashtiwi Bahri and Dr. Jennifer Miskimins at Colorado School of Mines.

Partial credit for this work should be attributed to Gabriel Tatman (Texas A&M University) for printing the first iteration of the fracture network and to Dr. Ashtiwi Bahri (Colorado School of Mines) for conducting experiments on both sets of fracture systems, in addition to Dr. Ding Zhu, Dr. Dan Hill, and Dr. Jennifer Miskimins, who are all principal investigators of this research program.

3.4 Conclusions

The primary objective of the study summarized in this chapter was to incorporate another layer of subsurface complexity into proppant transport experiments by creating a fracture network characterized by rough-wall fracture surfaces.

Because fracture surface topography is instrumental in informing results across proppant transport experimental workflows, it was important to successfully establish and vet a procedure to inform rough fracture surfaces with geostatistical parameters, ensuring that no resolution is lost in the 3D printing process. As such, this chapter comprehensively summarizes the workflow created to generate this rough-wall fracture network with geostatistically-informed surfaces.

In short, a rough fracture surface was first simulated with a series of geostatistical parameters serving as inputs to a geostatistical library. The output simulated rough fracture surface was then scaled to the appropriate size for proppant transport experimentation and

printed with a Digital Light Processing (DLP) 3D printer. Following this, the fracture network was assembled and used for experimentation. Results associated with this updated fracture network will be compared to the previous surface characterization generated, printed, and analyzed by Tatman et al. (2022). The updated fracture system is characterized by a surface that has more correlation in the direction of flow relative to the first iteration of transport plates which were characterized by equal correlation lengths in both directions. Although the results garnered from the most recent fracture system are preliminary, they do show promise in offering major insights.

The technical work presented in this section successfully demonstrated the following:

1) A robust workflow was implemented to create a geostatistically defined rough fracture surface through the use of 3D printing.
2) Twenty tiles comprising a greater fracture network were successfully printed and assembled at Colorado School of Mines.
3) Experiments with the same fracture size, fracture width, slurry injection rate, proppant density, and proppant concentration allow proppant size and surface topography to be evaluated to determine their impact on proppant transport and distribution.
4) Varying surface topography by incorporating a system with more correlation in the direction of flow resulted in significant changes to proppant transportation and distribution behavior.

4. GENERAL DISCUSSION, LIMITATIONS, AND CONCLUSIONS

4.1 Introduction

Experimental studies geared towards analyzing the relationships between well stimulation parameters and subsurface characteristics are inherently difficult to design and execute. The two studies introduced in this thesis offer a unique approach to reducing the uncertainty associated with stimulation experimental results, while layering in additional complexities.

This chapter discusses significant existing limitations associated with current analyses, in addition to exploring recommendations for future work.

4.2 Limitations

Both fracture conductivity and proppant transport experimental workflows are associated with a few minor limitations.

4.2.1 Fracture Conductivity Workflow Limitations

Recall from the second chapter of this thesis that the conductivity associated with cement samples appears to be somewhat higher than their unconventional reservoir rock counterparts. Initially this observation was thought to be unwanted signatures on the surface of cement samples from the silicone casting degassing on the fracture faces while cement was in the process of curing. After resolving this degassing obstacle, conductivity of the cement samples remains slightly higher than should be expected in real-rock applications.

It is believed that this higher conductivity is due to minor divergence of the fracture faces, particularly on the flanks of the conductivity sample, which are highlighted in red circles in **Figure 60**. This phenomenon is shown and exaggerated by applying pressure to one side of the conductivity sample displayed in **Figure 60**.

Figure 60: Illustration of the Divergence of Matching Surfaces on Sample Flanks

This behavior cannot be attributed to the shape or size of the 3D print, as illustrated by applying pressure to one side of the 3D-printed sample in **Figure 61**.

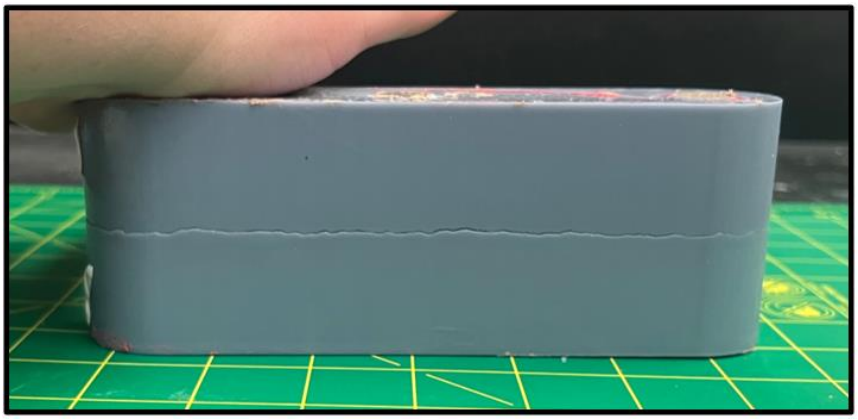

Figure 61: 3D-Printed Conductivity Sample Shows No Surface Divergence

This seems to suggest that the behavior showcased in **Figure 60** can be attributed to the silicone casting. Because the cement fracture faces appear to align perfectly towards the middle of the conductivity sample and only begin to diverge towards the flanks of the sample, it is suggested that the elasticity of the silicone mold is yielding to the weight of the cement while it is still curing. This is illustrated in **Figure 62**.

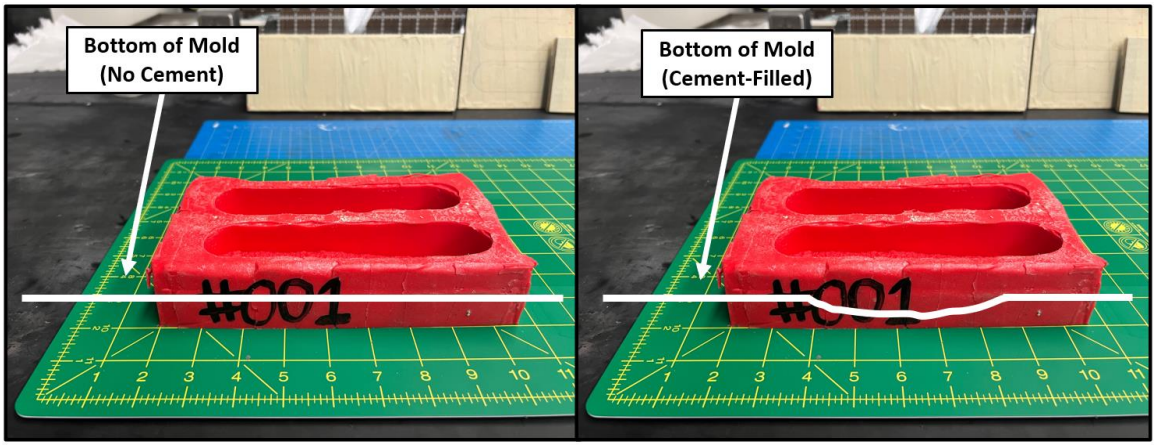

Figure 62: Illustration of Silicone Sagging Behavior Leading to Ill-Fitting Samples

Notice in **Figure 62**, that the bottom of the mold (which is the rough surface face of the fracture) is almost a half-inch off of the table. This allows the silicone to exercise its elastic properties by sagging in the middle of the mold. The solution to resolving this behavior is simple. There should be as little excess silicone below the bottom of the mold (or rough fracture face) as possible. This means that when the silicone casting is being created, silicone should be poured into the container slowly until the face of the conductivity samples are barely submerged. The silicone should be translucent enough that the fracture faces are still visible to the naked eye through this layer of silicone.

Minimizing the excess silicone below the fracture faces in the silicone castings should prevent the silicone from sagging towards the middle of the mold. This idea is depicted in **Figure 63**.

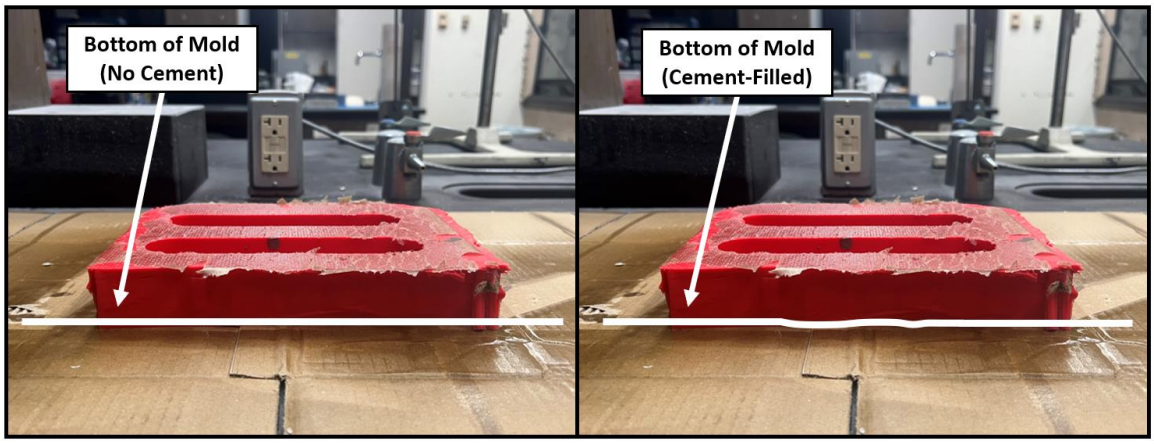

Figure 63: Illustration of Silicone Sagging Behavior Resolution

This small step should resolve the character of the conductivity sample fracture faces illustrated in **Figure 60**, yielding lower and more realistic conductivity results.

4.2.2 Proppant Transport Workflow Limitations

Recall from the third chapter that the 3D-printed, rough-walled fracture network generated for proppant transport experiments highlighted in this thesis is not the first of its kind. Tatman et al. (2022) were the first to implement this workflow.

It is worth noting that one key trouble Tatman et al. (2022) ran into in their efforts to implement a 3D-printed fracture network in proppant transport experiments was the deterioration of the 3D-printed rough fracture surface after a considerable number of experiments were ran successfully.

This plate deterioration was first identified when the fracture system—specifically the main fracture—began warping. This character is displayed in a portion of the main fracture in **Figure 64**.

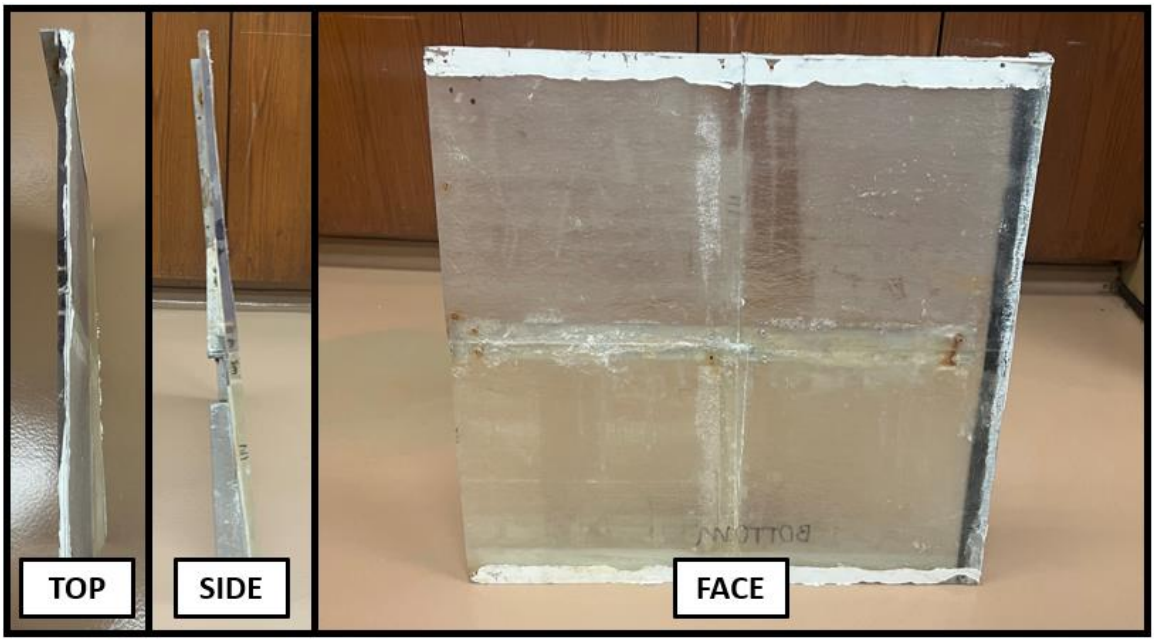

Figure 64: Main Fracture Warping in First Iteration Fracture System

Although this warping could have been due to the interaction between the 3D-printed fracture and fracture fluid, precautions were taken when creating the second iteration fracture system in the event that this warping was simply pressure induced. First, the second set of plates is twice as thick as the first set of plates. Fracture system specifications were ramped up from 0.25-inch thick plates to 0.5-inch thick plates. Second, a more robust layer of clear coat was used to protect both the front and back of each plate in the second iteration of the fracture system. Visibility was not impacted by either of these changes. The second iteration fracture system has yet to warp or deteriorate through eight experiments.

4.3 Future Work

Both fracture conductivity and proppant transport experimental workflows offer ample opportunity for future work.

4.3.1 Fracture Conductivity Future Work

The fracture conductivity workflow outlined in the second chapter of this thesis has proven to be successful in generating identical high-strength cement samples with geostatistically-informed rough fracture surfaces, in addition to exhibiting that this high-strength cement is an adequate proxy for unconventional reservoir rock in fracture conductivity experiments. Given this success in putting together a workflow, there should be no hurdles preventing a start to the experimental study proposed.

While the experimental study will certainly implement different proppant sizes, concentrations, and types, it will differ from existing experimental studies in that surface topography will also be varied consistently and repeatably.

Surface topography adjustments will include random / more uniform fracture topography, varied length correlation, and step-change / ridge signatures included on the face of the fracture.

Using the workflow outlined in the second chapter of this thesis, fracture conductivity samples with varied correlation in the direction of flow have already been generated and printed. These samples are shown in **Figure 65** and **Figure 66**, respectively.

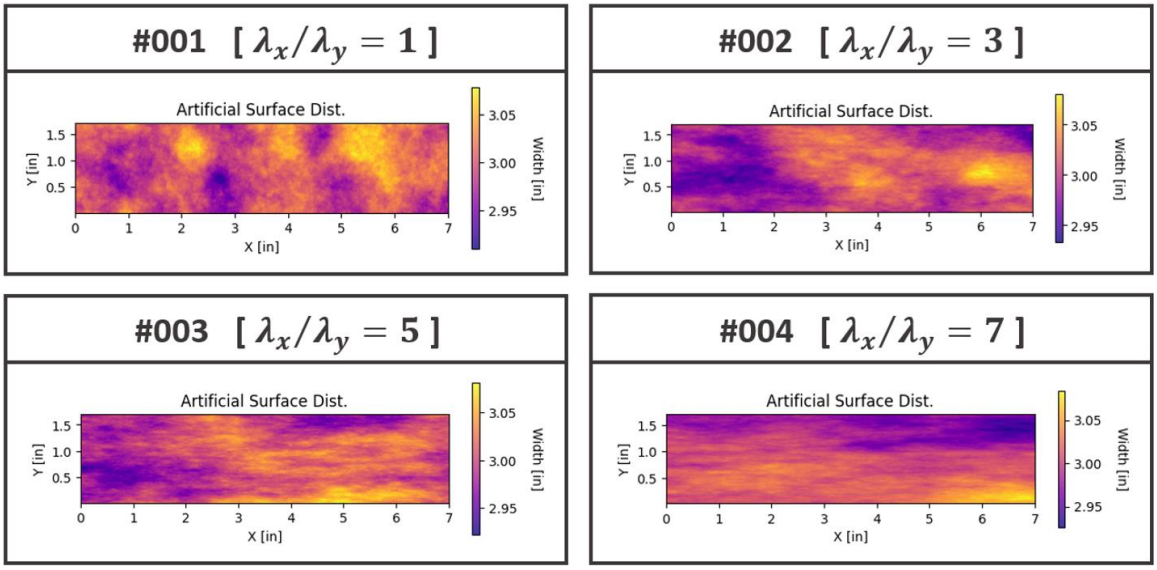

Figure 65: Simulated Surfaces with Varied Correlation in the Direction of Flow

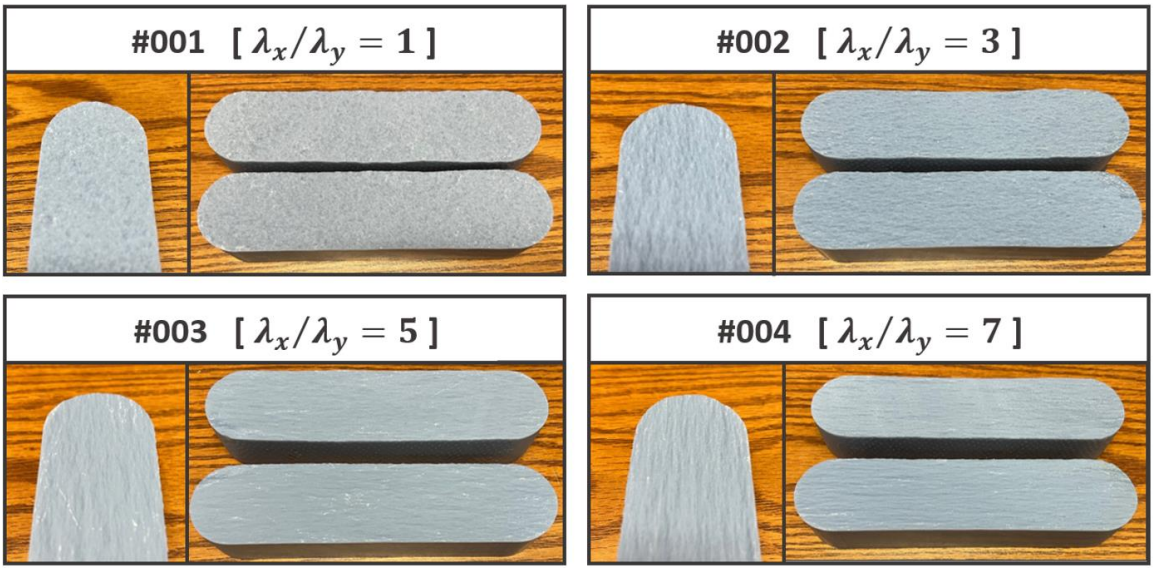

Figure 66: 3D-Printed Samples with Varied Correlation in the Direction of Flow

4.3.2 Proppant Transport Future Work

Given the interest that preliminary results for the two fracture systems to date have generated, great emphasis is being placed on printing another fracture system with a

different surface characterization. In fact, the third set of proppant transport plates has already been generated and is currently in the process of being printed. This particular surface realization is similar to the second iteration fracture system. It carries the same mean, standard deviation, and correlation lengths in both the X and Y direction as the previous iteration. This time, though, the 3D model includes a 0.1-inch ridge also running in the direction of flow. An example of this model is illustrated in **Figure 67**.

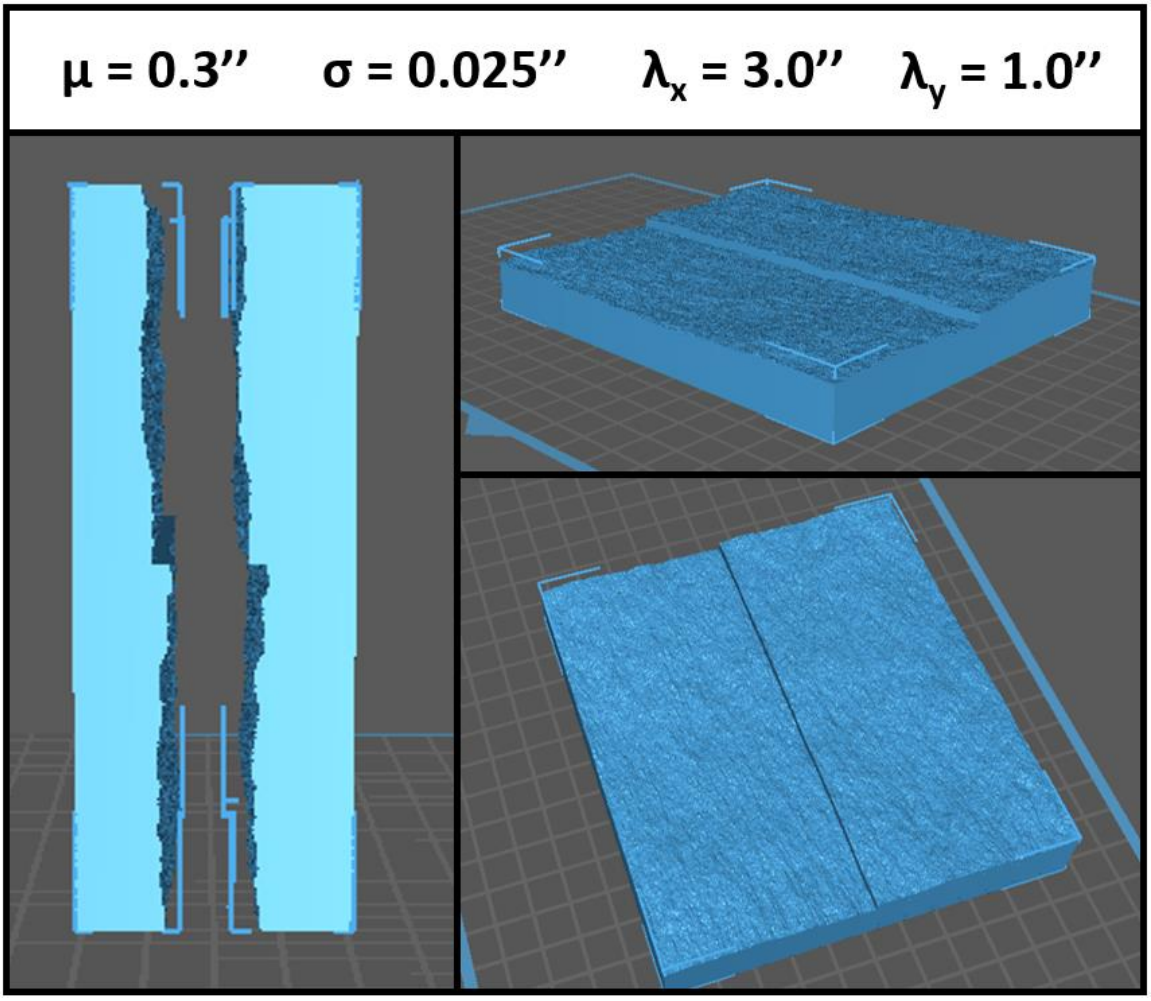

Figure 67: Third Iteration Fracture Network for Transport Experiments Example

Additionally, the process to print these plates is getting significantly easier given the addition of a new printer—the Phrozen Sonic Mega—to the laboratory. This printer

primarily differs from the Phrozen Transform Fast in that the XY resolution of the printer is twice as granular and the build volume is approximately 25% bigger. This will reduce the print time associated with proppant transport plate printing—a huge constraint in this experimental program— substantially. This printer is displayed in **Figure 68**.

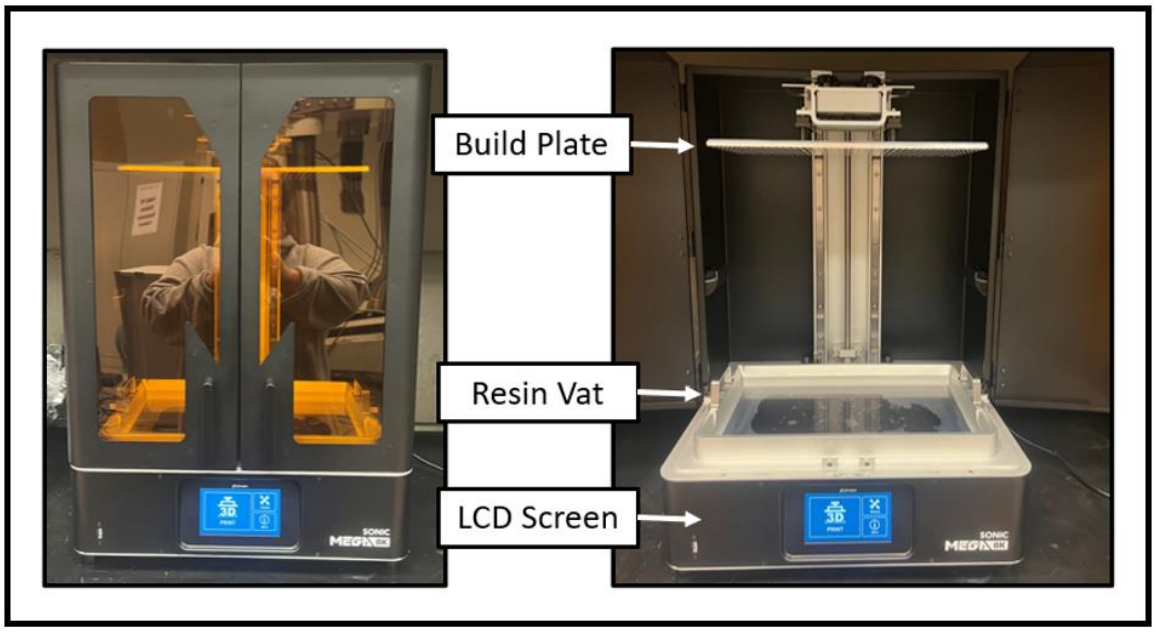

Figure 68: Phrozen Sonic Mega Digital Light Processing (DLP) 3D Printer

4.4 Conclusion

In summary, this thesis serves to highlight two studies that employ 3D printing to amend their respective experimental workflows to be more comprehensive. The first of these workflows and primary focus of this thesis leveraged 3D printing to generate repeatable rock conductivity samples, reducing uncertainty associated with experimental results. Study results illustrated how proppant concentration impacts fracture conductivity while also demonstrating that conductivity results garnered from these 3D-printed samples are both repeatable and reasonable relative to previous experimental studies.

This thesis also aims, secondarily, to summarize progress made in making proppant transport experimental workflows more comprehensive with the help of 3D printing. Like fracture conductivity, how effectively proppant is transported through a fracture network and subsequently distributed throughout that network is a key determining factor in how prolific a fractured well in a given resource turns out to be.

While the foundation of these proppant transport and distribution experiments remains largely unchanged to date, this study aims to incorporate another layer of subsurface complexity by creating a fracture network for proppant transport experimentation characterized by 3D-printed, rough-walled fracture surfaces.

The rough-wall fracture network that was printed in this study differs from previous iterations of rough-wall systems in that the surface is characterized with correlation of features in the direction of flow. Results associated with this updated fracture network were compared to the previous surface characterization generated, printed, and analyzed by Tatman et al. (2022). Although the results garnered from the most recent fracture system are preliminary, they do offer significant insight into the impact that surface topography has on proppant transportation and distribution.

When employed appropriately, 3D printing can be leveraged to make a variety of stimulation experimental workflows more robust in nature.

5. REFERENCES

All3DP Pro. “The 7 Main Types of 3D Printing Technology.” All3DP Pro, 27 Mar. 2023, all3dp.com/1/types-of-3d-printers-3d-printing-technology/.

Alotaibi, M., & Miskimins, J. L. (2020). Experimental Quantification of Slickwater Proppant Transport in Subsidiary Hydraulic Fractures. International Petroleum Technology Conference. Dhahran, Kingdom of Saudi Arabia.

Anderson, T. (2016). Applications of Additive Manufacturing to Rock Analogue Fabrication. SPE Annual Technical Conference and Exhibition. Dubai, UAE.

Bahri, A., & Miskimins, J. (2021). The Effects of Fluid Viscosity and Density on Proppant Transport in Complex Slot Systems. SPE Virtual Hydraulic Fracturing Technology Conference.

Baidoo, M., Fillion, M.H., Hutchison, A., and C. Gonzalez. “Controlled Lab-Scale Evaluation of the Secondary Permeability Represented in a 3D Printed Discrete Fracture Network (DFN) Model.” Paper presented at the 3rd International Discrete Fracture Network Engineering Conference, Santa Fe, New Mexico, USA, June 2022. doi: https://doi-org/10.56952/ARMA-DFNE-22-0010

Brashear, A. T., Hill, A. D., Zhu, D., Kerr, E., Scofield, R., Jordan, D., Estrada, E., and T. Tajima. "Fracture Conductivity Created by Proppants and Acid in the Austin Chalk Formation." Paper presented at the SPE Annual Technical Conference and Exhibition, Houston, Texas, USA, October 2022. doi: https://doi.org/10.2118/210213-MS

Briggs, Kathryn , Hill, A. Daniel, Zhu, Ding , and Karen Olson. "The Relationship Between Rock Properties and Fracture Conductivity in the Fayetteville Shale." Paper presented at the SPE Annual Technical Conference and Exhibition, Amsterdam, The Netherlands, October 2014. doi: https://doi.org/10.2118/170790-MS

CBD-Tech. (2021). Chitubox Basic Ver. 1.7.0.

Chen, Chi , Wang, Shouxin , Lu, Cong , Wang, Kun , Lai, Jie , and Yuxuan Liu. "A New Method of Reproducing Rock Samples with Rough Surfaces for Testing Conductivity: A Case Study on Shale Propped Fractures." Paper presented at the International Petroleum Technology Conference, Virtual, March 2021. doi: https://doi.org/10.2523/IPTC-21263-MS

Cooke Jr, C. (1973). Conductivity of Fracture Proppants in Multiple Layers. Journal of Petroleum Technology, 1101-1107.

Copeland, A. (2020). The Impact of Proppant Grain-Size Distribution on Fracture Conductivity in Shale Formations. Texas A&M University, Petroleum Engineering, College Station.

Deutsch, Clayton V., and A. G. Journel. GSLIB: Geostatistical Software Library and User's Guide. Oxford University Press, 2017.

Enriquez-Tenorio, O.. , Knorr, A. F., Zhu, D.. , and A. D. Hill. "Relationships Between Mechanical Properties and Fracturing Conductivity for the Eagle Ford Shale." SPE Prod & Oper 34 (2019): 318–331. doi: https://doi.org/10.2118/181858-PA

Guerra, Jesse Mateo. n.d. “Fracture Conductivity Behavior in Shale Formations.” Texas A&M University. Accessed November 3, 2021. https://core.ac.uk/reader/237701880.

Isaaks, E.H. and Srivastava, R.M. 1989. An Introduction to Applied Geostatistics. New York: Oxford University Press, Inc. Mou, J. (2009). MODELING ACID TRANSPORT AND NON-UNIFORM ETCHING. College Station, TX: Texas A&M University.

Jansen, T.. , Zhu, D.. , and A. D. Hill. "The Effect of Rock Mechanical Properties on Fracture Conductivity for Shale Formations." Paper presented at the SPE Hydraulic Fracturing Technology Conference, The Woodlands, Texas, USA, February 2015. doi: https://doi.org/10.2118/SPE-173347-MS

Kern, L. R., Perkins, T., & Wyant, R. E. (1959). The Mechanics of Sand Movement in Fracturing. JPT.

Lai, Jie, Guo, Jianchun, Wu, Kaidi, Chen, Chi, Wang, Kun, Wang, Shibin, Lu, Cong, Zhao, Xuepei, and Huan An. "The Effects of Roughness and Mechanical Property of Rough Fracture Surface on Hydraulic Fracture Conductivity." Paper presented at the 53rd U.S. Rock Mechanics/Geomechanics Symposium, New York City, New York, June 2019.

Ma, S., Jin, G., Antle, R., and B. Wieneke. “3D Printed Rocks - an Emerging Technology for Systematic Petrophysical Studies.” Paper presented at the SPE Middle East Oil, Gas, and Geosciences Show, Manama, Bahrain, February 2023. doi: https://doi.org/10.2118/213383-ms

McGinley, M., Zhu, D., and A.D. Hill. "The Effects of Fracture Orientation and Elastic Property Anisotropy on Hydraulic Fracture Conductivity in the Marcellus Shale." Paper presented at the SPE Annual Technical Conference and Exhibition, Houston, Texas, USA, September 2015. doi: https://doi-org/10.2118/174870-MS

Perez Pena, P.. , Zhu, D.. , and A. D. Hill. "The Effect of Rock Properties on Fracture Conductivity in the Marcellus Shale." Paper presented at the SPE Asia Pacific Hydraulic Fracturing Conference, Beijing, China, August 2016. doi: https://doi.org/10.2118/181867-MS

Sistrunk, C., Brashear, A.T., Zhu, D., Hill, A. D., and T. Tajima. "The Effect of Fracture Surface Roughness on Propped Fracture Conductivity Using 3D-Printed Fracture Surfaces." Paper presented at the SPE Western Regional Meeting, Anchorage, Alaska, USA, May 2023. doi: https://doi-org /10.2118/213032-MS

Tatman, G. (2022). Utilizing 3D Printing Technology in Well Stimulation Research. Texas A&M University, Petroleum Engineering, College Station.

Tatman, G., Bahri, A., Zhu, D., Hill, A. D., and J. L. Miskimins. "Experimental Study of Proppant Transport Using 3d-Printed Rough Fracture Surfaces." Paper presented at the SPE Annual Technical Conference and Exhibition, Houston, Texas, USA, October 2022. doi: https://doi.org/10.2118/210196-MS

Winner, R. 2018. A Study on the Effect of Water Damage to Fracture Conductivity in the Meramec Shale. MS Thesis, Texas A&M University, College Station, Texas, U.S.A. (August 2018).

Zhang, Junjing, Kamenov, Anton, Zhu, D., and D. Hill. "Laboratory Measurement of Hydraulic Fracture Conductivities in the Barnett Shale." Paper presented at the International Petroleum Technology Conference, Beijing, China, March 2013. doi: https://doi.org/10.2523/IPTC-16444-MS